UCL
Université
catholique
de Louvain

École polytechnique de Louvain (EPL)

Analysis of the microstructure and the mechanical properties of an alloy Fe-Mn-Ni-Al-C for biodegradable bio-medical applications

Dissertation presented by
Héloïse Roelandts

for obtaining the Master's degree in
Chemical and Materials Engineering

Supervisor(s)
Pascal Jacques

Reader(s)
Laurent Delannay, Sarah Reuter

Academic year 2017-2018

Abstract

The artery diseases that originate from a substance called plaque which builds up inside the arteries are very common nowadays. Because of the presence of this plaque, the artery becomes narrower leading to a reduction of the blood flow which can cause, in the worst case, a complete obstruction of the artery. Several treatments exist including medication treatments or surgeries such as an artery bypass or a stent implantation.

In this work, a special attention will be devoted to the stents, which are small mesh tubes that are placed with a catheter in the weak or narrow arteries to restore a correct blood flow and to prevent the arteries from bursting. The current issues with this treatment are the potential late thrombosis, restenosis and the recurrence of a narrowing of the artery. Hence, this research focuses on a new generation of stents: the biodegradable stents.

The properties of a Fe-Mn-Ni-Al-C TRIP-maraging steel that could lead to medical biodegradable applications such as the coronary stents have been studied. Specifically, the impact of heat treatments on its microstructure and its mechanical properties have been investigated. In addition, the corrosion properties and the degradability of the TRIP-maraging alloy as a function of different heat treatments have been analysed thanks to several immersion tests. Furthermore, the austenite phase fraction has been approximated with a X-Ray diffraction analysis.

As a result, it appears that the phase fraction of austenite expands when the time of an annealing at $600°C$ is increased. However, a saturation can be highlighted after an annealing of 24 hours. The resulting microstructure presents austenite grains that grow from the martensite laths and prior austenite grain when the annealing time at $600°C$ is increased. On the other hand, performing a thermal cycling on the alloy accelerates the reversion onto austenite and presents an austenite phase fraction as high as the one resulting from an homogenization followed by the same annealing treatment. In addition, the resulting microstructure is finer and composed as well of martensite and austenite.

Moreover, the mechanical properties of the alloy increase as well when the annealing time increases. Again, there is a saturation of the improvements of the mechanical properties after an annealing time of 24 hours.

Furthermore, very high corrosion rates have been detected at the beginning of the immersions. In addition, the corrosion rates increase globally when the annealing time increases. However, when an annealing of 24 hours is performed, the corrosion rates decrease. Moreover, the corrosion of all the samples was localised. Specifically, the edges of the sample constituted favourable sites for corrosion. The energy dispersive X-ray spectroscopy revealed that there were large amounts of oxygen, iron and carbon that could highlight the presence of iron oxide. In addition, small amounts of calcium and phosphorus on the attacked area of the samples could be distinguished.

Keywords: *TRIP-maraging steel*, *biodegradation*, *stents*, *heat treatment*

Acknowledgements

First of all, I would like to thank my supervisor, P.Jacques, for his advises and his constant help throughout the whole project.

In addition, my particular attention to M.Croonenborghs and S.Reuter for their support and help. Specifically, I would like to thank them for their daily presence and help during the experiments as well as for the drafting of this master thesis.

Furthermore, my special thanks to the whole IMAP team for its conviviality and its good working atmosphere. Particularly, I would like to thank J.Lorfèvre, A.Maton and M.Frebutte for their help with the preparation of the samples as well as their contribution for the use of several machines.

In addition, many thanks to F. Van Wonterghem for helping me with the chemical and the XRD experiments. Moreover, I'm thankful to L. Ryelandt for the SEM formation as well as for her wise advises. Many thanks to Q. Mestrez for his help during the mechanical tests.

Finally, may all my supportive friends and family be thanked including my dog. They kept encouraging me and were supportive all through the academic year.

Héloïse

Contents

List of Figures

List of Tables

Introduction

When an artery is being blocked or is too narrow, the blood cannot pass anymore. Hence, the energy and the oxygen present in the blood cannot pass through the artery anymore leading, in the worst case, to the death of the cells being fed by this artery. For example, if it is the coronary artery that is blocked, the heart's blood supply becomes threatened, which can lead to important damages such as a heart attack.

Today, several treatments exist including stents, the coronary artery bypass graft and some medication treatments. The stents and the coronary bypass will require a surgery whereas the medication treatment will not. Specifically, the stent implantation requires a small device that has to be placed in the blocked artery. On the other hand, for a coronary artery bypass surgery, an artery or a vein from elsewhere in the body needs to be taken in order to be grafted to the blocked artery and bypass this one, leading to the reroute of the blood. [1]

In this work, a special attention will be devoted to the stents which are small mesh tubes placed in the weak and narrow arteries to restore a correct blood flow and prevent the arteries from bursting.[1] [2] Nowadays the main issues with this treatment are the possibilities of late thrombosis, restenosis and the recurrence of a narrowing of the artery. Consequently, researches are in progress to find new stents that could solve those different issues like the risk of a late thrombosis caused by the long-term device implantation with biodegradable stents.[3] [4] Specifically, the research pursues to create new stents needs to follow very strict constraints like some diverse mechanical and chemical constraints but more importantly, it needs to follow the strict rules of biocompatibility. Furthermore, this research flows from two distinct fields, namely, the medical field and the engineering field. While the medical research focuses on the causes of the several side effects and how to avoid them, the engineering research tries to find alternative solutions in materials and design.

The aim of this work is to study a transformation induced plasticity (TRIP) maraging steel that could lead to some medical applications like the coronary stent. The TRIP steels are known to have good mechanical properties as well as a good tenacity and strength. [5] Hence, the TRIP-maraging steels that combine the TRIP and the maraging effect allow an increase in both strength and ductility.

Specifically, an alloy of Fe-Mn-Ni-Al-C will be analyzed. First, the microstructure and the mechanical properties were characterised through several heat treatments. Then, some corrosion tests were performed in order to characterise the degradability of this alloy.

In this work, a background on the main concepts of this study will be first explained. Then, Chapter 2 will detail the experimental procedures. Chapter 3 will present the main results of the different experiments and in Chapter 4, those results will be discussed and the general trends highlighted. Finally, a conclusion gathering all those elements will be presented.

Chapter 1

Background

In this chapter, the fundamentals on the stents as well as their specifications and their material evolution will be reviewed. First, a brief summary on the artery diseases and their treatments will be exposed. Then, the emphasis will be laid on the implantation of a stent through their history and specifications but also through their material selection. Thereafter, the TRIP alloys and the properties of the austenitic phases will be summarized. Finally, a brief reminder on the corrosion will be made.

1 The context

A human body is constituted of a large number of blood vessels that play the role of paths for the blood to flow from the heart to any part of the body and back to the heart again. [6]

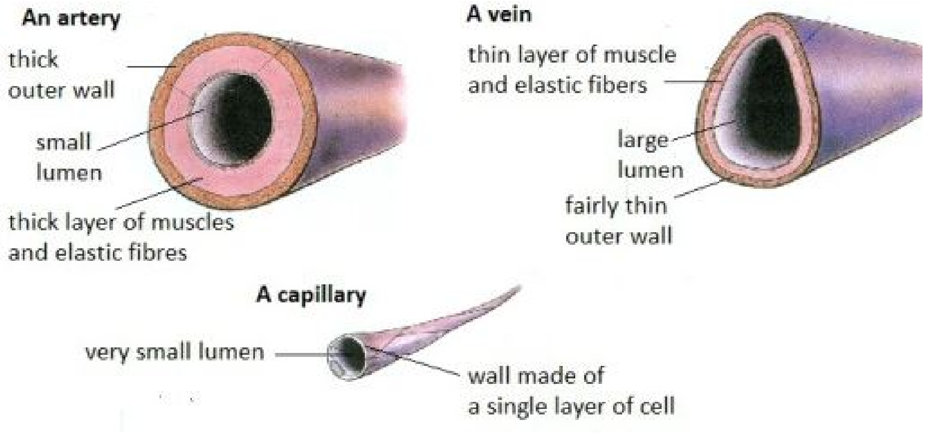

Figure 1.1: Schematic representation of the types of the blood vessels [7]

There are three types of blood vessels, namely, the capillaries, the veins and the arteries (Figure 1.1). More specifically, the blood vessels are composed of a hollow area called the lumen in which the blood can flow. The thickness of the wall of the vessel around the lumen will vary from something very thin for the capillary to something very thick for the artery. This difference in the wall's thickness comes from the difference of blood flow pressure and the pulse of the flow. While a small lumen helps to maintain the high blood pressure, the elastic tissue and the muscles present in the wall will respectively help the blood vessels to sustain the pulse of the flow and to regulate the blood pressure . [6] [7]

As a result, the arteries will have a thicker wall due to the high pressure of blood flow coming from the heart. On the opposite, the veins, that transport the blood back to the heart, will have thinner walls because of the loss of pressure in the capillary beds [1]. The capillaries, which are

---

[1] A capillary bed is formed by a network of capillaries that supply organs and tissues. Hence it represents a

the smallest blood vessels, are found in the tissues where they ensure the exchange of materials between the cells of the body and the blood.[6]

1.1 The artery diseases

Several artery diseases exist but they mainly originate from a substance called plaque that builds up inside the arteries (Figure 1.2). Because of the presence of this plaque, the artery becomes narrower leading to a reduction of the blood flow and in the worst case, can lead to a complete obstruction of the artery. [1]

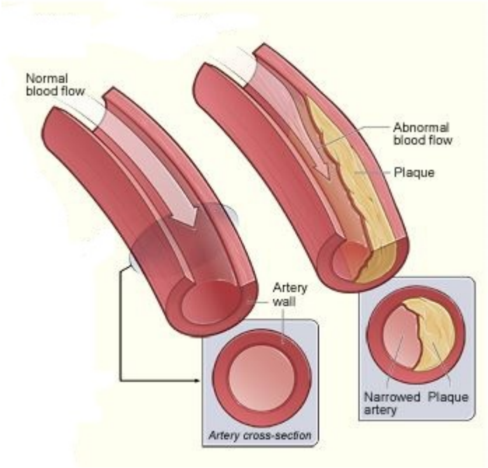

Figure 1.2: Schematic representation of the formation of plaque in the artery [10]

This formation of plaque can conduct to serious damages. The presence of plaque can increase the risk of blood clots that can lead to a heart attack in the case of a coronary arteries[2] but it can also limit the blood flow to the brain through the carotid arteries which can cause a risk of stroke. [1]

Furthermore, with time, the arteries can be teared and seriously weakened. In the case of the aorta, the major artery that supplies the heart with oxygen-rich blood, some region can be seriously weakened causing a bulge in the artery. Moreover, the burst of this bulge can lead to serious internal bleeding. [1]

1.2 The treatments

The simplest treatment recommended by the doctors is a healthy lifestyle thanks to physical activities, to a healthy diet... Sometimes, just a healthy lifestyle can not be sufficient to control the formation of plaques in the arteries. Lots of other treatments can then be proposed such as medication or treatments that require surgeries.

In the case of the coronary artery disease either an angioplasty along or not with a stent implantation or a coronary artery bypass grafting are possible. The coronary artery bypass grafting surgery (Figure 1.3) consists on taking an artery or a veins from another region of the body in order to connect it to the blocked coronary artery. This connected artery or vein is then able to bypass the blocked region of the coronary artery creating a new route for the rich-oxygen blood to reach the heart. [11]

The angioplasty, also known as a per-cutaneous coronary intervention, consists of the placement of a flexible tube with a balloon in the blocked artery . The balloon is then inflated to

---

network of capillaries in a particular area or organ of the body. [8] [9]

[2] The coronary arteries are the arteries that supply the heart with oxygen-rich blood.[6]

compress the plaques against the wall of the blocked artery leading to the restoration of a correct blood flow in the vessel. When an angioplasty is performed alone, after the inflation of the balloon the surgery is finished. [1]

On the other hand, the angioplasty can be performed with a stent implantation as well. Specifically, a stent is placed in the blocked artery to sustain the artery's inner wall (Figure 1.4). Thanks to this little device, the probability that the artery becomes blocked or narrow again is largely reduced.[1]

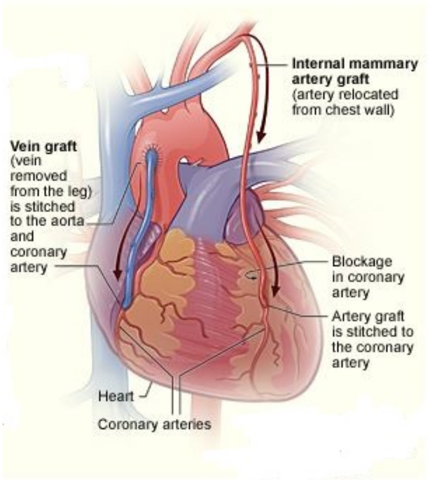

Figure 1.3: Schematic representation of the coronary artery bypass grafting [11]

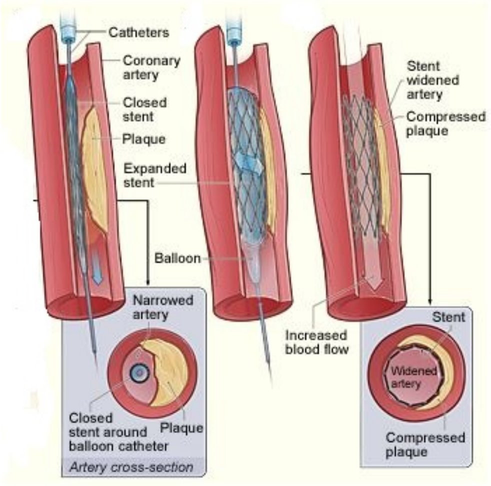

Figure 1.4: Schematic representation of the angioplasty along with the placement of a stent [1]

2 The implantation of a stent

In this work, the stress will be put on the implantation of stents as treatments for the artery diseases. A stent consists of a small mesh tube placed by surgery in blocked or narrow arteries to restore or improve the blood flow, to treat weak arteries and prevent them from bursting. [1]

The main steps of implantation of a stent can be resumed as follow (Figure 1.5). A catheter with a stent wrapped around a deflated balloon at its end is inserted into the blood vessel. Once the catheter reached the target blood vessel area, the inflation of the balloon causes the expansion of the stent and the stretching of the artery. Later on, when the expansion of the stent is complete, the balloon deflates and the catheter along with the balloon are removed. [12]

2.1 The self-expanding and balloon expandable stents

There are two main kinds of stents, namely, the self-expanding and the balloon expandable stents. They both differ from their properties and the way they are deployed during surgery. [13]

A self-expanding stent, which is manufactured at the size of the target blood vessel, is constrained to its smallest diameter until it reaches the intended site where the constrain is released and the stent deployed. Those stents have different attractive properties such as high radial strength [3] leading to a higher flexibility and a large conformability. Hence, they adapt their shape easily to the vessel and they do not force the vessel to the shape of the stent.

---

[3] The radial strength defines the pressure that the stent is able to withstand without causing any clinical damage. [13]

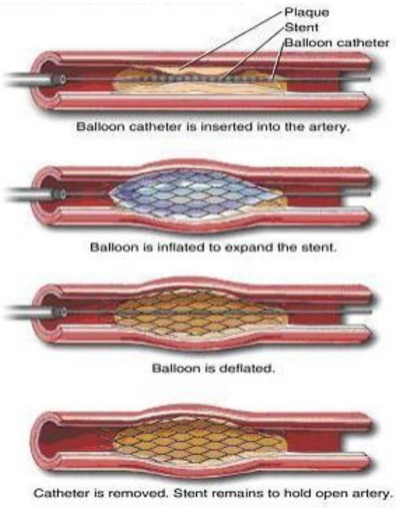

Figure 1.5: Schematic representation of the implantation of a stent [12]

The self-expanding stents present drawbacks. The presence of a recoil [4] due to the springback forces of the vessel, the presence of a remodeling of the vessel due to the continuous increase of the stent's diameter over time and the insecurity of the exact place of deployment will be the main drawbacks of this kind of stent. [13]

Next, a balloon expandable stent is expanded to the size of the vessel thanks to an inflating balloon. Hence, it plastically deforms the stent. The balloon expandable stent differs from the self-expanding one on several properties. First, they do not have the same radial strength, they collapse if the pressure reaches a critical level. Then they also differ on their stiffness, they are more or less, for the same design, three times stiffer than the self-expandable ones. On the opposite to the self-expanding one, even if they resist the balloon inflation, it has been demonstrated that they do much less recoil due to the springback forces of the vessel. Moreover, they do not increase their diameter with time, on the contrary, they can only decrease it and their site of deployment is more predictable. [13]

As a result, the self-expanding stent will be in harmony in the vessel whereas the balloon expandable will change the geometry of the anatomy of the vessel. Hence, self-expanding stents will assist the balloon expansion process while balloon expandable stents will resist it. [13]

2.2 A brief history

Even if the stents are currently used, they were created only in the late 1980's. At first, the angioplasty was done without a stent leading to a re-narrowing of the arteries. To provide solutions to those issues, several researches have been performed leading to the conception of the stents. [14]

The Wallstent was the very first stent implanted in a 63 year man in 1986 in Toulouse. This self-expanding, stainless steel stent was created by two Swedes namely, Wallsten and Senning. After the first tests running with the Wallstent, numerous patients had been suffering of late thrombosis complications. Because of those concerns, U.Sigwart, a cardiologist, developed new treatments of anticoagulants combining aspirin and other macromolecules. But even with those drugs, there remained 5 to 10% probability that those patients would suffer from a late thrombosis.

In 1987, Palmaz and Schatz conceived the first balloon expandable stent. This stent, also

---

[4] The acute recoil is defined as the reduction of the diameter of the stent just after the balloon deflation.[13]

made of stainless steel, was the most used in the 1990's. Several stents were then designed in the 1990's such as the Wiktor formed by a U-shuped tantalum wire [15] and the Flex-stent, a surgical stainless steel monofilament. [16] [14] [17]

Even if the main issues were reduced, there were still some serious drawbacks: the risk of thrombosis and the in-stent restenosis. The in-stent restenosis comes from the proliferation of cell tissue in the artery because of the presence of a foreign body (Figure 1.6).

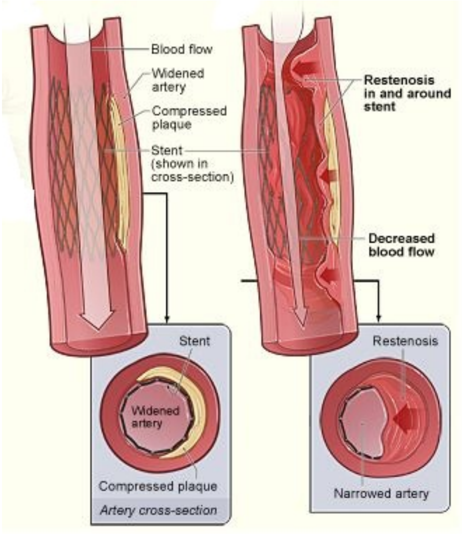

Figure 1.6: Schematic representation of the restonesis phenomena [1]

Due to those concerns, another generation of stents was born: the drug-eluting stents. This new generation consisted of bare metal stent coating with anti-proliferative drugs such as sirolimus or paclitaxel substances [5] that were released slowly for few weeks after the surgery. In 2002 the first sirolimus-eluting stent, Cypher, was implanted by Eduardo Sousa. Thanks to this in-drug delivery, a significant reduction of in-stent restonesis was possible. [14]

Unfortunately, in 2006, another issue emerged from this new stent generation : the late risk of thrombosis. This new concern seems to find its origin in the late endothelialization [6] of the artery.

In 2011 a totally new stent was born: the biodegradable scaffold. The idea was to provide a stent that could be resorbed after a certain amount of time following the surgery in order to free the blood vessel from any caging. Thanks to the disappearance of the material, the restoration of the endothelium, the vascular wall and the decrease of the risk of late thrombosis were possible. [17] [14] [19]

Nowadays, new kinds of biodegradable stents are being tested. Several designs have been proposed, but the main idea consists in a metallic stent with a drug-eluting coating. The main challenge of this biodegradable stent is to combine the degradation and the mechanical properties. While at first the degradation rate should be low and the mechanical properties high, later on an increase of the degradation rate and a decrease of the mechanical properties should be observed. It is considered that the degradation of the stent should be complete after 12 to 24 months while

---

[5] The Sirolimus substance is a derived compound from fungus that can be found in Rapa Nui, also known as the Easter island. The paclitaxel is an anti-cancer drug derived from the Pacific Yew tree, a conifer.[17]

[6] A significant injury and inflammation of the artery's inner wall can appear due to a stent implantation. The endothelialization process consists in repairing the inner wall. Specifically, the vascular wall and the endothelium which are damaged cause a process of reparation that depends on a whole process of migration of the endothelial cells. [18]

the mechanical properties should keep a sufficiently high level during 6 to 12 months during the remodelling of the artery. [20] [19]

In this work, the accent will be put on those biodegradable stents.

3 The specifications and material perspectives for stents

3.1 The specifications

The stent design is an important factor since it will influence its final properties and the several related drawbacks of such a surgery like the restenosis and the late thrombosis. [21] [22] [23]

The main design characteristics are presented below.

3.1.1 The flexibility

Even if the flexibility is not the principal characteristic for a stent implantation, it should still present a sufficient flexibility. Specifically, a too high flexibity can cause an excessive intimal hyperplasia [7]which has been proved to be linked with the risk of restenosis. [26]

The stent placed at the end of the catheter should be able to travel easily inside the different tortuous blood vessels and to pass through the different diameter of the blood vessels to finally arrive at the target location. After the expansion of the stent, it should maintain a non-flexing surface to promote the endothelial cells growth. [21] [22] [23]

3.1.2 The biocompatibility and thromboresistance

Whereas the flexibility relies on the stent design, the thromboresistance and the biocompatibility rely on the material itself, specifically on the surface properties of the material. There are two categories of biocompatiblity, namely, the early and late issues. The early biocompatibility issues are associated with inflammation, thrombosis and neointima formation. The late issues come from two different domains: the mechanical and the chemical domain. While the mechanical issues are connected to the failure due to the material fatigue, the chemical issues are linked with the release of potential toxic substances due to corrosion or depolymerization.[27]

For a biomedical application, the biocompatible material chosen should not encourage the platelet adhesion and deposition to be thromboresistive. The compatibility of the blood and the materials have been largely studied. In the case of the metals, two main categories can be extracted, namely, the electropositive and the electronegative metals. [23] [22]

The electropositively charged metals have a large resistance to corrosion and are thrombogenic because the blood elements are negatively charged. On the opposite, the electronegative charged metals have a smaller resistance to corrosion and are thromboresistant. Furthermore, the thrombogenicity of metals can be balanced by an improvement of the surface texture thanks to surface treatments. [21]

As a result, the metal stent should combine a low surface potential, a surface free of contaminants and a minimal surface area. [21]

3.1.3 The surface characteristics

The surface of a stent is an important parameter since it influences the thrombosis and neointimal hyperplasia. The surface characteristic should include the surface energy, the surface texture, the surface potential and the stability of the surface oxide layer. [23]

---

[7] The intimal hyperplasia is a thickening of the innermost layer of the artery called the tunica intima. More specifically, it is the response of a blood vessel to an injury.[24] [25]

The surface energy and surface chemistry of any material influences the wettability of the surface. Through several studies it has been demonstrated that the thrombogenicity of a material surface increases when the surface energy increases. Hence, they began to coat those high surface energy metals with polymers having a low surface energy.

The surface texture will be influenced by the polishing and coating step. Polishing the surface of the stent is an important step since the thrombogenicity is higher for rougher surfaces and the coatings influence the roughness of the surface as well. The surface texture control is very difficult since there are several morphological changes during the stent expansion.

The surface potential, as mentioned above for the biocompatibility, is related to the fact that most of the metals are electropositive while the blood is electronegative. Hence, this difference of charges accentuates the thrombogenicity. [23]

The stability of the surface oxide layer plays a crucial role in the release of the ions from the bulk materials underneath the surface : this surface oxide layer acts as a barrier. Again, the coatings are generally the most common solution to stabilize the surface.

Furthermore, even if the coatings were first used to increase the biocompatibility, they became later a platform for the control of the delivery of drugs to inhibit the intimal hyperplasia. Many coatings exist such as inorganic coating with gold or silicon-carbide, porous materials or even polymers like copolymers (PLGA, PU) or some biological polymers such as fibrin or hyaluronic acid (HA). [23]

3.1.4 The visibility

The visibility is a crucial property for the implantation of a stent. If this property is not fulfilled it could cause serious problems : the target area could be missed or the stent could fall from the end of the catheter during the intervention before reaching the targeted site. The stent should have the right radio-opacity and magnetic resonance imaging to assist the clinicians.

This criteria, even if important, is very difficult to meet and combine with the other criteria. For instance, metals such as platinum or gold which could improve the radio-opacity of the stent, lead to very poor properties and a higher cost. [21] [23]

3.1.5 The expandability

The expandability of a stent will depend on the type of stent used, self-expanding or balloon expandable. For both cases, the stent should undergo a sufficient expansion to conform the vessel's wall. [23]

A balloon expandable stent has a precise expansion due to the balloon inflation and needs to have sufficient plasticity to remain at the required size once it has been deployed.

A self-expanding stent has no precise expansion, there is a risk of undersizing that could cause the migration of the stent and embolization or a risk of oversizing that could cause an intimal trauma. Furthermore, those stents should have sufficient elasticity to sustain a large compression at first and then an expansion of a predetermined size. Moreover, after the expansion, the stent should have a sufficient radial hoop strength to be capable to maintain the required diameter and not to collapse. [21] [27] [23]

As a result, the stent should have a large expansion ratio. At first, the stent should be small enough to be placed at the end of the catheter and pass through the blood vessels. Then, it should be able to expand many times its original size to conform the vessel's wall. [21]

3.2 The material perspectives

Thanks to the previous specifications of the stents, the material selection can now be studied. Several solutions will be examined, namely the metallic permanent stent and the biodegradable stent.

3.2.1 The metallic permanent stents

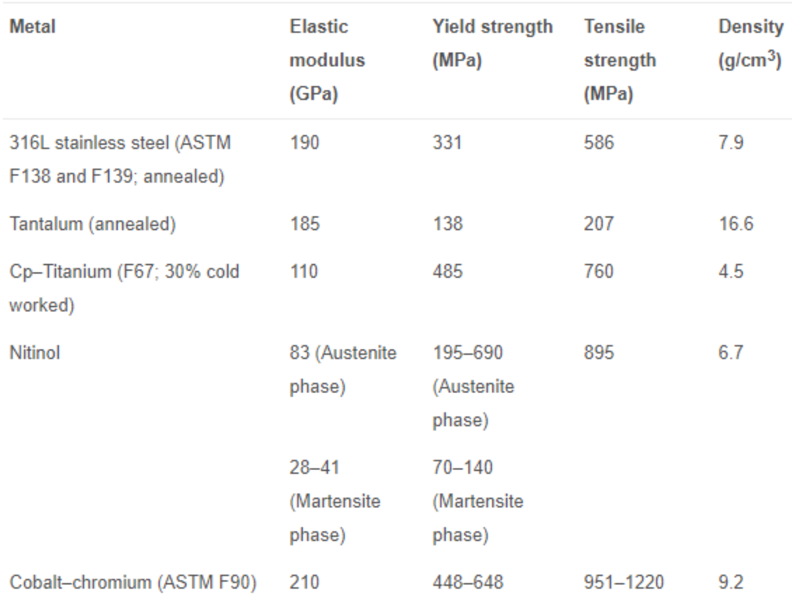

Metal	Elastic modulus (GPa)	Yield strength (MPa)	Tensile strength (MPa)	Density (g/cm^3)
316L stainless steel (ASTM F138 and F139; annealed)	190	331	586	7.9
Tantalum (annealed)	185	138	207	16.6
Cp–Titanium (F67; 30% cold worked)	110	485	760	4.5
Nitinol	83 (Austenite phase)	195–690 (Austenite phase)	895	6.7
	28–41 (Martensite phase)	70–140 (Martensite phase)		
Cobalt–chromium (ASTM F90)	210	448–648	951–1220	9.2

Figure 1.7: Mechanical properties of materials used to manufacture metallic stent [23]

Nowadays, several materials have been used to manufacture metallic permanent stents. The most common one is the 316L SS due to its well-suited mechanical properties (Figure 1.7) and its excellent corrosion resistance. Even with those excellent properties, this material has some drawbacks. The 316L SS has a ferromagnetic nature and a low density. These properties translate a non-MRI compatible and a poorly visible fluoroscopic material.[23]

The biocompatibility can be an issue because of the presence of nickel, chromium and molybdenum in the alloy. The ions of those elements, if released, can trigger local immune response and inflammatory reactions that may induce intimal hyperphlasia and in-stent restonesis. Moreover, the release of the nickel can lead to allergic reactions. As a result a lower nickel concentration will be preferred to decrease the allergic reactions, but a higher nickel content will be preferred to decrease the ferromagnetic properties in order to stabilize the iron in a non-magnetic state. Specifically, an optimal concentration of 10.5 % of nickel is promising. [23]

Furthermore, other solutions, like the addition of coatings, have been found to improve the biocompatibility and the visibility limitations. Elements like the tantalum (Ta) have been coated on the 316L SS to improve the corrosion properties and enhance the biocompatibility. The tantalum has a highly stable surface oxide layer that gives him excellent corrosion resistance and it also has a good biocompatibility. [23]

Moreover, Ta is an MRI compatible material and it has excellent fluoroscopic visibility due to its high density. Even with all those excellent properties compared to the 316L SS, the production of tantalum stents is much lower due to their poor mechanical properties. Indeed, by looking at its properties in Figure 1.7 it can be observed that its yield strength is very close to its tensile strength leading to a higher probability of those stent to break during the deployment. As a result, the pressure applied during the deployment will be lower causing a larger risk of recoiling. [23]

First used in the orthopedic and dental biomedical applications, the titanium (Ti) and its alloys are very interesting materials. The titanium has an excellent biocompatibility and an excellent corrosion resistance due to its stable surface oxide layer. Yet, the titanium is not commonly used to manufacture stent due to its low ductility and its higher probability of tensile failure when they expand to stress beyond their yield strength (Figure 1.7) which is one of the specifications of the balloon expandable stent. Hence, a solution is to alloy the titanium with elements that reduce its yield strength while maintaining the tensile properties. [23]

A famous alloy of titanium used to manufacture stents is the nitinol (Ni-Ti). This alloy of 49.5-57.5% of nickel and titanium as remaining component is used to make self-expanding stent due to their shape-memory property. Thanks to this effect, the stent is able to have a smaller diameter at room temperature and expand to a predetermined diameter at body temperature. Hence, the stent is plastically deformed at room temperature and regains its original shape after the implantation. The maximum strain recovery [8] of this alloy is about 8.5% after the plastic deformation. [23]

The nitinol alloy has good mechanical properties (Figure 1.7) for a stent application but the corrosion resistance is still debated. Through researches it has been demonstrated that the nitinol presents a good corrosion resistance comparable to the one of titanium or Ti-6Al-4V. This good corrosion resistance could come from the formation of a protective oxide film mainly constituted by titanium oxide. In addition, it has been demonstrated that the corrosion resistance is higher for nitinol than for 316L stainless steel but it is lower than the one of Ti-6AL-4V. [29]

The presence of the nickel and the risk of allergic reactions make this alloy non biocompatible. One of the solutions is to passivate the surface to increase the titane oxide concentration at the surface and decrease the nickel oxide concentration. Moreover, even if the Ni-Ti alloy is MRI compatible, it is not visible by fluoroscopy which is a serious drawback since the deployment of the stent is performed by fluoroscopy. [23]

Recently, a new alloy has been used to manufacture stents : the Co-Cr alloy. This alloy has high elastic modulus and an excellent radial strength (Figure1.7). As a result of those properties, this alloy is attractive to make very thin struts with increased strength. Moreover, it is MRI compatible and radio-opaque. [23]

3.2.2 The biodegradable stents

These days, the key element in the researches is to develop devices that are strong, durable and accepted by the body. In the case of the stent implantation, the permanent implant have serious drawbacks : long-term endothelial dysfunction, delayed re-endothelialization, thrombogenicity, chronic inflammatory local reactions ... Moreover, since the major effect of a stent is its deployment it is then required to be implanted only for 6-12 months which is the time period required for the artery remodeling and healing achievement. Hence, after those 6-12 months, the stent has no longer a beneficial effect. As a result the studies are now mainly focused on the biodegradable stents.

The material used to manufacture biodegradable stent should fulfill the same requirements as the previous stent, but also some special requirements : the material and its degradation products should be biocompatible; the stent should stay in the target site and sustain a sufficient radial force for the scaffolding effect during the required period. In order to meet those specifications,

---

[8] When a material is deformed plastically (beyond the yield point), and the stress applied is then released, the material ends up with a permanent strain. Furthermore, if the stress is reapplied, the material will again respond elastically up to a new yield point that will be higher than the original yield point. Hence, the elastic strain recovery corresponds to the amount of elastic strain that it takes before reaching the new yield point. [28]

three materials were studied : the polymers, the magnesium and the iron. [30] [23]

3.2.2.1 The polymeric stents

The stents made of polymer materials will be referred as biodegradable polymers. Specifically, most of the biodegradable polymer stents will be based on polyesters due to their tailorable biodegradability. Since unprocessed polyesters such as poly-L-Lactic acid (PLLA) have a tensile modulus typically 100-fold lower than the one of cobalt or stainless steel material, they will require up to 240% thicker struts to match with the current metallic drug-eluting stents. [31]

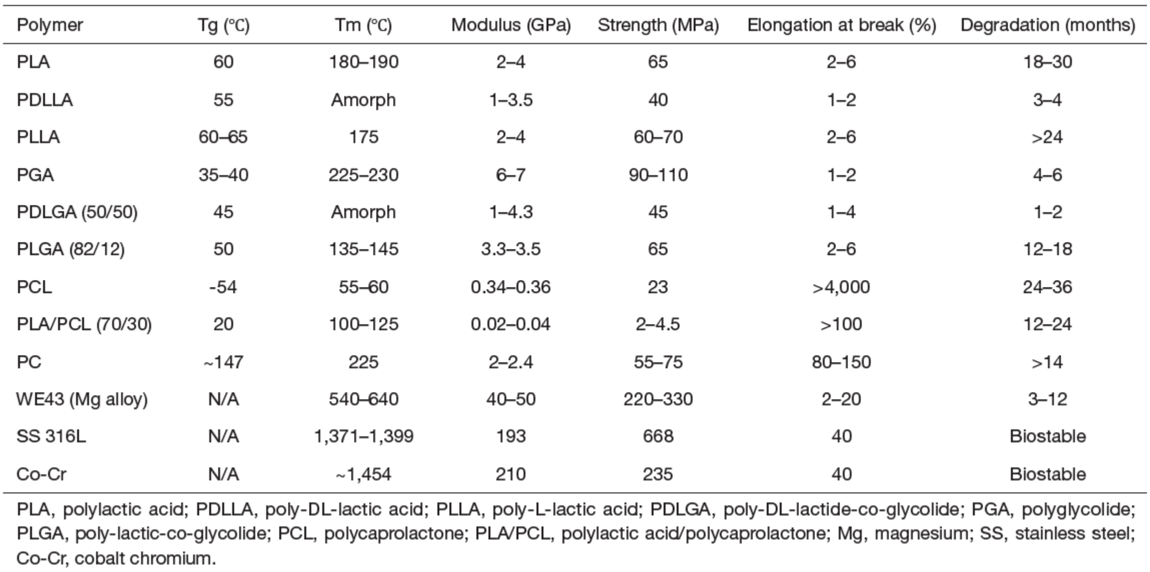

Polymer	Tg (°C)	Tm (°C)	Modulus (GPa)	Strength (MPa)	Elongation at break (%)	Degradation (months)
PLA	60	180–190	2–4	65	2–6	18–30
PDLLA	55	Amorph	1–3.5	40	1–2	3–4
PLLA	60–65	175	2–4	60–70	2–6	>24
PGA	35–40	225–230	6–7	90–110	1–2	4–6
PDLGA (50/50)	45	Amorph	1–4.3	45	1–4	1–2
PLGA (82/12)	50	135–145	3.3–3.5	65	2–6	12–18
PCL	-54	55–60	0.34–0.36	23	>4,000	24–36
PLA/PCL (70/30)	20	100–125	0.02–0.04	2–4.5	>100	12–24
PC	~147	225	2–2.4	55–75	80–150	>14
WE43 (Mg alloy)	N/A	540–640	40–50	220–330	2–20	3–12
SS 316L	N/A	1,371–1,399	193	668	40	Biostable
Co-Cr	N/A	~1,454	210	235	40	Biostable

PLA, polylactic acid; PDLLA, poly-DL-lactic acid; PLLA, poly-L-lactic acid; PDLGA, poly-DL-lactide-co-glycolide; PGA, polyglycolide; PLGA, poly-lactic-co-glycolide; PCL, polycaprolactone; PLA/PCL, polylactic acid/polycaprolactone; Mg, magnesium; SS, stainless steel; Co-Cr, cobalt chromium.

Figure 1.8: Mechanical and physical properties of the polymeric and metallic stents [31]

Several polymers have been explored as potential material for drug eluting stent, namely, the PLLA, poly-DL-lactic acid (PDLLA), polycarbonate (PC), poly(lactide-co-glycolide) (PLGA) and polycaprolactone (PCL). In Figure 1.8, the characteristics of those polymers are presented. Compared to the metallic-based stent, the thickness of the struts is largely higher for the polymer-based. In addition, most of the mechanical properties including the modulus, strength and the elongation at break seem to be much higher for the metallic-based stent.

First, by comparing the polyglycolide (PGA) with the PLLA, it can be observed that PGA has a higher strength and stiffness than PLLA. But the low ductility and the difficulty in processing material the PGA makes it unsuitable for a drug-eluting stent fabrication.

Then, the fabrication of PLGA by random copolymerization of PLA and PGA affects its properties by the addition of methyl groups. Hence, it increases its hydrophobicity and alters its degradation time.

The polycaprolactone, a semi-crystalline polymer, has a higher flexibility than the PLLA but a lower tensile modulus and strength due to its lower crystallinity.

Moreover, the PLLA is the most commonly used polymer material for the biodegradable stent fabrication. Indeed, it has a higher tensile strength and modulus than PDLA and PCL and a slower absorption time than PLGA. PLLA is more hydrophobic and stable against hydrolysis compared to the PGA thanks to its additional methyl group. In addition, it is biologically inert, biocompatible and it is widely used in different biomedical applications such as in sutures or tissue engineering scaffolds. Common biodegaradable PLLA based stent include ABSORB bioresorbable vascular scaffold (BVS) (Abbot Vascular), DESolve (Elixir Medical), MIRAGE

(Manli Cardiology), etc.[31]

Since the PLLA is the most polymer material used to fabricate biodegradable stent, the next section section will mainly focus on its mechanical and degradation properties.

3.2.2.2 Degradation properties

There are three main stages of degradation of the PLLA via hydrolysis. This hydrolysis process is a biomolecular nucleophilic substitution reaction catalyzed by the presence of acids or bases.

First, the molecular weight will decrease with the hydrolysis of the amorphous polymer tie chains. Since the amorphous segments are less packed and hydrophilic carboxylic acid end group are present, the amorphous segments will be more susceptible to hydrolysis. Hence, there will be a small effect on the mechanical performance.

Then, there will be a scission between the amorphous tie chains and the crystalline regions causing a decrease in the mechanical strength. In this second stage, the polymer is fragmented into low weight oligomers. Moreover, mass loss, cracks and structural discontinuities will be observed.

In the last stage, the monomer will be transformed into pyruvate [9] which will enter into a Krebs cycle [10] and then converted into carbon dioxide and water. The final bioresorption of the polymer will take place thanks to the excretion of the end products from the body through the kidneys or lungs. [31]

3.2.2.3 Mechanical properties

Poly-L-Lactic acid (PLLA) is a semi-crystalline polymer with a maximum of 70% of crystallinity. It has the highest glass transition temperature T_g [11]. Although it has relatively high tensile properties among the biodegradable polymers, the unprocessed PLLA has a lower mechanical strength compared to conventional metals used for drug-eluting stents fabrication. In addition, the PLLA stents have a limit of expansion and can fracture as well due to over-dilatation. Hence, improvements of the expandability while maintaining a good radial strength are the main focus for the biodegradable polymeric stents. [31]

Nowadays, the Abbot Vascular's Everolimus-eluting ABSORB biodegradable stent is the most commonly used. Furthermore, it was the very first biodegradable stent to achieve the FDA's approval [12].

In a study performed by Ormiston et al. [35], a comparison between metallic drug-eluting stent and two PLLA based biodegradable stents was performed. The three studied stents and their properties are shown in Figure 1.9. From this experiment, they demonstrated that even if the ML8/Xpedition drug-eluting stent and the Absorb biodegradable exhibited similar recoil properties, the ML8/Xpedition showed a higher radial strength (Figure 1.10).

---

[9] The pyruvate corresponds to the anionic form of the pyruvic acid.[32]

[10] "*The citric acid cycle (CAC) – also known as the tricarboxylic acid (TCA) cycle or the Krebs cycle is a series of chemical reactions used by all aerobic organisms to release stored energy through the oxidation of acetyl-CoA derived from carbohydrates, fats, and proteins into carbon dioxide and chemical energy in the form of adenosine triphosphate (ATP).*"[33]

[11] The glass transition temperature of a polymer is defined as the temperature at which the reversible transition in amorphous regions within a semi-crystalline polymer from a hard and relatively brittle state into a viscous rubbery state occurs. [31]

[12] The U.S. Food and Drug Administration (FDA) is an organisation that examines, tests and approves wide range of medical items such as drugs and medical appliances. When a medical item is "FDA approval", it means that the FDA organisation has recognised the benefits of the approved item and outweigh the potential risks for the item's planned use. [34]

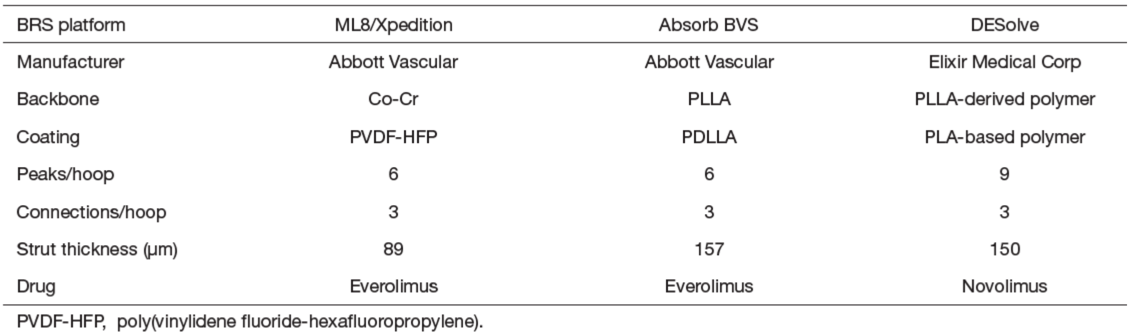

BRS platform	ML8/Xpedition	Absorb BVS	DESolve
Manufacturer	Abbott Vascular	Abbott Vascular	Elixir Medical Corp
Backbone	Co-Cr	PLLA	PLLA-derived polymer
Coating	PVDF-HFP	PDLLA	PLA-based polymer
Peaks/hoop	6	6	9
Connections/hoop	3	3	3
Strut thickness (µm)	89	157	150
Drug	Everolimus	Everolimus	Novolimus

PVDF-HFP, poly(vinylidene fluoride-hexafluoropropylene).

Figure 1.9: Description of the stents taken in the study of Ormestion et al.[35] [31]

By comparison with the two PLLA-based stents, it can be noticed that the DESolve has a lower radial strength (Figure 1.10) and presents an ability to offset any initial recoiling of the device within the first few hours after implantation as the unconstrained device expands towards its nominal diameter. In addition, it seems that compared to the PLLA-based stents, the metallic drug-eluting has higher safety threshold in various post-dilatation strategies.

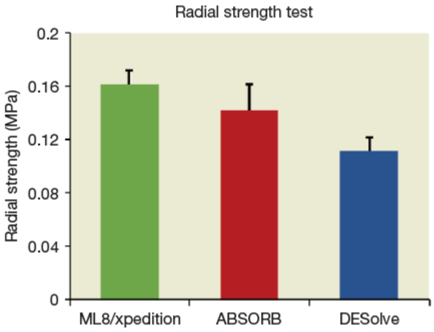

Figure 1.10: Comparison of the radial strength for the three stents studied in the Ormestion et al. study [35] [31]

Moreover, as in Figure 1.8, it can be noticed that the strut thickness is much more higher for a polymeric-based stent than for a metallic one.

3.2.2.4 The magnesium-based biodegradable stents

The magnesium (Mg) is an attractive material for biodegradable implants like orthopedic implants because of its low thrombogenicity and its good biocompatibility. Magnesium, like iron, is an important element to life since it is a structural constituent of the tissues. The properties of magnesium and more specifically its mechanical and corrosion properties are not suitable for stent applications. As the degradation of magnesium is too quick, it results in a lost of the mechanical properties and a tissue overload with the degradation products. The magnesium needs to be alloyed with other elements such as Al, Mn, and rare earth elements to decrease its degradation rate.

Furthermore, the properties of magnesium like the properties of iron can be modified by alloying elements. Specifically, the lithium enhances the ductility and the formability of magnesium alloys, the zirconium is an effective grain-refining agent in Al-free magnesium alloys which contributes to the grain boundary strengthening, calcium improves the strength of the alloy and the creep resistance and act as a grain refining-agent.

In 1878, it was the very first time that magnesium was used in a biomedical applications: a Mg wire ligature was used to stop bleeding vessels by Huse. Later, during the 21th century, Heublein and al. [36] [37] were the first to investigate the magnesium alloys for cardiovascular

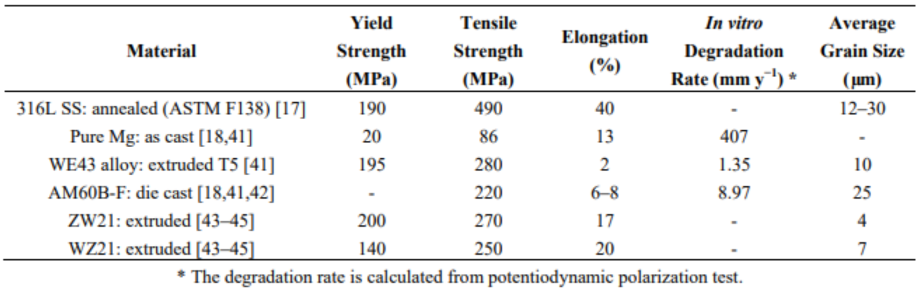

Material	Yield Strength (MPa)	Tensile Strength (MPa)	Elongation (%)	*In vitro* Degradation Rate (mm y^{-1}) *	Average Grain Size (μm)
316L SS: annealed (ASTM F138) [17]	190	490	40	-	12–30
Pure Mg: as cast [18,41]	20	86	13	407	-
WE43 alloy: extruded T5 [41]	195	280	2	1.35	10
AM60B-F: die cast [18,41,42]	-	220	6–8	8.97	25
ZW21: extruded [43–45]	200	270	17	-	4
WZ21: extruded [43–45]	140	250	20	-	7

* The degradation rate is calculated from potentiodynamic polarization test.

Figure 1.11: Mechanical properties of materials used to manufacture magnesium biodegradable stent [30]

stents. They chose the AE21 alloy of magnesium, which is composed of 2% aluminum, 1% of rare earth metals and magnesium as remaining component because of its lower degradation rate. The main disadvantage of this alloy is its neointimal response and its faster degradation rate than expected. As a result, they concluded that improvements on the degradation rates and the mechanical stability over a predetermined time needed to be further investigated. [30]

Another alloy of magnesium was then investigated by Di Mario et al. [38]: the WE43 alloy(Figure 1.11). This alloy made of 4% yttrium, 0.6% zirconium, 3.4% rare earth metals and magnesium as remaining component, has a poor radial strength because of its low elastic modulus ($E = 44GPa$ [23]). In their study, they have implanted, in 33 mini-pigs, a WE43 stent in their coronary arteries. The results showed no symptoms of allergic or toxic reactions. Yet, a recent study on 60 patients, showed that even if it is a biodegradable stent that can be implanted safely, the specifications are not met in the long-term angioplasty.

Zartner and al. [39] were the first to successfully implant a biodegradable metal stent on a baby with a congenital heart disease. The magnesium stent of 3mm diameter and 10 mm in length was placed in his left pulmonary artery. This experiment showed a complete degradation after 5 months and there was no in-stent obstruction observed.

Later on, in 2006, Waksman et al. [40] studied the safety and the efficiency of this biodegradable WE43 stent in the coronary arteries of pigs during 3 months. The results showed no evidence of stent particle embolization, thrombosis, excess of inflammation and the neointimal area was much smaller in this magnesium alloy than with a stainless steel stent. The conclusion was that magnesium alloy stents are safe and associated with less neointima formation, even if this reduction of intima did not result in larger lumen.

In 2007, this alloy was tested in the coronary arteries of 63 patients. The study demonstrated that biodegradable magnesium stents can achieve an angiographic result similar to the ones of other metal stents and could be biodegraded after 4 months. Even with those promising results some points still need to be improved: the prolongation of the degradation and the possibility to add a drug-elution function to the stent. [30]

Biodegradable polymers such as the PLGA and the PLLA have been coated to the Mg alloys in order to control the biodegradation. Those polymers were coated in their blank form or mixed with drugs. The drugs contained in the polymer coating can be released either from the stent coating diffusion or during the polymer breakdown. When the drug is released thanks to a diffusion-controlled mechanism, two different formulations can occur. In reservoir devices, the drug reservoir is covered with a thin layer of polymer that acts as a rate-controlling membrane. In matrix devices, the drug is dispersed inside a polymer matrix and released into the environment without rate-controlling barrier layer. On the other hand, a degradation-controlled drug release is based on the degradation of a polymer membrane that encapsulates the drug reservoir or a drug containing polymer matrix itself. [41]

Lu et al. [42] manufactured a biodegradable AZ81 Mg alloy stent coated with a composite multi-layer film for the control of the degradation rate and the drug release rate. The result of their study showed an increase of the corrosion resistance and the control of the biodegradation rate. [30]

Recently, new alloys of magnesium ZW21 and WZ21 (Figure 1.11) containing Zn, Y, Ca and Mn showed fine structure and generate exceptional plasticity of 17% and 20% respectively at ambient temperature which make them very attractive for stent applications. Moreover, the result showed that those alloys have a homogenized corrosion and their corrosion resistance is higher than the one of other magnesium alloys. [30]

3.2.2.5 The iron-based biodegradable stents

Iron is an essential element to life but like everything else, its excess or deficiency can lead to serious damage. Iron has excellent mechanical properties (Figure 1.12), including a high radial strength due to its high elastic modulus and a high ductility which is helpful when the stent is plastically deformed during the implantation. Iron has some drawbacks: since the yield strength and tensile strength are close to each other, there is a slight probability that the stent fractures during the deployment. Moreover, the biodegradation of the iron involves the oxidation of iron into ferrous Fe^{3+} and ferric Fe^{2+} ions that will interact with the biological media. [23][30]

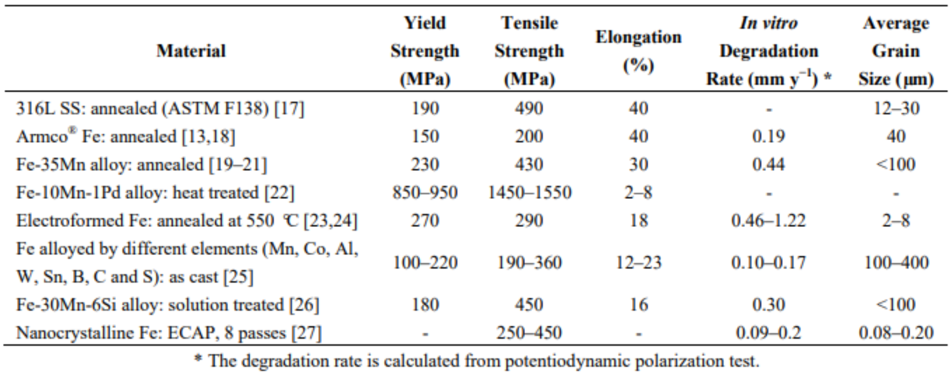

Material	**Yield Strength (MPa)**	**Tensile Strength (MPa)**	**Elongation (%)**	***In vitro* Degradation Rate (mm y^{-1}) ***	**Average Grain Size (μm)**
316L SS: annealed (ASTM F138) [17]	190	490	40	-	12–30
Armco® Fe: annealed [13,18]	150	200	40	0.19	40
Fe-35Mn alloy: annealed [19–21]	230	430	30	0.44	<100
Fe-10Mn-1Pd alloy: heat treated [22]	850–950	1450–1550	2–8	-	-
Electroformed Fe: annealed at 550 ℃ [23,24]	270	290	18	0.46–1.22	2–8
Fe alloyed by different elements (Mn, Co, Al, W, Sn, B, C and S): as cast [25]	100–220	190–360	12–23	0.10–0.17	100–400
Fe-30Mn-6Si alloy: solution treated [26]	180	450	16	0.30	<100
Nanocrystalline Fe: ECAP, 8 passes [27]	-	250–450	-	0.09–0.2	0.08–0.20

* The degradation rate is calculated from potentiodynamic polarization test.

Figure 1.12: Mechanical properties of materials used to manufacture iron biodegradable stent and the 316L SS [30]

In 2001, the very first biodegradable metallic stent fabricated from Armco iron ($Fe > 99.8\%$) was implanted in the aorta of white rabbits. The results showed that there was no significant evidence of inflammatory response, neointimal proliferation or systematic toxicity. Also it has been observed that the mechanical properties were maintained during the implantation without any failure. Yet, the results showed a slower degradation rate than required. The future researches focused then on the acceleration of the degradation rate thanks to the development of new alloys and changes on the microstructure.

The first to study the effect of the alloying elements on the properties of the biodegradable iron were Hermawan et al. [43] [44] [45] In this study, the goal was to produce an antiferromagnetic Fe-Mn alloy that is MRI compatible, has mechanical properties in the order of the 316L SS and a higher degradation rate. During their researches, they took the manganese (Mn) as the alloying element with contents from 20 to 35 wt%. The alloys Fe-30Mn and Fe-35Mn (Figure 1.12) showed single austenitic phase with mechanical properties comparable to the one of the 316L SS and a degradation rate more than twice the one of the Armco iron. These alloys were then suggested for further in-vitro and in-vivo studies.

Other studies performed by Schinhammer et al. [46] were then performed on Fe-based alloys with Mn and paladium (Pd) as alloying elements in order to change the electrochemicallity of the

Fe and control the formation of noble intermetallic phases. The intermetallic phases deployed were proved to be responsible of the increase of the degradation rate and the enhancement of the strength. The alloy Fe-10Mn-1Pd (Figure 1.12) revealed a degradation resistance of one order magnitude lower and mechanical properties that are adjustable thanks to the choice of alloying elements and the heat treatments. [30]

Moreover, other elements than Mn and Pd were investigated by Liu et al. [47] Specifically, they studied the Mn, Co, W, B, C, Sn, Al and S. The results showed that while Mn, Co, W, B, C and S improved the yield and ultimate strength of iron (Figure 1.12), the Sn reduced the mechanical properties. Furthermore, the corrosion results showed localized corrosion and the corrosion rates were about the same order of magnitude as pure iron. As a result, only Co, W, C and S were considered as suitable for the stent application since those alloying elements improve the mechanical properties and the corrosion rates and have a good biocompatibility.

In another study, Liu et al. [48] developed a new shape memory alloy : Fe-30Mn-6Si. This alloy consists at room temperature in $\epsilon - martensite$ and $\gamma - austenite$ phases. Compared to the Fe-30Mn alloy and the pure iron, it has better mechanical properties (Figure 1.12) and has higher corrosion rates than the Fe-30Mn.

On the other hand, studies began to focus on the degradation rate thanks to microstructural changes. The main idea of Nie and al. [49] was to fabricate nanocrystalline pure iron rods by the equal channel angular pressure technique [13]. However, the results proved that this nanocrystalline (Figure 1.12) iron show a stronger corrosion resistance than the one of the microcrystalline pure iron after severe plastic deformation.[30]

In conclusion, the stent has several stringent specifications such as a good biocompatibility and thrombo-resistance. Furthermore, different materials have been currently tested for the stent fabrication.

The metallic permanent stents that do not biodegrade are mainly made of 316L SS which presents good mechanical properties and good corrosion resistance but poor biocompatibility due to the presence of alloying elements. Other permanent metallic stents are, for example, titanium, nitinol or Co-Cr.

The biodegradable stents are made either with polymers or with metallic alloys. The PLLA is the most common polymeric biodegradable stents. It is inert and has a good biocompatibility but the polymeric stents lead to thicker struts due to their lower properties compared with metals. The most studied metallic biodegradable stents are the iron and magnesium-based alloys. While the degradation of the Armco iron is too slow, the degradation of the magnesium is too quick. In order to tailor the degradation time, studies on the effect of alloying elements have been performed.

4 Transformation-induced plasticity (TRIP) effects and the austenite properties

In this work a transformation-induced plasticity (TRIP) maraging alloy of Fe-9Mn-3Ni-1.4Al-0.01C will be investigated. First, the theoretical aspect of the TRIP and the maraging steels will be reviewed. Later on, the properties of the TRIP maraging steel and the austenitic phase will be detailed.

---

[13] *"Equal channel angular extrusion (ECAE, sometimes called Equal channel angular pressing, ECAP) was developed in the 1970s. In this process, a metal billet is pressed through an angled (typically 90 degrees) channel. To achieve optimal results, the process may be repeated several times, changing the orientation of the billet with each pass. This produces a uniform shear throughout the bulk of the material"*. Hence, this technique allows the production of ultrafine grain or even nanocrystalline structure. [50]

4.1 Transformation-induced plasticity (TRIP)

The transformation-induced plasticity steel consists in a combination of strength and ductility (Figure 1.13) as a result of their particular microstructure. There are two main kinds of TRIP steels: the TRIP steels which have a fully austenitic microstructure and contain several alloying elements that stabilize the austenite, and the TRIP-assisted steel, as part of the third generation of high strength steel [51], where only a small part of the microstructure is austenite and the rest is composed of ferrite, bainite or martensite depending on the composition of the alloy and the processing treatments performed. [52] [53]

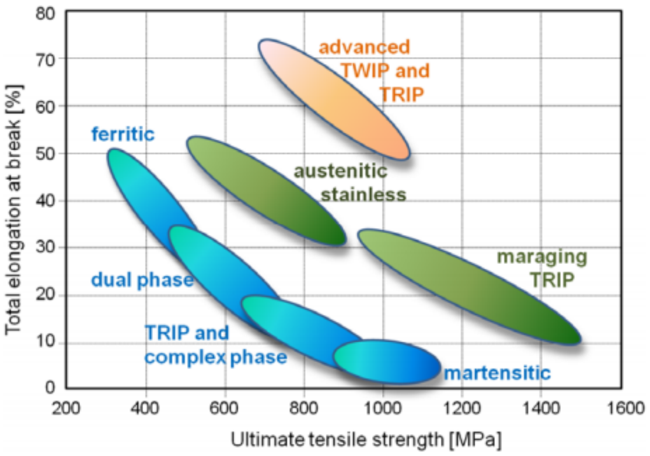

Figure 1.13: Schematic comparison of the mechanical properties of the TRIP, TWIP and the TRIP maraging steel [54]

The austenite present in the TRIP steel will transform into martensite upon mechanical loading. More specifically, when the steel is loaded, it will first undergo a conventional dislocation plasticity of the soft portions, the ferrite. Thereafter, when the deformation is further increased, the retained austenite [14] begins to transform into martensite causing an increase of the work hardening rate at higher strain levels. Moreover, because the TRIP steels show a high strain hardening capacity, they increase their mechanical properties and more specifically, they increase their yield strength. [55][56]

In Figure 1.14, the schematic representation of the transformation into martensite can be observed. During the straining, the retained austenite will transform into martensite. Hence, the austenite is then replaced by a high strength martensite and this transformation is associated with a volume expansion. As a result, the plastic instability is suppressed and the range of uniform elongation is extended. [57]

During a phase transformation of a certain area, or micro-region, of the material, a change of volume and a change of shape cause an eigenstress state [15] from grain to grain and even within a grain of a polycrystal to compensate the difference between the micro-region and the original one. Most commonly, this misfit causes a plastification of the area next to the micro-region and even sometimes, the plastification of this changing area. The superposition of the eigenstress state and the stress applied that induce this state can cause plastification. The macroscopic deformation of the specimen and the phase transformation define the TRIP effect. [59]

Moreover, the plastic flow behaviour of the material is controlled by two factors, namely, the

---

[14] The retained austenite simply consists in the remaining austenite at ambient temperature after the transformation into martensite through heat treatments.

[15] An eigenstress state describes a self-equilibrated transformation stress field that generates equivalent perturbed stress and strain distributions caused by one or several eigenstrains in the body which are free of any other external forces and surface constraints. Hence, the eigenstress field is created by the incompatibility of the eigenstrain field. The eigenstrain field represents induced strains due to misfit of inhomogeneities, thermal expansion,etc. [58]

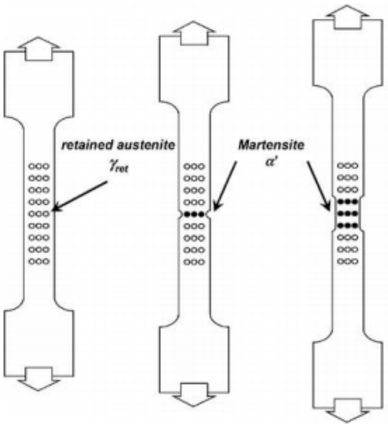

Figure 1.14: Schematic representation of the martensitic transformation induced by loading [57]

dynamic softening and the static hardening. The dynamic softening, dominant at low strains, arise from the plastic straining due to the dilatation effect upon the formation of martensitic grains. The static hardening, related to the fraction of martensite formed, is caused by the increasing volume fraction of the harder martensitic phase. [60]

Furthemore, the martensitic transformation is a displacive transformation. In other words, this transformation occurs by a homogeneous transformation of the crystal structure. The martensitic transformation can either be triggered by a temperature or by stress or strain applied. If it is induced by temperature, the martensitic temperature starts upon cooling at a particular temperature, the martensite start temperature, M_s.

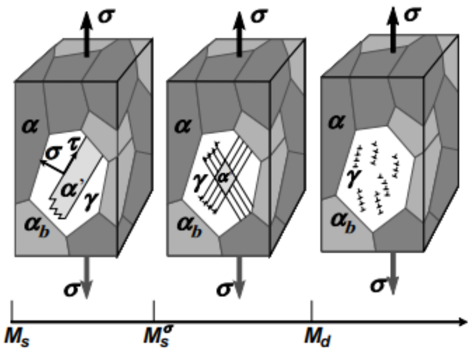

Figure 1.15: Schematic representation of the martensitic transformation depending on the temperature [57]

On the other hand, the temperature of the formation of the martensite can be higher than M_s if the transformation is induced by stress or strain. But, the higher the temperature will be, the higher the stress will be required. Moreover, the martensitic transformation can only be induced in a temperature range between $M_s - M_d$ where M_d represents the maximum temperature at which the martensite can be formed, above M_d, the austenite will only deform plastically [16]. [52]

Specifically, the dominant deformation mechanisms for different temperature ranges in the retained austenite in TRIP steel are presented in Figure 1.15. When the temperature is between M_S and M_S^g, the transformation of austenite into martensite is by stress-induced transformation

---

[16] As a reminder, plastic deformation of crystalline materials occurs by slip. This slip corresponds to the sliding of planes of atoms over one another by dislocations movements. The specific planes and shear directions of this slip are called slip planes and slip directions. Those planes and directions will be characteristic of the crystal structure.[61]

via preexisting nucleation site. The temperature M_S^g is defined as the temperature where the stress required to initiate the martensitic transformation equals the yield strength of the γ parent phase. As previously said, the stress required for this transformation will increase with the increasing temperature since the chemical driving force decreases. [57]

When the temperature is between M_S^g and M_d, the austenite will be strained. The martensite will be nucleated at new nucleation sites produced by slip. Hence, the transformation is mainly stress-induced. Moreover, additional nucleation occurs at the intersection of stress-induced deformation bands. Furthermore, the martensite formation in steels containing austenite between a temperature range of $M_s - M_d$ during plastic deformation helps to maintain the strain hardening. It is this local strain hardening that delays the onset of necking and lead to a large and uniform elongation. [52][57]

When the temperature is higher than M_d, there will be a higher stacking fault energy and a lower driving force for transformation. Hence, no transformation occurs as a result of straining. [57]

4.2 Retainded austenite and the stability of the austenite

The TRIP steel is able to combine several excellent mechanical properties such as high strength, high ductility and high fatigue resistance thanks to the transformation of austenite into martensite upon straining. The stability of the austenite, hence its resistance to the transformation upon stress, strain and temperature is an important parameter for this TRIP effect. The stability of the austenite should be enough to transform progressively during the deformation in order to accommodate the damages at all stages of the deformation. [52] In other words, if the retained austenite (RA) is overstabilised it restricts its transformation into martensite without the desirable TRIP effect. On the opposite, the instability of the RA causes the easy transformation of RA into martensite at the early stages of deformation and will not provide the TRIP effect at higher strains. [60]

The stability of the retained austenite combines the mechanical and the chemical stabilities of austenite. The chemical stability of austenite depends mainly on the composition of steel, and more specifically, the concentration of the stabilizing elements in the austenite. One of the main elements influencing the austenite stability is the carbon. Austenite grains with a small amount of carbon will tend to transform at low strain levels whereas a large amount of carbon prevents the austenite to transform at all. [60] Hence, increasing the carbon content decreases the driving force for the martensitic transformation. [52] As a result, the carbon is an austenite stabiliser. But not only the carbon in the retained austenite will play a role in the TRIP effect. [60]

Other elements will also influence the stability of the retained austenite. Aluminum and phosphorous decrease the activity coefficient of the carbon, inhibit the cementite precipitation and increase the solubility of the carbon in the ferrite, leading to a high enrichment of carbon in the retained austenite. Aluminum can also present deleterious effects, it can decrease the stability of the retained austenite by increasing the M_s temperature. While phosphorous can strengthen the ferrite, aluminum cannot. Another important alloying element of the TRIP-assisted steel is silicon, a ferrite stabiliser. Silicon helps to retain the carbon-enriched austenite by suppressing the cementite precipitation from austenite, it strengthens the ferrite enhancing the overall strength of the steel. [52] Manganese is another influencing element, it is a solid solution hardener and it is also an austenite stabilizer. Hence, it reduces the M_s and the activity of carbon in the austenite. Nickel, as well as manganese, is an austenite stabiliser and a solid solution harderner. But the addition of nickel can be very expensive.[60]

The mechanical stability of the austenite is governed by several factors such as the grain size, the microstructure, the nature of the neighbouring phase, defect structure ... The austenite's grain size is inversely proportional to its stability, the smaller the grain the higher the stability.

This observation is due to a resultant lowering of M_s and a decrease in the number of martensite nucleation sites in each grain. [62] [60] More specifically, whereas coarse grains of austenite are unstable and transform into martensite at low strains providing a limited contribution to the ductility, the very fine grains of austenite do not transform into martensite even at fracture making themselves useless for the TRIP effect. [60]

The properties of the surrounding phases, matrix, influence, like in the case of a composite material, the stress and strain carried by the austenite for a given total strain level. As a result, several properties of the surrounding phases like their size and shape will influence the transformation behaviour of the austenite. More specifically, when the austenite is surrounded by a soft phase like ferrite, it will experience more of the global stress and strain applied than when it is surrounded by a harder phase like bainite.

Furthermore, the properties of the austenite phase itself will influence its stability. The morphology and the orientation of the retained austenite are the main factors. Several morphologies have been observed in TRIP steels such as a microstructure composed of discrete particles of retained austenite between equiaxed ferrite grains (Figure 1.16) in the case of a two-stage heat treatment and thin layers of austenite between bainite sheaves or as thicker lamellar shape (Figure 1.17) when other heat treatments are performed. [62]

In addition, it has been demonstrated that the equiaxed microstructure shows a higher strength and a higher work hardening rate at low strains and decays quickly. On the other hand, the lamellar microstructre presents a superior work hardening behaviour at higher strains. Hence, the lamellar microstructure produces a slower rate of transformation than the one of the equiaxed microstructure. As a result of the slower rate of transformation in the lamellar microstructure, work hardening can persist at high strains where the transformation effect has already been exhausted in the case of the equiaxed microstructure. Those differences can be attributed to the location, carbon content and size of the retained austenite grains in the different TRIP microstructure. [62]

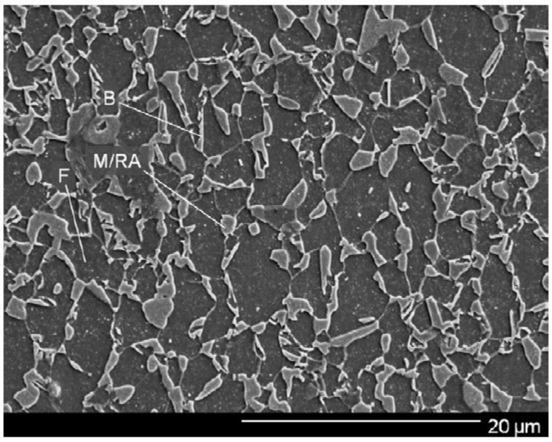

Figure 1.16: SEM micrograph of equiaxed microstructure with B, bainite, F, ferrite and M/RA martensite/retained austenite [62]

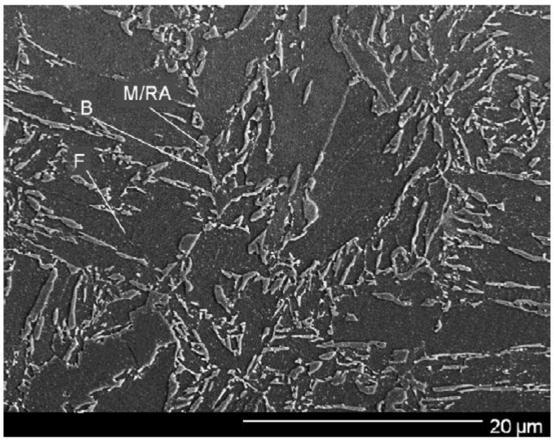

Figure 1.17: SEM micrograph of lamellar microstructure with B, bainite, F, ferrite and M/RA martensite/retained austenite [62]

The effect of the orientation of the retained austenite on its stability has been less studied than the other factors. But Reisner et al. showed that the martensite variants with the largest mechanical driving force is the one that is favoured. Another study performed by Tirumalasetty et al. has shown that the retained austenite crystals with the highest Schmid factor [17] and

---

[17] Schmid found that when a crystal is stressed, the slip will begin only when the shear stress on a slip system reaches a critical value τ_c. The Schmid's law in uniaxial tension can be written as : $\tau_c = \sigma m$ where m is the Schmid factor and it is defined as $m = cos\lambda cos\phi$ where λ is the angle between the slip direction and the tensile axis and ϕ the angle between the tensile axis and the slip-plane normal. [61]

embedded in ferrite undergo first a rotation that causes the lowering of their Schmid factor and causes the delays of their strain-induced transformation. [60]

4.3 The maraging steel

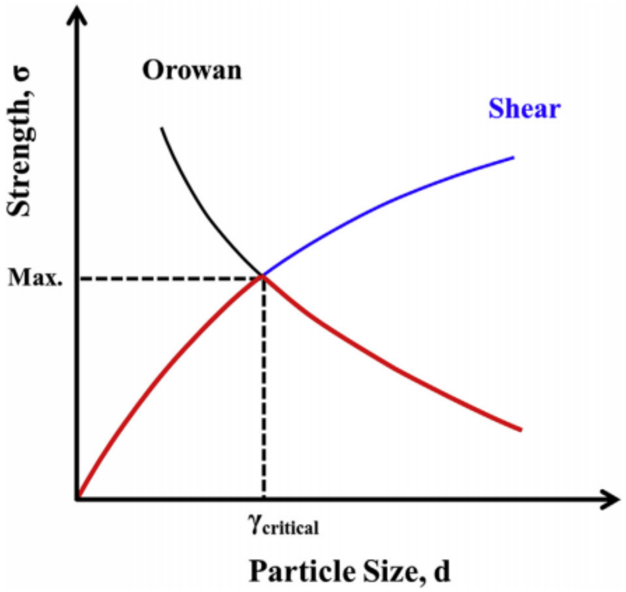

Figure 1.18: Material strength as a function of the particle size with the transition between the mechanism of dislocation shearing and Orowan looping [63]

The word maraging comes from martensite and aging. The maragaing treatment consists in a hardening of heavily strained martensite through the formation of small intermetallic precipitates that act as obstacles against the dislocation motion through the Orowan mechanism [18] leading to a strengthening of the material (Figure 1.18). [65] More specifically, the maraging steels, contrary to most of the other steels, are not hardened by carbon. In such steel, the carbon is considered as an impurity and is kept as low as possible. As a result, they are not relying on carbide precipitation to be hardened but on the precipitation of intermetallic compounds. For instance, the absence of carbon in those steels confers them good properties such as a better formability, a high resistance to thermal fatigue and a combination of strength and thoughness. [65] [66]

Those maraging steels contain several alloying elements like aluminum, titane, but the most present one is nickel. Thanks to the presence of nickel, the martensite is easily obtained. Moreover, the only transformation occurring at ordinary cooling rates will be the martensite transformation. Furthermore, due to the lack of presence of carbon, the martensite formed is quite soft but heavily dislocated. The hardening and strengthening of these steels are performed thanks to further heat treatments (aging). At that moment, the metastable martensite decomposes and leads to the precipitation hardening which occurs faster than the reversion reactions that produce austenite and ferrite. The prevention of the austenite reversion is one of the most important features because the austenite of maraging steels compositions is a stable phase at room temperature. [66]

---

[18] The orowan mechanism corresponds to the bypassing of the dislocations around the precipitates. Depending on the size of the particle, the dislocation will either cut or bypass the precipitate. More specifically, the orowan mechanism will be dominant at higher size of precipitates while the cutting mechanism dominates at lower size. [64]

4.4 The TRIP maraging steels

The TRIP maraging steels will combine two effects, namely the TRIP effect and the maraging effect. As a reminder of the previous sections, the TRIP effect is based on the deformation-stimulated transformation of the metastable austenite into martensite and the plasticity required to accommodate the transformation misfit, and the maraging effect is based on the formation of small intermetallic precipitates that act as obstacles against the dislocation motion through the Orowan mechanism. The combination of such effects leads to excellent properties such as the simultaneous increase of the ductility and strength. [67] [68] [69]

Several studies and researches have been performed on those TRIP maraging steel. Wang et al. [67] have studied the effect of the grain size independently of other effects such as the chemical composition or the surrounding microstructure. Through their investigations they found an unexpected result : "smaller is less stable". They have concluded that this size effect comes from the difference in the evolution of the in-grain deformation in larger (size between $0.3 - 4\mu m^2$) and smaller (size between $0.1 - 3\mu m^2$) retained austenitic grain and more specifically, it comes from the competition between the TWIP[19] and TRIP mechanisms. The mechanical twinning mechanism is activated for large austenitic grains and their in-grain deformation substructures cause a stabilization of the grains and result in a higher mechanical stability. The mechanical twinning mechanism is much less favoured for the small austenitic grains leading to less pronounced substructures from the in-grain deformation. As a result, the smaller grains transform themselves more easily into martensite even at small deformation. Consequently, they proved that the smaller grains present a lower stability against transformation.

Another research performed by Raabe et al. [65] studied the effect of the TRIP maraging steel. More specifically, they studied two TRIP maraging alloys with a different manganese content, respectively, 9wt%, 12wt% and 15wt% Mn. The results showed both an increase in the strength and ductility upon aging. Furthermore, the materials investigated combine three hardening mechanisms:(i) the formation of mechanically induced martensite, such as any TRIP steel hardening mechanism; (ii) the hardening of the ductile low carbon α' and ϵ-martensite phase and of the remaining austenite; (iii) the formation of nanosized precipitates in the deformation-induced and in the as-quenched martensite during the final aging which corresponds to the maraging treatment. Through their investigation they found that the alloy with 12 and 9wt% Mn showed a significant increase in strength and in the total elongation after the aging treatment. They concluded that the surprising increase in the total elongation was coming from the formation of nanoscaled particles that cause an Orowan hardening mechanism and a second strain hardening plateau at intermediate strains.

5 Corrosion

This section is mainly inspired by the book *Corrosion and corrosion control: An introduction to corrosion science and engineering* [71].

Since this study is focusing on the biodegradable stents, a closer look at the corrosion theory seems to be non-negligible. By definition, *the corrosion is the destructive attack of a metal by chemical or electrochemical reaction with its environment.*[71] On the opposite, all deterioration that originates from physical causes are not called corrosion but are referred to as erosion, galling or wear.

---

[19] The TWIP (twinning-induced plasticity steels) steels are austenitic steels which contain above 20% Mn, less than 1% carbon and less than 3% silicon or less than 3% Al. Those steels combine excellent properties at room temperature such as a high strength and ductility. Furthermore, they have a low stacking fault energy (in the order of $20 - 40mJ/m^2$) and their high strain hardening is attributed to the increasing fraction of deformation twins that are considered as strong obstacles to the dislocation glide. [70]

In this section, first a reminder on the basics of the electrochemistry will be exposed since most of the corrosion processes are electrochemical. Then, the accent will be put on the case of iron and its alloys. Finally, a few researches highlighting the corrosion of stents will be reviewed.

5.1 Basics on the electrochemistry

A corrosion process will be composed of two electrodes, one positive called cathode and one negative called anode, and placed in an electrolyte. This combination forms the so-called galvanic cell. More specifically, the cathode corresponds to the electrode where the chemical reduction occurs while it is at the anode that an oxidation reaction occurs.

Furthermore, the galvanic cell converts chemical energy into an electrical energy. For instance, the more the electrical energy flows between the electrode, the more the metal will corrode. This relation between the electrical energy and the corrosion has been expressed by Faraday and it is known as Faraday's Law :

$$WOMR = kIt \tag{1.1}$$

where WOMR expresses the weight of metal reacting in gAs/C; k is the electrochemical equivalent expressed in grammes per Coulomb (g/C), a constant which is equal to $3.39X10^{-4}g/C$ for zinc; I the current expressed in amperes (A); t the time expressed in seconds (s) . If the cell is short-circuiting [20], there will be by convention a positive current that flows from the positive electrode to the negative one, even if,thanks to the researches, it is known that it is the negative charges, the electrons that carry the current. On the other hand, it is both the positive and negative ions that carry the current in the electrolyte. Even if the current carried by each ions depends on their mobility and their electric charge, the total current, positive and negative in the electrolyte is equal to the total current carried by the electrons in the metallic paths.

When the electricity flows, the positive ions, the cations, migrate towards the cathode and the anions, the negative ions, migrate towards the anode. As a result, the current enters the cathode from the electrolyte and leaves the anode to return in the electrolyte.

5.1.1 The types of corrosion

The five main types of corrosion are classified and described below with respect to the outward appearance and the altered physical properties.

5.1.1.1 The general corrosion or the uniform attack

The general corrosion or uniform attack represents a corrosion process that damages the metal uniformly. The rusting of the iron and the tarnishing of the nickel are referred to as general corrosion processes.

The corrosion rates of such processes referred to as the penetration or the weight loss of metal exclude all types of corrosion products on the surface and are expressed in millimeters penetration per year (mm/y) or in grammes per square meter per day (g/m^2d). In the case of these uniform attacks, the corrosion rate tends to be greater at the beginning and then decreases. As a result, the corrosion rates should always be given with the time of exposure, the extrapolation of the corrosion rates is not accurate.

Furthermore, when the attack is defined as uniform, three groups of metals can be highlighted:

- Corrosion rate $<$ 0.15mm/y : Good corrosion resistance
- 0.15 $<$ Corrosion rate $<$ 1.5mm/y : Satisfactory corrosion resistance, suitable for applications in which high corrosion rates are tolerated

---

[20] Short-circuiting a cell consists in attaching a low resistance wire to connect the two electrodes.[71]

- Corrosion rate > 1.5mm/y : Poor corrosion resistance

5.1.1.2 The pitting

On the opposite of the general corrosion, pitting is a localized corrosion process. Hence, greater corrosion rates are found in some areas. There are two main kinds of attacks, namely, the pits and the shallow. Hence, if the attack is a small, fixed area of metal, acting as anode, the resultants will be very deep and called pits. On the other hand, the shallow describes an attacked area larger and less deeper than the pits. The pitting factor, the ratio between the deepest metal penetration and the average metal penetration, is sometimes used to express the depth of the attacked area (Figure 1.19). Consequently, an uniform attack is characterized by a pitting factor equal to one.

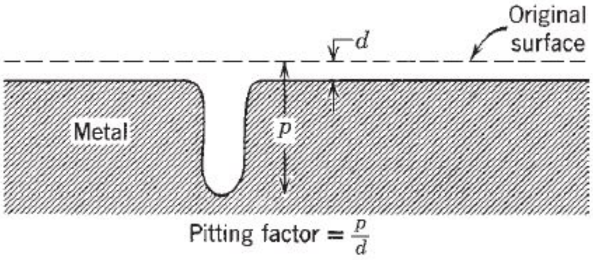

Figure 1.19: Schematic representation of the pitting factor [71]

Other types of corrosion can also create pits on the metals. The fretting corrosion corresponds to the formation of pits at the metal interface due to the relative motion of two substances (at least one of those substances being a metal) in contact. Those pits are often only visible after the removal of the metal debris that have the tendency to fill those pits.

On the other hand, the cavitation-erosion corresponds to the formation of a sequence of pits that can appear as honeycomb of small deep fractures. This cavitation-erosion type of corrosion is due to the loss of material caused by an exposure to cavitation [21] in applications such as rotors in pumps.

5.1.1.3 De-alloying, dezincification and parting

The de-alloying corrosion is characterized by the removal of a particular element from an alloy. For instance, the dezincification is a de-alloying corrosion. The dezincification corresponds to the removal of the zinc element in zinc alloys thanks to a specific solution and leads to the production of porous residue of copper and several corrosion products. This type of corrosion causes a serious decrease of strength and ductility of the material.

Similar to the de-alloying process, the parting corresponds to the removal of one or more components of the alloy. This type of corrosion is mainly for noble metals such as gold. The parting is used in the refinement of gold, for instance. [71]

5.1.1.4 Intergranular corrosion

The intergranular corrosion, a localized attacked corrosion, consists in the attack at the grain boundaries of the metal leading to a loss of strength and ductility. In that type of corrosion, the grain boundary acts as an anode and the larger areas of the grain act as a cathode, the attack is very fast and can lead to serious failures. In particular, when the metal is used at high

---

[21] The cavitation is defined as the formation and collapse of vapor bubbles at a dynamic interface between a metal and a liquid.[71]

temperature and under some specific conditions, some phases with low melting point form and penetrate along the grain boundaries causing this intergranular corrosion. [71]

5.1.1.5 Cracking

Normally, a metal stressed at values below the fatigue limit or the critical stress will not fail by fatigue even after a large number of cycles. But, if the same metal is put in a corrosive environment, it will fail by corrosion fatigue even at low stress. Moreover, there are no true fatigue limits in a corrosive environment.

Furthermore, if a metal cracks after being exposed to a tensile stress in a corrosive environment, it is said that it fails under stress corrosion cracking. The stress may be externally applied or residual in the metal. Moreover, the cracks observed in such corrosion process can be transgranular or intergranular depending on the condition of the stress and the corrosion environment. Nevertheless, the intergranular cracks in the stress corrosion cracking need to be distinguished from the intergranular corrosion where the process proceeds without regard to whether the metal is stressed. [71]

5.1.2 The corrosion's thermodynamics

5.1.2.1 The Gibbs free energy and the electromotive force

As for any chemical reaction, the tendency of a reaction of a metal in its environment to occur is measured by the Gibbs free energy change ΔG. For instance, the more ΔG will be negative the greater will be the tendency of the reaction to happen. As a result, the corrosion rate is not a measure of the tendency to corrode. Hence, a large negative ΔG may or may not be combined with a high corrosion rate, the thermodynamics and kinetics are not specifically related. [71]

In the case of the corrosion process, which is often electrochemical, the Gibbs free energy change can be expressed in terms of the electromotive force (emf) of the corrosion cells. The link between the δG and this force can be expressed as :

$$\delta G = -nFE \tag{1.2}$$

where E is the electromotive force expressed in volts, n the number of electrons taking part in the reactions and F the Faraday constant (F = 96,500 C/eq). The greater the electromotive force the greater the negative δG is, and, hence, the greater tendency the metal will have to corrode.

The electromotive force (emf) can be calculated through the equation 1.4, which is called the Nernst equation. This equation gives the exact eletcromotive force of cell thanks to the activities $(a_Q, a_R, a_L ...)$ of the products and the reactants of the cell. [71]

$$lL + Mm + ... \rightarrow qQ + rR + ... \tag{1.3}$$

$$E = E^\circ - \frac{RT}{nF} \ln \frac{a_Q^q . a_R^r}{a_L^l . a_M^m} \tag{1.4}$$

5.1.2.2 The Pourbaix diagram

The Pourbaix diagram represents graphically the electrochemical and corrosion behavior of any metal thanks to two parameters, namely, the potential and the pH. In those diagrams, the domain where the metal is stable and where it reacts into specific oxides or complex ions can be observed. As an example, in Figure 1.20 the Pourbaix diagram of iron is represented.

Those diagrams are only based on thermodynamics and give no information regarding the kinetics. The information highlighted in those diagrams are the specific conditions of potential

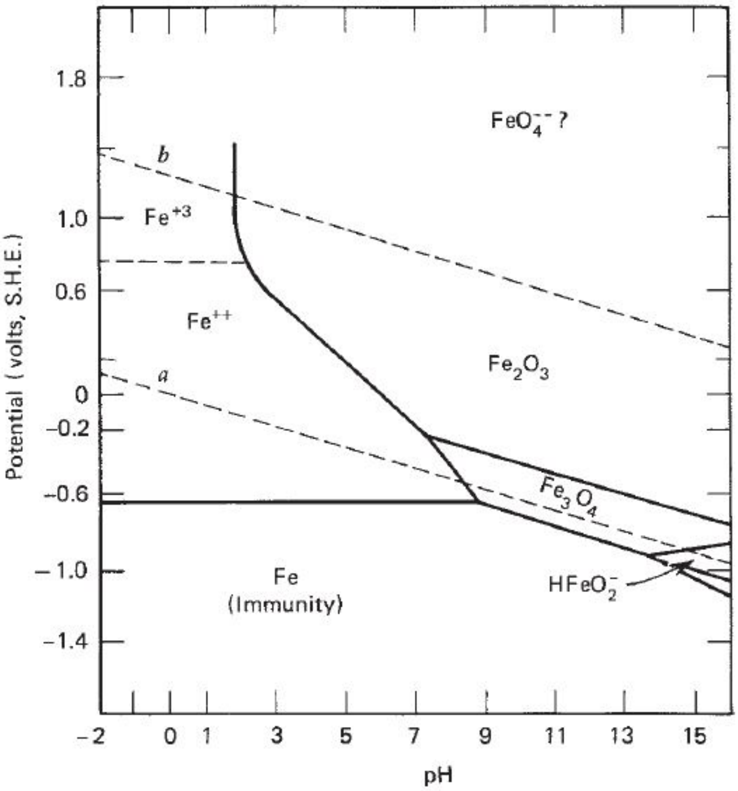

Figure 1.20: Pourbaix diagram of the iron-water system at 25 °C, only the solid substances Fe, Fe_3O_4 and Fe_2O_3 are considered [71]

and pH under which a metal react to form specific oxides or complex ions or does not react. As a result, they indicate the potential-pH domains in which the different species are stable. For instance they do not include information on the alloys or conditions for the non-stoechiometric metal compound films. Hence, the Pourbaix diagrams give useful information on the equilibrium status of a metal either immersed in acids or alkalies or when a specific potential is applied on the metal. [71]

5.1.3 The corrosion's kinetics

In the previous section, the basics of the corrosion's thermodynamics have been reviewed. However, in reality, when studying corrosion processes, it is the kinetic, the rate of corrosion and not the thermodynamics, the equilibrium between the metals and their environment, that is the most relevant. Hence, this approach is based on the non-equilibrium states and on the calculation of the corrosion rates.

Furthermore, the study of the electrode kinetics consists in the study of the reaction rates at the interface between an electrode and a liquid.

Hereafter, the two main concepts of the kinetic are presented, namely, the polarization and the corrosion rate calculation. [71]

5.1.3.1 Polarization

The polarization of an electrode, measured in volts, is characterized by the change caused by the net current to or from an electrode. The polarization depends on several factors such as the nature of the metal and the electrolyte, and also on the electrode area exposed.

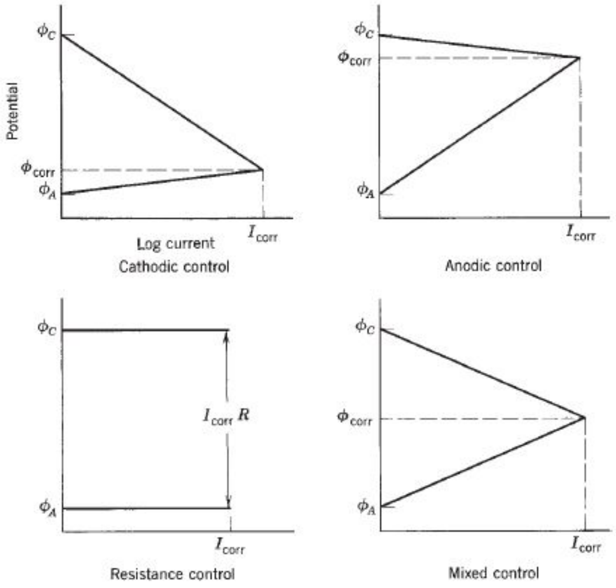

Cathodic control

Anodic control

Resistance control

Mixed control

Figure 1.21: Types of corrosion control [71]

This polarization of the electrodes and the resistance of the electrolyte limit the magnitude of the current produced by a galvanic cell. The reaction can be controlled by several factors. For instance, when the reaction is anodically controlled (Figure 1.21), the polarization mostly occurs at the anodes and the corrosion potential is close to the thermodynamic potential of the cathode. Immersed impure lead in sulfuric acid can be a practical example. In that case, a lead sulfate film covers the anodic areas and it will expose the cathodic impurities such as copper. On the other hand, when the reaction is cathodically controlled (Figure 1.21), the polarization mostly occurs at the cathode and the corrosion potential is close to the thermodynamic potential of the anode. Corroding zinc in sulfuric acid or iron exposed to natural waters can be taken as practical examples.

Furthermore, when the resistance control (Figure 1.21) occurs, the high resistance of the electrolytes causes an insufficient resultant current to appreciably polarize the anodes and cathodes. When there is a mixed control, the polarization takes place in both the anodes and cathodes. [71]

5.1.3.2 Corrosion rates

Several methods exist to calculate the corrosion rates. For instance, the main methods to express the corrosion rate are the weight loss per unit area and unit time, the corrosion current density and the released ion concentration. [72] [73]

When the weight loss is performed, the measures of the weight of the sample before and after the test are needed. The corrosion rate can then be calculated by the equation :

$$CR = \frac{m}{St} \tag{1.5}$$

where CR is the corrosion rate expressed in $g/m^{-2}day$, m the mass loss in grammes, S the exposed surface area in meter square and t is the time in days. [73]

On the other hand, when the the corrosion current density is used, the corrosion current density i_{corr} needs to be measured. The corrosion rate is then calculated thanks to the following formula :

$$V_{corr} = K_1 \frac{i_{corr}}{\rho} EW \qquad CR = K_2 i_{corr} EW \tag{1.6}$$

where v_{corr} expresses the corrosion rate in terms of penetration rate and CR expresses the corrosion rate in terms of the mass loss rate in mm/year, EW is the equivalent weight, I_{corr} is given in $\mu A/cm^2$ K_1 and K_2 are two constant such as $K_1 = 3.27 * 10^{-3} \frac{mmg\mu}{Acmyear}$ and $K_2 = 8.954 * 10^{-3} \frac{gcm^2\mu}{Am^2day}$. [73]

Moreover, when the corrosion rate is calculated from the released ion concentration, the released ion concentration and the volume of immersion solution should be measured. The corrosion rate given in $\frac{g}{m^2day}$ is found according to the formula :

$$CR = \frac{cV}{ST} \tag{1.7}$$

where CR is the corrosion rate, c the released ion concentration in g/ml, V the volume of immersion solution in ml, S the surface area of the specimen m^2 and t is the time in days. [73]

5.2 Iron and steel

In the case of iron and steel in water in a basic medium, the reaction at the anodic areas is [74]:

$$Fe \longrightarrow Fe^{2+} + 2e^- \tag{1.8}$$

and the reaction at the cathodic areas is :

$$O_2 + 2H_2O + 4e^- \longrightarrow 4OH^- \tag{1.9}$$

The reaction 1.9 is often slower than the reaction 1.8. Hence the corrosion process of the iron is often controlled by the cathodic reaction. Nevertheless, the chemical reaction of the iron in water can be written as :

$$2Fe + O_2 + 2H_2O \longrightarrow 2Fe(OH)_2 \tag{1.10}$$

In an aqueous environment, several parameters will affect the behavior of the iron and steel corrosion. In the following subsection, the effect of several factors such as metallurgical factors will be explained. Thereafter, there will be a special focus on the corrosion of the stainless steel and on aluminum and nickel as alloying elements. [71]

5.2.1 The Aqueous environment

Several parameters influence the corrosion in aqueous environments. The main effects will be listed and described below. [71]

5.2.1.1 Effect of dissolved oxygen

In aqueous environment, the presence of dissolved oxygen is necessary to have an appreciable corrosion of iron. Even if the initial rate of corrosion can be high, as the corrosion period evolves, this rate can decrease due to the formation of an iron oxide film acting as a barrier to oxygen diffusion.

On the other hand, at steady state, the diffusion rate is proportional to the oxygen concentration. Hence, the corrosion rate of iron is also proportional to the oxygen concentration.

However, even if at first increasing the oxygen concentration accelerates the corrosion rate of iron, it has been proved that beyond a critical value, the rate drops again to lower values due to the passivation of iron by oxygen. The critical value will depend on different parameters, such that it will increase with dissolved salts and with temperature, and will decrease with an increase of the pH and the velocity. [71]

Furthermore, it has been proved that an increase of the partial pressures of oxygen lead to a larger amount of oxygen that reaches the metal. The excess of oxygen that cannot be reduced by the corrosion reaction can form a passive film onto the metal surface. [71]

5.2.1.2 Effect of the bacteria

The microbiologically influenced corrosion (MCI) corresponds to the corrosion caused by the presence and activities of micro-organisms. This kind of corrosion can lead to different form of localized corrosion: pitting, de-alloying, enhanced galvanic corrosion ... Hence, the MCI can lead corrosion to occur at very high rate at locations where it would not be predicted.

The microbes can form a biofilm onto the metal surface causing the corrosion of the metal. The impact of the corrosion can be intensified by the presence of acidic products of bacterial action trapped between the biofilm-metal surface interface.[71]

Furthermore, it has been proven that the rates of corrosion can be increased by the presence of sulfate reducing bacteria. The proliferation of bacteria can be controlled by a low temperature and humidity and also a good cleaning. Another solution is to perform a chlorination to eliminate the bacteria that cause the corrosion. But, the main drawback of this process is the production of environmentally unacceptable byproducts. [71]

5.2.1.3 Effect of the temperature

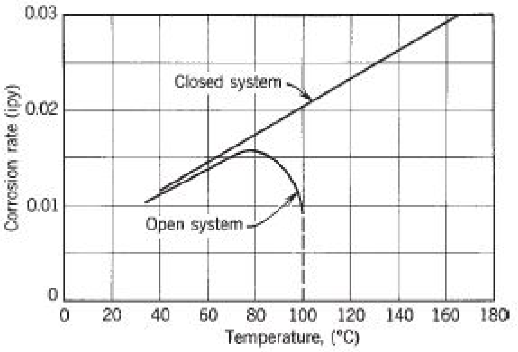

Figure 1.22: Effect of temperature on the corrosion rate of iron containing dissolved oxygen [71]

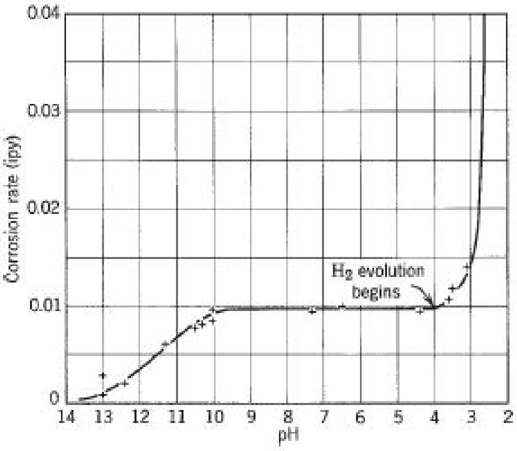

Figure 1.23: Effect of the pH on the corrosion rate of iron in aerated soft water at room temperature [71]

The temperature is an important parameter in a corrosion process. It is well known that if the corrosion is controlled by the diffusion of oxygen, the corrosion rate at a given oxygen concentration more or less doubles for every rise of temperature of $30°C$. [71]

Two main cases can be distinguished: either an open system or a closed system (Figure 1.22). In the case of an open system, the oxygen is able to escape, hence, the corrosion rate increases up to a determined temperature and then falls to very low values. On the contrary, in a closed system, the oxygen is not able to escape, hence, the corrosion rate keeps increasing with the temperature until all the oxygen is consumed. [71]

5.2.1.4 Effect of the pH

The effect of the pH on the corrosion of iron can be seen on Figure 1.23. It can be observed that within the range of pH 4-10, the corrosion becomes independent of the pH and, consequently, will only depend on how rapidly the oxygen diffuses to the metal surface. [71]

Moreover, it has been found that as long as the oxygen diffusion through the oxide layer is controlling, like in a pH between 4-10, only the oxygen concentration, temperature and velocity of the water determine the reaction rate.

Furthermore, this behavior between a pH of 4-10 is important in the stent application, since the pH of the blood is approximately of 7.35 - 7.45. [75]

On the other hand, when the solution is in the acid range, $pH<4$, the oxygen does not control the reaction anymore. The corrosion reaction is controlled, in part, by the rate of hydrogen evolution. Hence, the ferrous oxide film is dissolved and the pH of the surface falls leading to a direct contact between the iron and the aqueous environment.

Specifically, it depends on the hydrogen overpotential of various impurities or phases present in specific steels or irons. For instance, low carbon steel corrodes in acids at lower rate than the high carbon steels since the cementite is a phase of low hydrogen overpotential.[71]

For region above pH 10, there is an increase in alkalinity of the environment that raises the pH of the iron surface. As a result, the corrosion rate decreases because iron becomes passive due to the presence of alkalies and dissolved oxygen. For the very alkaline region, pH 14, the corrosion is again controlled by the hydrogen evolution. [71]

5.2.1.5 Effect of dissolved salts

The presence of sodium chloride has an impact on the oxygen solubility. For instance, the oxygen solubility in water decreases continuously with the sodium chloride concentration. Hence, there will be lower corrosion rates at higher sodium chloride concentration.

In the same way, with the presence of alkali-metal salts (KCl, LiCl, NaBr...) the corrosion rate is affected on the same manner. [71]

5.2.2 Metallurgical factors

Through this subsection, the different metallurgical parameters that affect the corrosion reaction will be detailed. [71]

5.2.2.1 Effect of the composition

In the case of a stainless steel, a high-silicon or a high-nickel iron alloy, the oxygen diffusion no longer controls the rate of the corrosion which causes the decrease of the corrosion process. Other factors, as the chemical composition of the alloys will control the corrosion process.

Carbon has been found to have no effect on the corrosion rate in fresh water but an increase of the rate has been reported in sea water.

Manganese is known to decrease the acid corrosion of steel which contains small amounts of sulfur. Moreover, Mn decreases the solid solubility of sulfur iron.

Furthermore, adding alloying elements can change the passivity of the alloy. More specifically, whereas some elements are able to retain the passive layer, others are able to destroy this layer, often leading to the creation of localized corrosion with pits formation.

5.3 The corrosion of biodegradable implants

Nowadays, the paradigm of the metallic bio-materials consists in the fact that the more the metallic material is resistant to corrosion, the more it is biocompatible. It is known from the previous sections, that the corrosion of the metallic materials depends on different factors including the formation of a passive layer of metal-oxide on the surface of the implant. The goal of the recent researches is to combine a good bio-compatibility with good mechanical and corrosion properties. [76]

Several solutions have already been proposed but the main issue is the very low degradation rate of iron implant. Several solutions have been investigated in order to increase this degradation rate.

Some studies have shown that the addition of manganese can enhance the degradation rate of Fe-Mn alloys. The corrosion products from those alloys consist in metal hydroxides and calcium phosphates, which are bio-compatible products. Furthermore, it has been proved that the austenite phase formed in these Fe-Mn alloys enhances the magnetic resonance imaging compatibility compared to the 316L SS. [76]

On the other hand, pure Fe-foils produced by electroforming have been investigated as biodegradable implants. The studies proved that they show a higher corrosion rate and they have a fine microstructure with small grains and a high volume fraction of grain boundaries.

Moreover, other strategies like the production of microstructural defects and a strong preferred texture that initiate corrosion can also be produced by electroforming. [76]

Furthermore, Liu et al [73] have investigated the effect in vitro of the alloying elements Mn, Co, Al, W, Sn, B, C and S on pure iron. They showed that the elements Mn, Co, W, B, C, and S improve the yield and ultimate strength of iron. On the contrary, Sn led to a drastic reduction of the mechanical properties.

The corrosion results showed that the localized corrosion was the main mode of corrosion for both the pure iron and Fe-X binary alloys. Moreover, same order of magnitude of corrosion rates were found for the pure iron and the Fe-X binary alloys and there was no sign of thrombogenicity with the Fe-X binary alloys.

They concluded that the elements Co, W, C, and S were suitable as alloying elements for iron bio-materials with a suitable combination of mechanical, corrosion and bio-compatibility properties.

Chapter 2

Materials and methods

1 Materials

In this work, a Fe-9Mn-3Ni-1.4Al-0.01C (%wt) TRIP maraging alloy is being studied. This alloy was produced in the form of a pencil ingot thanks to a casting in a Balzers furnace with an alumina melting pot. The melting of the pure metals was performed around $1200 - 1300°C$. The pure elements used were:

- Fe : Armco iron
- Ni : pure nickel (99.9% purity)
- Al : pure aluminium (99.7% purity)
- Mn : pure manganese that has been deoxidised with a solution of 50% HCl

The final pencil ingot had a volume of 30500 mm^3 and a mass of 232.79 g.

The preparation of the sheet of steel was performed thanks to a hot and cold rolling. At first, the hot rolling was performed. The ingot was heated up to $1250°C$ in an furnace for 30 minutes. There was a reduction of 22 tours and the final height was of 3.5 mm. Then, a blasting was performed on the sheet to strip it. Finally, a cold rolling was performed. There was a reduction of 3 tours and the final height was of 0.8 mm.

Table 2.1: Composition of the TRIP-maraging steel determined by ICP

	Al	Fe	Mn	Ni
%wt	1.28	86.7	8.91	2.91

In order to know the exact composition of the sheet, an Inducted Coupled Plasma - Optical Emission Spectrometry (ICP-OES) by the Agilent Technologies 5100 ICP-OES has been done on the final sheet. The results are shown in Table 2.1.

This technique consists in the ionisation of a liquid sample [1] in a plasma of argon by injection of a fine suspension by a nebulizer (Figure 2.1). The fines particles, in the center of the plasma, will undergo a change of state. The electrons of the atoms are then ionized and will emit a photon when they come back to their fundamental state. Specifically, the photons have a characteristic wave length that will be detected by a polychromator. The light emitted by the photon and its intensity is then compared with the one emitted by the same element of a sample of known concentration [2].

---

[1] If the sample is not initially liquid, several chemical attacks are performed on the sample to obtain a liquid.

[2] Courtesy of Ronny Santoro of the IMMC/IMAP institute of the Catholic University of Louvain-la-Neuve.

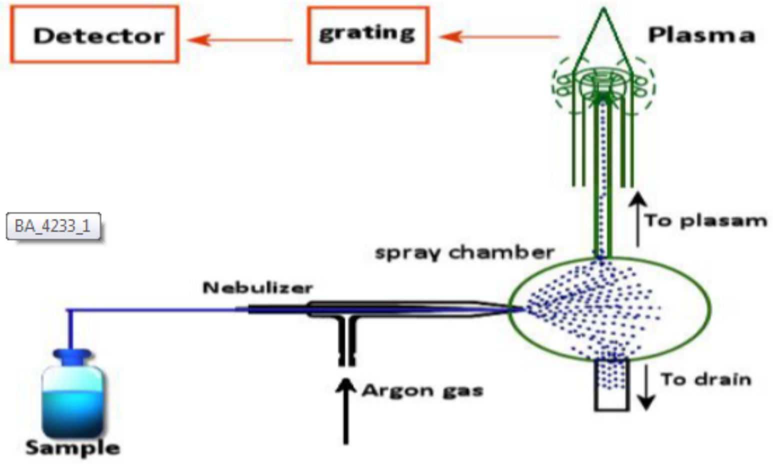

Figure 2.1: Schematic representation of the ICP-OES working principle [77]

Moreover, an analysis of the content of carbon has been performed thanks to an infrared detection combustion found to be equal to 0.03%. This technique consists in a fusion at 1350°C of a sample with a known mass under an oxygen flux. Specifically, carbon and sulfur will be released during the combustion and with oxygen they will form CO_2 and SO_2. The formed CO_2 and SO_2 compounds will be detected by infrared and the weight percentage of carbon and sulfur will be given [3].

2 Experimental procedure and methods

The following experimental procedures and methods are mainly inspired by the work of Wang et al[67] on the same TRIP-maraging steel.

2.1 Modelling: Dictra

Since the TRIP-maraging steel is based on the reversion of the martensite onto austenite thanks to a heat treatment or a mechanical force, the optimal reversion conditions have been calculated numerically. The DICTRA software has been used with the TCFE6 and MOBFE1 databases. The simulation performed was mainly based on the example b1b in the Dictra examples guide [78].

More specifically, because the databases used were not able to treat efficiently all the five elements, simulation has been done only on a maximum of four elements together. Finally, three simulations have been done : Fe-Mn-Ni, Fe-Mn-Ni-Al and Fe-Mn-Ni-C at 600°C for 1h and 8h.

Moreover, the kinetics parameters of the martensite are not present in the databases because it is a non-equilibrium phase. As a result, the martensite was treated as ferrite.

At the beginning, there is a single phase : martensite α. Then there is a reversion of martensite into austenite γ. As a result, an inactive phase of austenite with a planar surface was put as boundary condition. This inactive phase would then be active only when it becomes stable whereas, before, it does not participate to the simulation. This inactive austenite layer is attached to the left side of a martensite phase (ferrite in the simulation) with a $2\mu m$ cell size (Figure 2.2).

---

[3] Courtesy of Ronny Santoro of the IMMC/IMAP institute of the Catholic University of Louvain-la-Neuve.

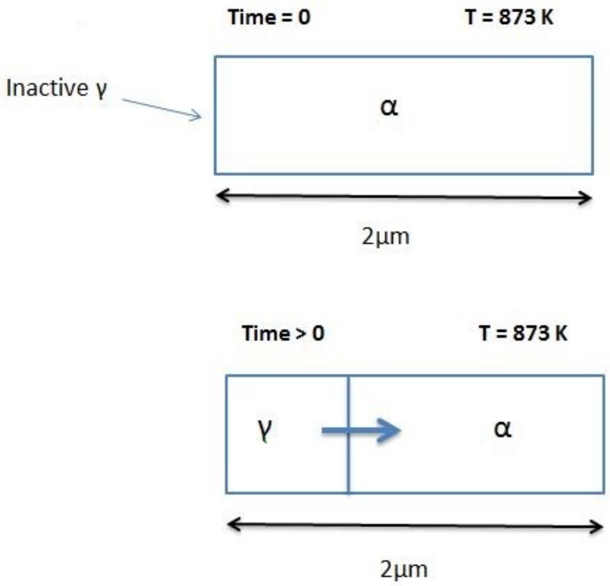

Figure 2.2: Schematic representation of the boundary conditions for the Dictra simulation

2.2 Dilatometry

In order to study the effect of a heat treatment on the microstructure and on the reversion of austenite, several heat treatments have been further investigated thanks to a dilatometer.

The dilatometry is a simple technique that allows the measurement of the dimensions of a specimen as a function of the temperature in a specific atmosphere under a specified controlled temperature program. [79]

The samples used in DIL805A|D TA instruments dilatometer were cut into 10x5 mm little samples by electro-erosion of the sheet produce by the rolling steps. The heating rate was of $10°C/s$.

Table 2.2: Resume of the temperature programs performed with the dilatometry

Temperature program						
Sample	**T1**	**T2**	**T3**	**T4**	**T5**	**T6**
Dilato 1	$1100°C$ for 1h	$25°C$	$600°C$ for 8h	$25°C$		
Dilato 1h/8h	$1100°C$ for 1h	$25°C$	$600°C$ for 8h	$25°C$		
Dilato 1h/1h	$1100°C$ for 1h	$25°C$	$600°C$ for 1h	$25°C$		
Dilato 750	$750°C$ for 1min	$25°C$	$750°C$ for 2sec	$25°C$		
Dilato cycling	$750°C$ for 1min	$25°C$	$750°C$ for 2sec	$25°C$	$600°C$ for 1h	$25°C$
Dilato 900	$900°C$ for 15min	$25°C$	$600°C$ for 1h	$25°C$		
Dilato electropoli	$1100°C$ for 1h	$25°C$	$600°C$ for 8h	$25°C$		
Dilato 1h	$1100°C$ 1h	$25°C$				
Dilato 15/1h	$1100°C$ for 15min	$25°C$	$600°C$ for 1h	$25°C$		

During the test performed in the dilatometer, fused silica was used as support (except for the "Dilato 1" sample, where a Al_2O_3 support was used) and the quench was performed under nitrogen atmosphere. Several temperatures have been investigated. First, the same program of temperature as the work of Wang et al [67] was performed : an homogenization at $1100°C$ for 1h and quenched at room temperature, followed by a further annealing at $600°C$ for 1h or 8h. From those samples, other temperature programs were chosen. More specifically, the investigation of the time and the temperature of the homogenization and annealing but also of the thermal cycling effects were carried out.

Moreover, the characterization of the depth of the sheet has been done through the sample "Dilato electropoli". Furthermore, the first sample did not respect the temperature program imposed due to the Al_2O_3 support used.

The different temperature programs are listed in Table 2.2. Moreover, the cooling performed between each heating consisted in a quench. As a result, all the treatments up to $25°C$ between the heating were performed as a quench under nitrogen. On the other hand, the cooling performed after the annealing at $600°C$ consisted in a natural cooling. Hence, a cooling rate of $5°/s$ was performed. The temperature program performed on the *Dilato cycling* and *Dilato 750* corresponds to a thermal cycling. Hence, it consists in the alternate of fast heating and cooling.[80]

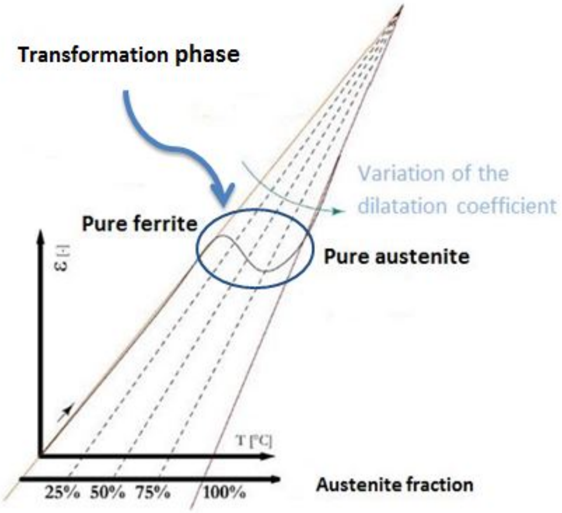

Figure 2.3: Schematic representation of a heating curve obtained with a dilatometry test [81]

The results of dilatometry tests are generally presented on a graph of the extension of the sample versus the temperature. Several information can be extracted from those graphs. More specifically, the fraction of austenite transformed, the M_s and M_f temperature and the thermal expansion coefficients. The phase transformation can be distinguished by a change in the linear behavior of the curve. Specifically, a shape of "S" can be observed when there is a phase transformation (Figure 2.3).

The fraction of austenite transformed can be found thanks to the curve corresponding to the heating phase with a lever rule. For the first heat, there will be a transformation of the ferrite into austenite, then as regards the further annealing, there will be a transformation of martensite into austenite since the cooling stage consists in a quenching. The first heating is represented on the Figure 2.3 : in order to obtain the fraction of austenite a lever rule needs to be performed between the line of the pure ferrite and pure austenite. Specifically, the fraction of austenite will be determined by the ratio $f_a = \frac{AC}{AB}$ for each temperature. Hence, the fraction of ferrite is determined by the ratio $f_f = \frac{CB}{AB}$ or simply by $f_f = 1 - f_a$. The schematic representation of the lever rule is depicted in Figure 2.4.

The dilatation coefficients were found thanks to an equation that links the thermal expansion coefficients with the change of length and the change of temperature:

$$\frac{\Delta L}{L_0} = \alpha_L \Delta T \tag{2.1}$$

They were calculated for the austenite of each of the heating phases and for the ferrite of the

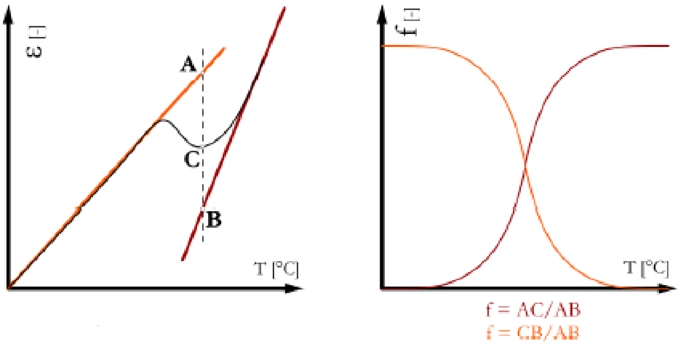

Figure 2.4: Schematic representation of the lever rule on a heating curve of dilatometry [81]

first heating phase. The results were found thanks to Matlab software with an extrapolation of the slopes of the curves of pure ferrite and pure austenite close to the phase transformations in order to ensure a linearity. The schematic representation of a heating curve can be observed on the Figure 2.3. The L_0 taken for the calculations was the L_0 of the beginning of each new heating.

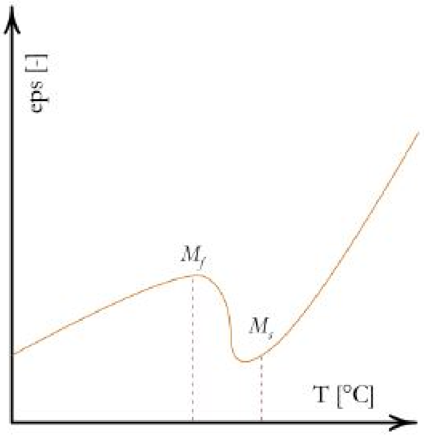

Figure 2.5: Schematic representation of a cooling curve obtain with a dilatometry test [81]

The temperature start and finish of the martensite can be found by looking at the cooling curves (Figure 2.5). More specifically, when the quench is performed, the austenite is transformed into martensite below the martensite start temperature M_s. In other words, for a temperature T, the transformation into martensite begins when $T < M_s$. This transformation is then stopped when the finish martensite temperature M_f is reached such as when $T < M_f$ the transformation is over. Moreover, like the transformation of ferrite into austenite, the transformation of austenite into martensite is characterized by a change in the linear behavior of the curve. Specifically, the M_s and M_f are defined such as in the Figure 2.5. Hence, the M_S and M_f are defined as the temperatures at which the linear behavior of the curve is stopped.

The transformation of martensite into austenite in the further heating stages are analysed and characterized the exact same way as the transformation of the ferrite into austenite.

2.3 Heat treatments

In order to calibrate the fraction of austenite and to compare it with the dilatometry samples, several heat treatments have been performed with different furnaces. Four square samples of 1cm length have been cut in the sheet with a simple shear. All the samples were then heated up to 1100°C for 1h in a Carbolite furnace RHF 14/9 and quenched in water. Then, the samples were further annealed at 600°C in a Nabertherm furnace L9 for 1h, 8h, 24h and 48h respectively. Finally, the samples were then removed from the furnaces and cooled naturally.

The different heat treatments are gathered in Table 2.3.

Table 2.3: Heat treatments performed in the furnaces

Samples	**T1**	**quenching**	**T3**
furnace 1h	1100°C 1h	quenched in water	600°C 1h
furnace 8h	1100°C 1h	quenched in water	600°C 8h
furnace 24h	1100°C 1h	quenched in water	600°C 24h
furnace 48h	1100°C 1h	quenched in water	600°C 48h

2.4 Polishing stage

In order to further analyze the sample from the dilatometer and the furnaces, a polishing stage was non-negligible. First, the samples have been embedded in a conductive resin, Polyfast. Then, all the samples have been polished.

First, a mechanical polishing has been applied thanks to a pre-polishing step with silicon carbide paper (SiC) and a polishing step with a diamond paste ($1\mu m$ polishing finish). Then a chemical polishing with a non-drying colloidal silica suspension (OP-S Non Dry) was performed to remove the strain-hardened layer created during the mechanical polishing. All the steps of the polishing are summarised in Table 2.4.

Table 2.4: Polishing steps of the dilatometry and furnace samples

Polishing step	**shutoff parameter**
SiC paper 320	uniform surface with all lines parallel
SiC paper 500	uniform surface with all lines parallel
SiC paper 800	uniform surface with all lines parallel
SiC paper 1200	uniform surface with all lines parallel
SiC paper 4000	uniform surface with all lines parallel
Diamond paste polishing $1\mu m$	15 minutes
OP-S Non Dry	5 minutes

2.5 Immersion tests

Two distinct tests of immersion have been performed. First, three square samples of 1cm length have been cut thanks to a slitting shears. The three samples have been submitted to three different heat treatments. All the samples were first heated up to 1100°C for 1h in the Carbolite furnace and quenched in water, then, the samples were further annealed at 600°C for 0h, 8h and 24h respectively in the Nabertherm furnace. After, the samples were taken out of the furnace and cooled naturally. The heat treatments are gathered in Table 2.5. Then, a small hole near the edge of the sample was created thanks to a drill bit of 1mm diameter such as in Figure 2.6. After the hole was created all the faces of the square have been polished up to the 1200 SiC paper. After the polishing steps, all the samples were measured and weighed.

This first immersion test was performed for seven days in a heat chamber Binder C 150 with a physiological pH (7.3- 7.7) regulation by CO_2 (5%) at 37°C. The samples have been immersed in 50mL of a simulated body fluid solution (SBF) [4]. The exact composition of this simulated

---

[4] In order to have a final pH corresponding to a physiological pH, a small amount of HCl 6M has been added to the solution before immersing both samples during the first and the second immersion.

Table 2.5: Heat treatments and time of the immersion tests performed

First immersion test				
Samples	**Treatment 1**	**Treatment 2**	**Treatment 3**	**Immersion time**
Immersion 0h/Week	1100°C 1h	quenched in water	600°C 0h	7 days
Immersion 8h/week	1100°C 1h	quenched in water	600°C 8h	7 days
Immersion 24h/week	1100°C 1h	quenched in water	600°C 24h	7 days
Second immersion test				
Samples	**T1**	**T2**	**T3**	**Immersion time**
Immersion 0h/1h	1100°C 1h	quenched in water	600°C 0h	1h
Immersion 0h/day	1100°C 1h	quenched in water	600°C 0h	1 day
Immersion 8h/1h	1100°C 1h	quenched in water	600°C 8h	1h
Immersion 8h/day	1100°C 1h	quenched in water	600°C 8h	1day
Immersion 24h/day	1100°C 1h	quenched in water	600°C 24h	1 day

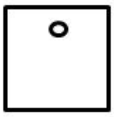

Figure 2.6: Schematic representation of the immersion sample

body fluid solution is given in Table 2.6. More specifically, the polished samples have been hung with a nylon string, washed in ethanol, in the solution (Figure 2.7). Moreover, the immersion tests performed were static.

Table 2.6: Composition of the simulated body fluid solution used for all the immersion tests [82]

Compounds	**g/l ultrapure water**
Mg chloride hexahydrate	0.2033
Na chloride	6.0193
K chloride	0.2982
dibasic Na phosphate	0.1420
Na sulfate	0.0710
Ca chloride dihydrate	0.3676
Na acetate trihydrate	0.9526
Na bicarbonate	2.6043
Na citrate dihydrate	0.0970

In order to see the influence of the first hours of the immersion and the influence of the immersion on the micro-structure of the sample, a second immersion test has been carried out. As for the first test, five square samples of 1cm length have been cut with a slitting shears and they were then submitted to different heat treatments. The five samples were first heated to 1100°C for 1h in the Carbolite furnace and then further annealed at 600°C for 0h, 0h, 8h, 8h and 24h hours respectively in the Nabertherm furnace. After, the samples were taken out of the furnace and cooled naturally. The different heat treatments are gathered in Table 2.5. A hole was also drilled with the same drill bit as for the first test in all the five samples before the polishing of the samples.

All the samples were then polished up to the 1200 SiC paper on one side and up to OP-s

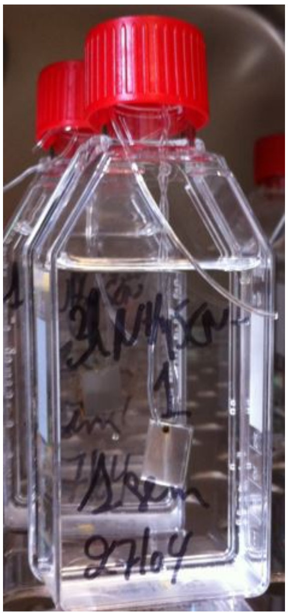

Figure 2.7: Setup of the immersion tests

polishing on the other side. More specifically, one side of the square has followed the same polishing steps as the first immersion test and the other side has followed the polishing steps gathered in Table 2.4. After the polishing steps, all the samples were measured and weighed.

The second immersion test has been performed in two steps. First, the two samples *Immersion 0h/1h* and *Immersion 8h/1H* were immersed in 50mL of a SBF solution (see Table 2.6 for the exact composition) for 1 hour. Second, the three samples *Immersion 0h/day*, *Immersion 8h/day* and *Immersion 24h/day* were also immersed in 50mL of a SBF solution for 1 day. The setup of these tests were the same as for the first immersion test. Specifically, the samples were placed in a heat chamber Binder CB 160 with a physiological pH (7.3-7.5) controlled by CO_2 (5%) at $37°C$. As well as for the first test, the immersion was static.

For all the immersion tests, the pH and the temperature of the solution were measured before and after the test. After the immersion, all the samples were cleaned with distilled water and ethanol and they were then dried. The remaining solution was then further analyzed by ICP and the corrosion rates were calculated thanks to the ion released concentration. More specifically, the corrosion rates can be calculated from the concentration of the elements in the solution measured thanks to the ICP. The equation that links the corrosion rate expressed in $gm^{-2}day^{-1}$ with the ion concentration released is as follows:

$$CR = \frac{cV}{ST} \tag{2.2}$$

where CR is the corrosion rate, c the released ion concentration in g/ml, V the volume of immersion solution in ml, S the surface area of the specimen m^2 and t is the time in days. [73] This equation was already stated in Chapter 1.

2.6 Microstructural characterization and composition analysis : Scanning electron microscope (SEM) and Energy dispersive X-ray spectroscopy (EDX)

The microstructure of the surface of different samples have been analyzed by the scanning electron microscope ULTRA-55 from Zeiss with a field emission electron beam source (FESEM).

A scanning electron microscope uses a focused-beam of high-energy electrons. Specifically, the SEM uses accelerated electrons carrying a significant amount of kinetic energy that is dissipated in a variety of signals. Those signals are produced by the electron-sample interactions coming from the incident electrons decelerated in the solid sample. Several signals can be distinguished : the secondary electrons, the backscattered electrons, the diffracted backscattered electrons, the photons (X-rays), the visible light and the heat. Thanks to those signals, different information can be revealed : the external morphology (texture), the chemical composition and the crystalline structure.

The backsctattered and the secondary electrons are mainly used for imaging samples. More specifically, the secondary electrons are of a great interest to show the morphology and the topography of the samples. On the other hand, the backscattered electrons are of a great interest to illustrate the contrast in composition in multiphase samples.

Furthermore, whereas the diffracted backscattered electrons are generally used to determine the crystal structures, the photons are used to perform elemental analysis. [83]

More specifically, when the primary electrons stop in the specimen they form a volume below the specimen surface called the interaction volume. The depth and the shape of this volume depend on the accelerating voltage and on the average atomic number of the sample. Hence, gathering information about the very thin layer below the surface material is possible with electrons very close to the specimen surface, the secondary electrons. On the other hand, in the case of the backscattered electrons, which have a very high energy compared to the secondary one, a deeper analysis of the specimen is possible.

The peer of interaction that gathers the different interaction volume depending on the signals type is showed in Figure 2.8. [84]

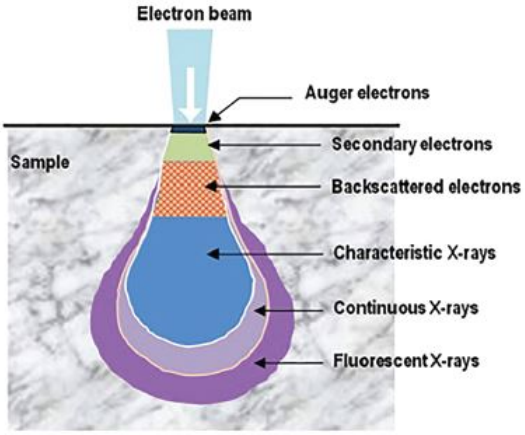

Figure 2.8: Peer of interaction [84]

Furthermore, the composition of the samples surfaces have been investigated thanks to an energy dispersive X-Ray analysis (EDX) with a Quantax Brucker detector as X-ray detector.

An energy dispersive X-Ray analysis is a technique that uses X-rays to identify the elemental composition of materials. These EDX techniques are generally combined with electron microscopy, and more specifically here, with the scanning electron microscope. The data generated by this technique are presented as a spectra showing peaks corresponding to the elements constituting the true composition of the sample. [85]

2.6.1 Dilatometry samples and Furnace samples

After the samples have been embedded within a conductive resin, Polyfast and polished up to the OP-S step the samples were then further analyzed with the scanning electron microscope. Specifically, the samples were observed with the SEM thanks to the secondary and the backscattered electrons with a voltage of 15 kV.

2.6.2 Immersion samples

The preparation of the immersion samples have been previously stated in the previous section. The immersion samples have then been further investigated with the SEM and the EDX. Thanks to the secondary electrons in the SEM, the samples surface after immersion were analyzed and with the help of the EDX technique the composition of the surface products were investigated.

2.6.3 The metastable properties of the austenite

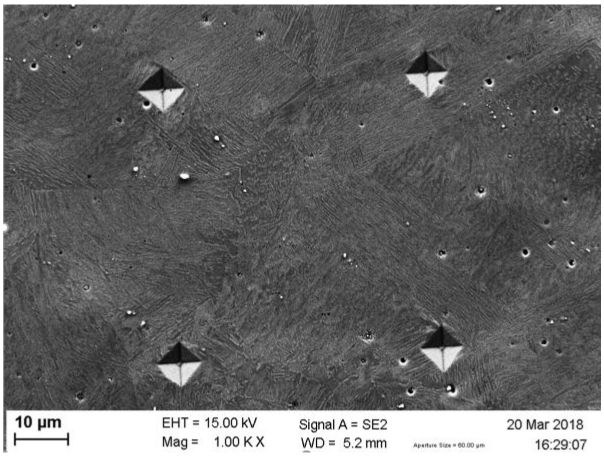

Figure 2.9: SEM image in secondary electron of the square delimited by the indents on the surface of the sample *Dilato electropoli*

In order to investigate the metastable properties of the austenite and the impact of a mechanical polishing on this TRIP-maraging steel, the sample *Dilato electropoli* has been electropolished for 2 minutes with a voltage of 20 volts. Then, a square of 50 microns delimited by four indents of approximately 10 microns have been created on the sample. The SEM image of the square can be observed in Figure 2.9.

The square and its neighbouring composition were then further analysed by EDX.

2.7 Analysis of the austenite phase fraction by X-Ray diffraction (XRD)

The phase volume fraction of the austenite was investigated thanks to a X-Ray diffraction technique. The Bruker D8 was used with a cobalt source. The voltage was of 30kV and the current of 30 mA. Moreover, the time step was of 10 seconds and the step size of 0.02° [5].

The X-Ray diffraction technique gives information on the structure, the phases, the texture and on different others structural parameters such as the crystallinity. The results are presented as peaks of diffraction and they are produced by the constructive interference of a monochromatic beam of X-ray diffused at specific angles of a sample. The peak's intensity are determined by the distribution of the atoms in the sample. Hence, the diffraction peaks are the unique imprint of the atoms in a sample. [87]

---

[5] The step size is defined as the intervals of 2-theta where the experimental data will be acquired. Moreover, the time step, which depends on the step size, is the time per step.[86]

2.7.1 Dilatometry samples

In order to observe the influence of the heat treatments performed with the dilatometer on the phase volume fraction of austenite, X-Ray diffraction has been performed on several dilatometry samples. The embedded and polished samples were then analyzed with the XRD technique. Specifically, the samples analyzed with the X-Ray diffraction are the *Dilato 1h/8h*, *Dilato 1h/1h*, *Dilato 750*, *Dilato cycling*, *Dilato 900* and *Dilato 15/1h.*

2.7.2 Furnace samples

As well as for the dilatometry samples, the influence of the austenite phase volume fraction and the heat treatment have been investigated on the samples treated in the furnaces. Again, the same polished and embedded in the Polyfast resin samples as the one investigated with the scanning electron microscope have been analyzed with the XRD technique. Specifically, the samples *Furnace 1h*, *Furnace 8h*, *Furnace 24h* and *Furnace 48h* have been investigated.

2.7.3 Analysis of the diffraction peaks

In order to investigate the austenite phase fraction in the different samples from the results of the X-Ray diffraction tests, two methods have been used. First, the quantitative analysis; secondly, the Rietveld method with the Topas software.

The quantitative analysis is based on the observation that the intensity of the diffraction pattern of a specific phase in a mixture of phases depends on the concentration of that specific phase in the mixture. Moreover, the diffracted intensity depends on the absorption coefficient of the mixture which depends itself on the concentration. Hence the relation between the concentration and the intensity is generally non linear. Specifically, the link between the intensity and the concentration of one phase α can be written as :

$$I_\alpha = \frac{K_1 f_\alpha}{\mu_m} \tag{2.3}$$

where the K_1 is a constant, I_α the intensity, f_α the volume phase fraction of the phase α and μ_m the linear absorption coefficient. The constant K_1 can be written as : $K_1 = KR_1$ where K depends on the experimental parameters and R_1 depends on the Bragg's angles and the Miller's indices :

$$K = \left(\frac{I_0 A \lambda^3}{32\pi}\right)\left(\left(\frac{\mu_0}{4\pi}\right)^2 \frac{e^4}{m^2}\right) \tag{2.4}$$

$$R_1 = \left(\frac{1}{v^2}\right)\left(|F|^2 p \left(\frac{1 + cos^2 2\theta}{sin^2\theta cos\theta}\right)\right)(e^{-2M}) \tag{2.5}$$

Finally, the equation 2.3 can be written as :

$$I_\alpha = \frac{K R_\alpha f_\alpha}{2\mu_m} \tag{2.6}$$

Since in the alloy study two main phases are present, namely the austenite (γ phase) and the ferrite (α phase), a mixture of those two phases is present in the X-Ray diffraction results. Hence the intensity of those two phases can be divided such as :

$$\frac{I_\gamma}{I_\alpha} = \frac{R_\gamma f_\gamma}{R_\alpha f_\alpha} \tag{2.7}$$

When the ratio $\frac{f_\gamma}{f_\alpha}$ is then known, with a last equation stated as : $f_\gamma + f_\alpha = 1$, the value of each volume phase fraction can be easily obtained.

In this work, the integrated intensity of the peaks have been calculated thanks to the function "trapz" in Matlab and the values of the R coefficients are gathered in Table 2.7. [88]

Table 2.7: Values of the coefficients R_α, R_γ in relation with the corresponding Miller indices for a cobalt source. Courtesy of the CRM group [89]

hkl	R_α	R_γ
110	118	-
111	-	87
200	16	38
211	35	-
220	18	21
311	-	33

The Rietveld method is a numerical method which tries to minimize the difference between an experimental pattern and a model based on different parameters. In order to have a better fitting, several crystallographic constrains are imposed. Whereas the lattice parameters and the space group will constrain the peak position, the crystal structure will constrain the peak intensities. The software used to apply this numerical method was Topas. [90] [91]

2.8 The traction tests

Table 2.8: Heat treatments performed on the traction specimens

Samples	**Treatment 1**	**Treatment 2**	**Treatment 3**
Specimen 0h	1100°C 1h	quenched in water	600°C 0h
Specimen 8h	1100°C 1h	quenched in water	600°C 8h
Specimen 24h	1100°C 1h	quenched in water	600°C 24h
Specimen 48h	1100°C 1h	quenched in water	600°C 48h

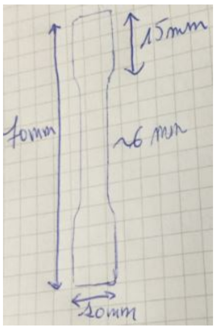

Figure 2.10: Schematic representation of the dimension of the specimens

In order to characterize the mechanical properties of the TRIP-maraging steel study, traction tests have been performed. Four traction specimens have been machined by electro-erosion. The specimens have been machined such as in Figure 2.10. In order to reveal the influence of the heat treatments and the volume fraction of the austenite, different heat treatments have been performed on the four specimens. All heat treatments performed are summarised in Table 2.8. The treatments performed at 1100°C have been done in a Carbolite furnace and the treatments at 600°C have been performed in a Nabertherm furnace.

Figure 2.11: State of the surface of the *Specimen 0h*, the *Specimen 8h* and the *Specimen 24h* (from right to left)

Figure 2.12: State of the surface of the *Specimen 48h*

Before the traction tests, all four specimens were polished with a 1200 SiC paper in order to remove the oxyde layer formed during the heat treatments. The state of the four specimens are presented in Figure 2.11.

The traction tests have been performed with a Zwick-Roell machine that has a maximum charge of 50kN. There was no pre-charge and Instron load frames were used. The speed of deformation was fixed at 0.5mm/min up to the fracture of the specimen and the displacement was measured thanks to an extensometer placed on the specimens.

Chapter 3

Results

This chapter will summarise the results obtained from the experiments. First, the results of the simulations performed with the Dictra software will be exposed. Second, the graphs resulting from the dilatometry tests and their characteristics including their thermal expansion coefficients, martensite transformation and their resulting microstructures will be highlighted. Third, the quantification of the austenite fraction of each sample thanks to the XRD analysis will be summarised. Fourth, the EDX analysis on the metastable austenite will be presented. Thereafter, the results of the tensile tests will be exposed. Finally, the corrosion rates and the microstructure of the samples of the immersion tests will be given.

1 Modelling: Dictra

In this section, the results of the modelling of the optimal reversion conditions of martensite into austenite with the Dictra software will be presented.

The graphs present the predicted reversion of martensite α' into austenite γ in the different elements composing the TRIP-maraging steel at a temperature of $600°C$ for 1 hour and 8 hours. Three curves can be distinguished in each graph representing the three simulations performed. The interface between the austenitic and the martensitic phase is represented on each graph by the long vertical line. Hence, the austenite phase is on the left whereas the martensite phase is on the right of the interface.

Furthermore, the constant value reached at the end of the simulations in the martensitic phase is the same as the one of the volume fraction of the corresponding element at the beginning of the simulation, hence the one at 0 hour. On the other hand, the first plateau corresponds to the value of the volume fraction of the element in the austenite phase. In addition, the variation between those two plateaus corresponds to the redistribution of the elements in the two phases.

First, the evolution of the weight fraction of manganese is presented in Figures 3.1 and 3.2 for 1 hour and 8 hours respectively. Since the manganese is a gammagenic element, a higher content of manganese in the austenitic phase compared to the martensitic phase can be observed in all simulations. Moreover, the simulation Fe Mn Ni C is, for both 1 hour and 8 hours, the one with the largest cell size of austenite. On the other hand, the Fe Mn Ni Al has always the shortest austenitic plateau.

By comparing the two graphs, it can be noticed that the curves behave more or less the same way but, for 8 hours, there is a longer austenitic plateau. Hence, the cell size of austenite is larger. Furthermore, the weight fraction of manganese in the martensite phase is about 9.2% for both 1 and 8 hours simulation.

Second, the evolution of the weight fraction of nickel is presented on Figures 3.3 and 3.4 for 1 hour and 8 hours respectively. As well as for manganese, the nickel is a gammagenic element.

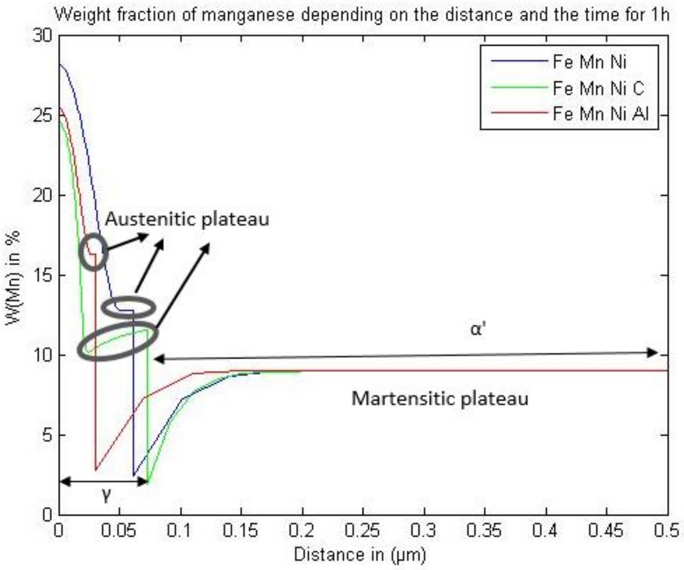

Figure 3.1: Predicted reversion of martensite α' into austenite γ at 600°C for 1 hour of the elemental partition of the manganese simulated by Dictra

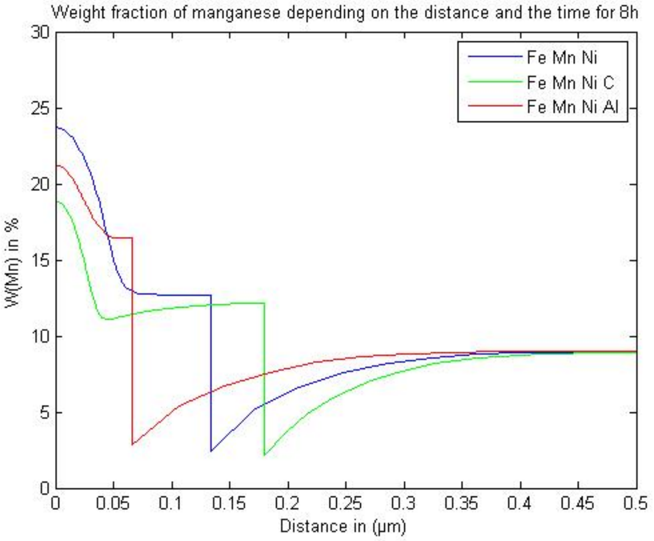

Figure 3.2: Predicted reversion of martensite α' into austenite γ at 600°C for 8 hours of the elemental partition of the manganese simulated by Dictra

Hence, a higher content of nickel in the austenitic phase compared to the one in the martensitic phase can be observed for all simulations. By comparing the graphs of nickel and manganese at first, a larger decrease of nickel in the austenitic phase can be noticed before reaching its constant value. Again, the Fe Mn Ni C simulation is the first one to stabilise into an austenitic phase and it has as well the longest austenitic plateau.

Moreover, the 8 hours simulation curves present again longer austenitic plateau at the same weight fraction as the one of the 1 hour simulation. Furthermore, the 1 and 8 hours simulation stabilise themselves around a weight fraction of nickel of 3% in the martensite phase.

Third, the weight fraction of aluminum is presented in Figure 3.5 for 0 second, 1 hour and 8 hours. Contrary to manganese and nickel, aluminum is an alphagenic element. Hence, the content of aluminum first increases in the austenitic phase but it reaches a lowest value in the

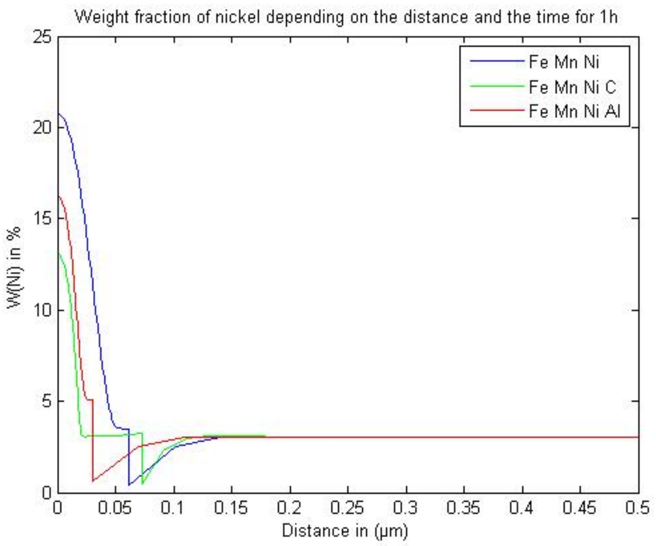

Figure 3.3: Predicted reversion of martensite α' into austenite γ in the TRIP-maragaging steel at $600°C$ for 1 hour for the corresponding elemental partition of Nickel simulated by Dictra

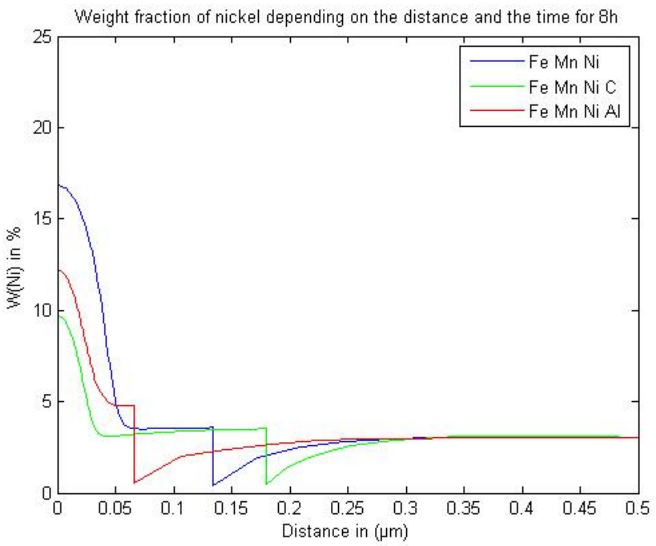

Figure 3.4: Predicted reversion of martensite α' into austenite γ in the TRIP-maragaging steel at $600°C$ for 8 hours for the corresponding elemental partition of nickel simulated by Dictra

austenitic than in the martensitic phase. Afterwards, it reaches again its initial weight fraction of 1.4% in the martensitic phase.

Again, by comparing the 1 hour and 8 hours simulations it can be noticed that the plateau of austenite is longer for 8 hours.

Fourth, the weight fraction of carbon is presented in Figures 3.6 for 0 second, 1 hour and 8 hours. Contrary to aluminum, carbon follows a decrease in its content in the austenitic phase before reaching a constant value higher than the one in the martensitic phase. Hence, as for nickel and manganese, carbon is a gammagenic element.

As for the other elements, the 8 hours simulation gives a longer austenitic plateau than the 1 hour. Furthermore, the decrease in the weight fraction of carbon before reaching the austenitic plateau is much smaller than for the other elements. Moreover, the stabilisation of the weight fraction of carbon in the martensite phase is lower than the initial fraction: 0,01% for 1 and 8

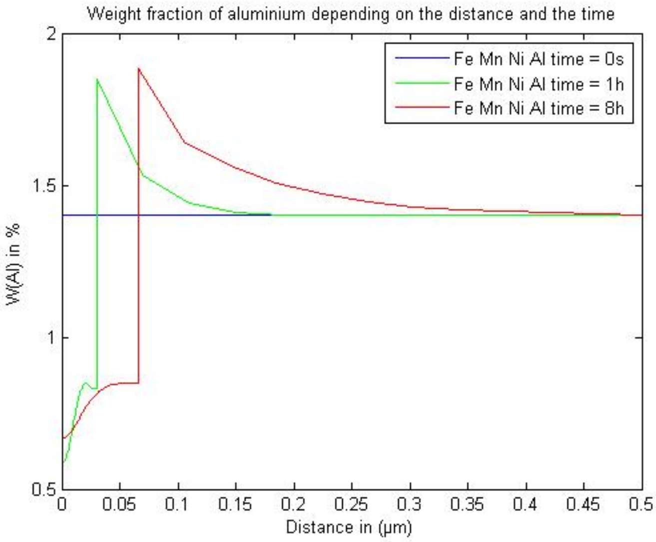

Figure 3.5: Predicted reversion of martensite α' into austenite γ in the TRIP-maragaging steel at 600°C for 0 second, 1 hour and 8 hours for the corresponding elemental partition of aluminum simulated by Dictra

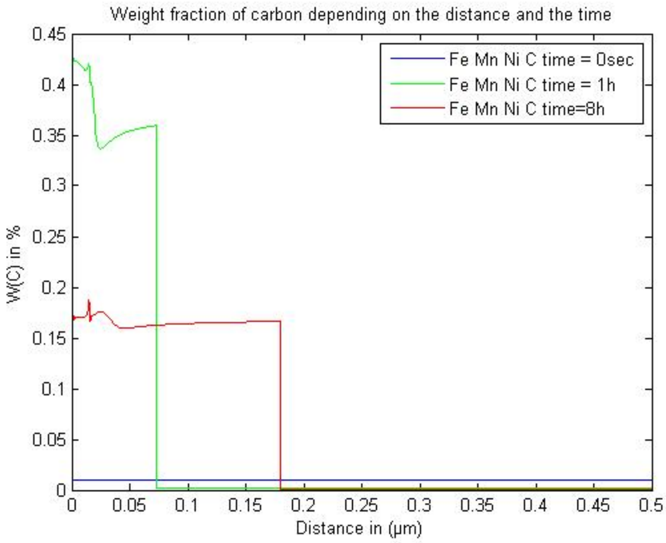

Figure 3.6: Predicted reversion of martensite α' into austenite γ in the TRIP-maragaging steel at 600°C for 0 second, 1 hour and 8 hours for the corresponding elemental partition of carbon simulated by Dictra

hours and 0,02% for 0 seconds.

Fifth, the weight fraction of iron is presented in Figures 3.7 and 3.8 for 1 and 8 hours. As well as for aluminum, the weight fraction of iron first increases in the austenitic phase before it reaches a constant value lower than the weight fraction in the martensitic phase. On the contrary, for the other elements their weight fraction in the austenitic phase is higher than their initial weight fraction in the martensitic phase. Moreover, the Fe Mn Ni C is still the simulation that presents the largest austenitic plateau for both 1 and 8 hours. On the other hand, the Fe Mn Ni Al simulation has still the smallest austenitic plateau.

Furthermore, the three simulations for both 1 and 8 hours do not stabilise at the same iron weight fraction as their initial one in the martensite phase. The simulation Fe Mn Ni C and Fe

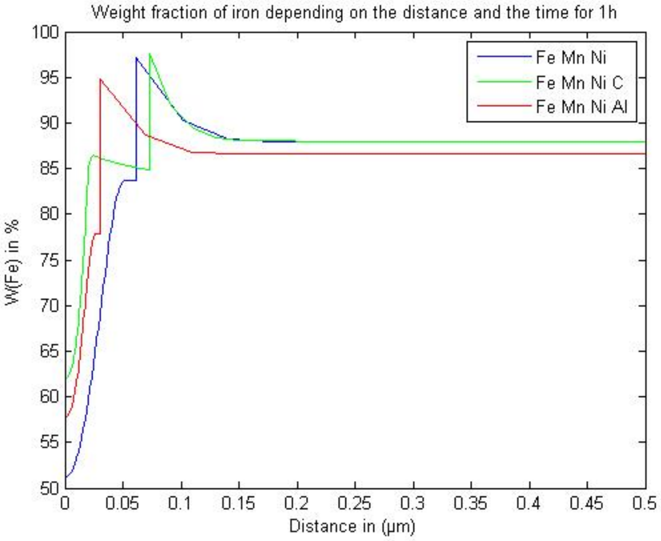

Figure 3.7: Predicted reversion of martensite α' into austenite γ in the TRIP-maragaging steel at 600°C for 1 hour for the corresponding elemental partition of iron simulated by Dictra

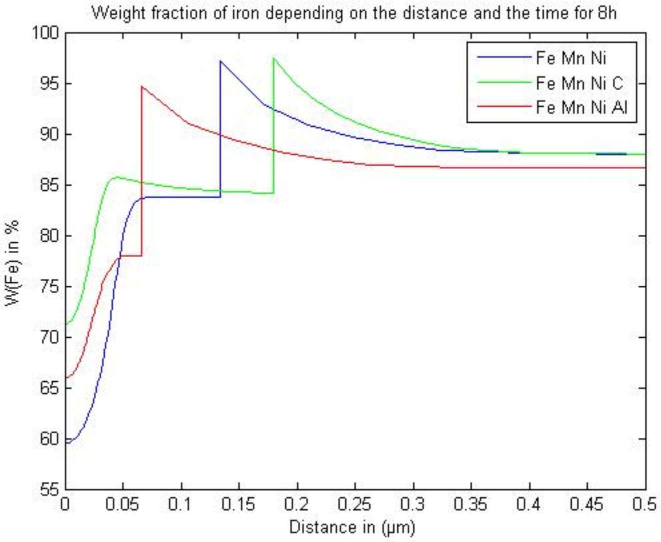

Figure 3.8: Predicted reversion of martensite α' into austenite γ in the TRIP-maragaging steel at 600°C for 8 hours and the corresponding elemental partition of iron simulated by Dictra

Mn Ni stabilise around 88% whereas the simulation Fe Mn Ni Al stabilise around 86%.

Finally, in the austenitic phase all elements except iron and aluminum reach a higher weight fraction than the one of the corresponding element in the martensitic phase. Indeed, the gammagenic elements stabilise the austenite whereas the alphagenic elements stabilise the ferrite[1]. The simulation Fe Mn Ni C seems to be the one that leads to the longest austenitic plateau. Hence, the Fe Mn Ni C simulations leads to the largest cell size of reverted austenite. On the other hand, the Fe Mn Ni Al seems to be the one that leads to the smallest austenitic plateau. Moreover, the 8 hours simulation tends to cause a lengthening of the austenitic plateau.

---

[1] Reminder: the martensite phase is treated in the simulations as a ferrite phase.

2 Heat treatments

In this section the results of the different heat treatments will be presented. First, the results of the dilatometry tests will be exposed. Thereafter, the results of the furnaces tests will be shown.

2.1 Dilatometry

Through this section, the different dilatometry results will be presented. First, the resulting graphs of the elongation of the sample versus the temperature of each dilatometry test will be highlighted. Second, the thermal expansion coefficients of the austenitic and ferritic phases, the M_S and M_f temperatures will be given. Then, the graphs of the elongation of the sample versus the time will be detailed. Finally, the microstructure obtained thanks to the different heat treatments performed will be analysed.

2.1.1 Variation of the elongation of the samples with the temperature

In all the resulting graphs, it can be highlighted that there is an expansion during the heating and a contraction during the cooling as well as during the plateau. Moreover, the several phase transformations that occur during the heating program can be distinguished by their "S" shape.

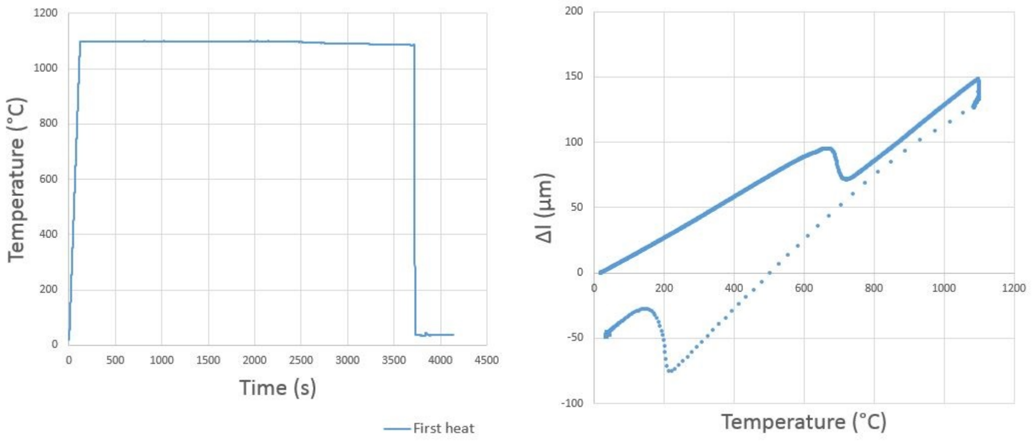

Figure 3.9: Temperature profile of the heat program (Left) and elongation of the sample ΔL versus the temperature for sample *Dilato 1h* (Right)

First, the graph resulting from the sample *Dilato 1h* is shown on Figure 3.9. Compared to the other samples, it has only been treated with one plateau at 1100$°C$ for 1h. Hence, this graph corresponds to the first part of the graphs on Figures 3.13, 3.10 and 3.11. In addition, two phase transformation can be highlighted. Furthermore, a little bump can be distinguished before the first phase transformation.

Second, the graph resulting from the sample *Dilato 1h/1h* can be observed in Figure 3.10. This sample can be compared with the *Dilato 1h/8h* sample. It can be noticed that even if they present more or less the same behaviour, some differences can be explained. Even if the first phase transformation appears in the same range of temperatures, the second one appears at lower temperatures and seems to happen on a shorter range of temperatures. In addition, a smaller contraction can be observed for the plateau of 1 hour compared to the one of 8 hours in the sample *Dilato 1h/8h*.

Furthermore, on the temperature profile of the sample *Dilato 1h/1h*, a small peak around 4000 seconds can be highlighted. This peak translates the recalescence phenomenon. This

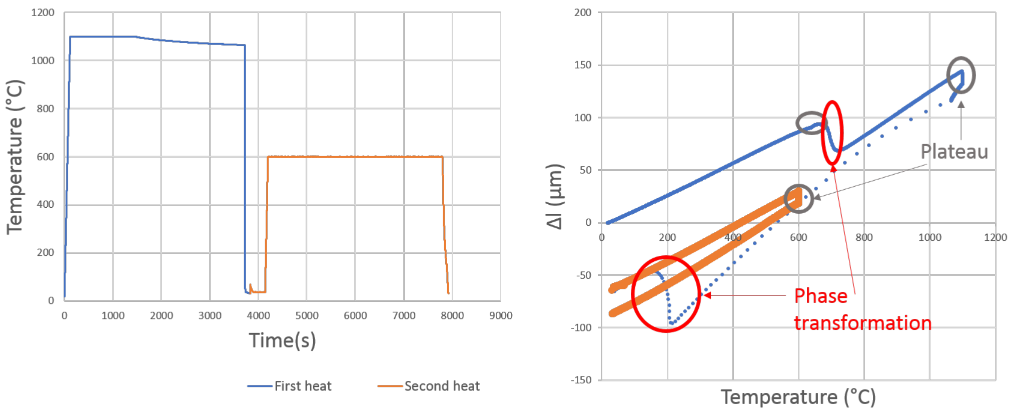

Figure 3.10: Temperature profile of the heat program (Left) and elongation of the sample ΔL versus the temperature for sample *Dilato 1h/1h* (Right)

phenomenon is due to a heat release from the martensitic transformation. Specifically, this transformation is accompanied by the release of latent heat. Hence, the release of latent heat may cause a temporary rise of temperature when the rate of heat liberation during the transformation exceeds the one of heat dissipation while cooling the metal through a transformation temperature range.[92]

In addition, a small bump can be distinguished just before the first phase transformation. This bump is highlighted by a grey circle during the first heating.

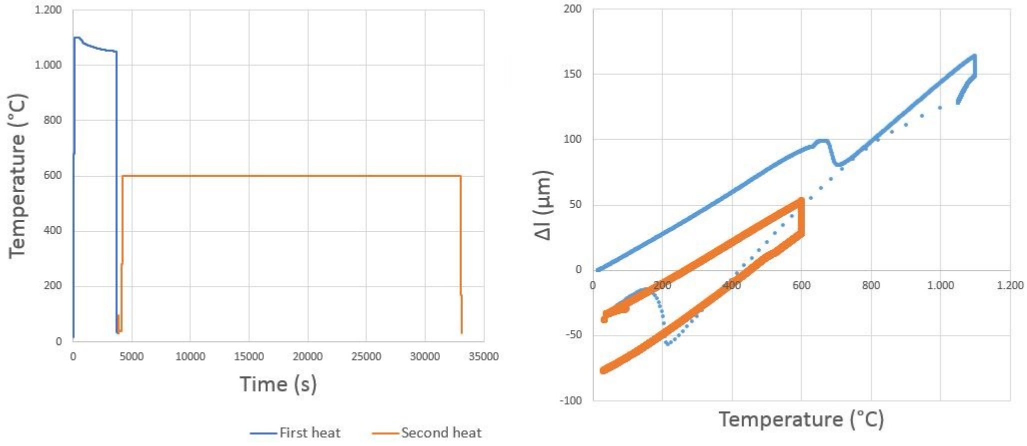

Figure 3.11: Temperature profile of the heat program (Left) and elongation of the sample ΔL versus the temperature for sample *Dilato electropoli* (Right)

On the other hand, the resulting graph of the sample *Dilato electropli* can be found on Figure 3.11. This heat treatment corresponds to the one performed on the sample *Dilato 1h/1h*. The main difference between the two samples comes from the fact that the plateau at $1100°C$ has not been correctly followed by the dilatometer in the sample *Dilato electropoli*.

Since this sample has followed the same heat treatment as the *Dilato 1h/1h* and possess more or less the same behavior, it will not be further analysed.

Third, the resulting graph from the sample *Dilato 15/1h* is presented on Figure 3.12. This graph can be compared with the graph on Figure 3.10 since the only difference in the heat programs is the time of the first plateau: 15 minutes for the sample *Dilato 15/1h* and 1 hour for the sample *Dilato 1h/1h*. Both graphs present two phase transformations around the same range of temperature.

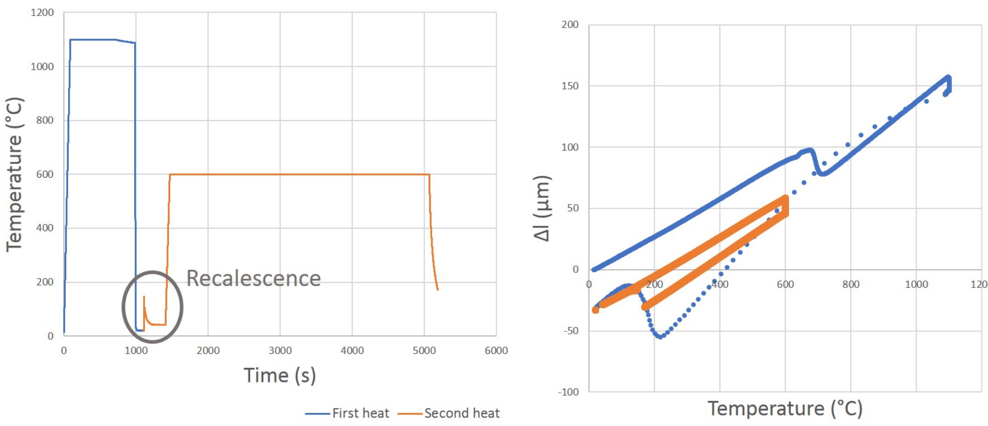

Figure 3.12: Temperature profile of the heat program (Left) and elongation of the sample ΔL versus the temperature for sample *Dilato 15/1h* (Right)

Furthermore, a peak, representing the recalescence, in the temperature profile can be distinguished as well as a bump before the first transformation.

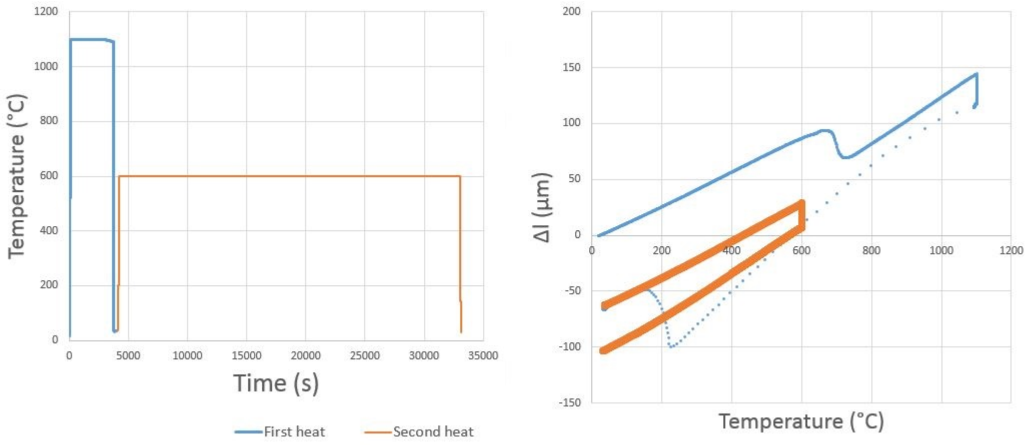

Figure 3.13: Temperature profile of the heat program (Left) and elongation of the sample ΔL versus the temperature for sample *Dilato 1h/8h* (Right)

Fourth, the resulting graph of the sample *Dilato 1h/8h* can be seen in Figure 3.13. On this graph, different elements can be explained. The presence of two phase transformations can be detected thanks to their "S" shape. The first phase transformation occurs around $650°C$ during heating and the second one during cooling around $230°C$.

In addition, the recalescnece phenomenon can be distinguished by a very small peak in the temperature profile. Moreover, a bump before the first transformation can be detected as well.

Fifth, the resulting graph from the sample *Dilato 900* can be seen on Figure 3.14. This graph can be compared with the one presented on Figure 3.10 since their main difference comes from the first plateau temperature and time. In sample *Dilato 900*, a smaller temperature and a shorter time for the first plateau have been tested. The general behaviour of the two graphs is the same but the second phase transformation around $200°C$ seems to happen on a larger range of temperatures for this sample (see in the next section *Martensite transformation*).

Moreover, the contraction during the first cooling is much less important for the *Dilato 900* than for *Dilato 1h/1h* (8 and $26\mu m$ respectively) . Furthermore, a peak, representing the recalescence, in the temperature profile can be distinguished as well as a bump before the first

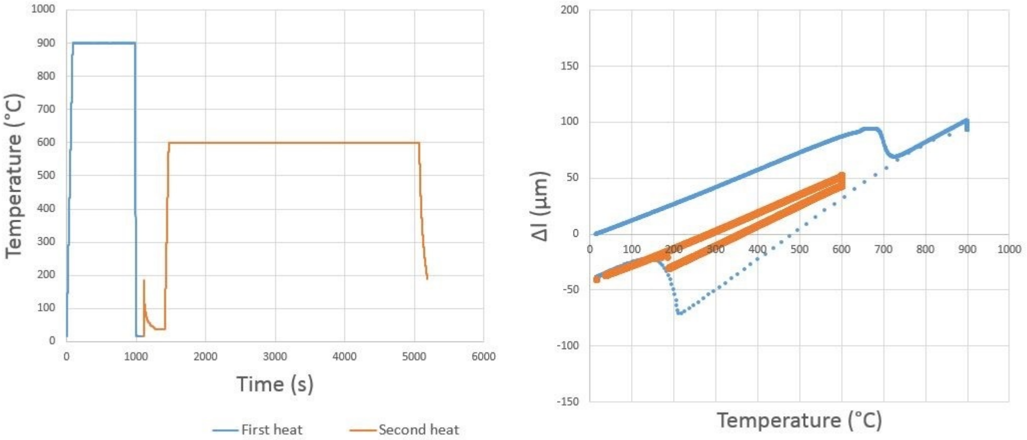

Figure 3.14: Temperature profile of the heat program (Left) and elongation of the sample ΔL versus the temperature for sample *Dilato 900* (Right)

transformation in the resulting graph.

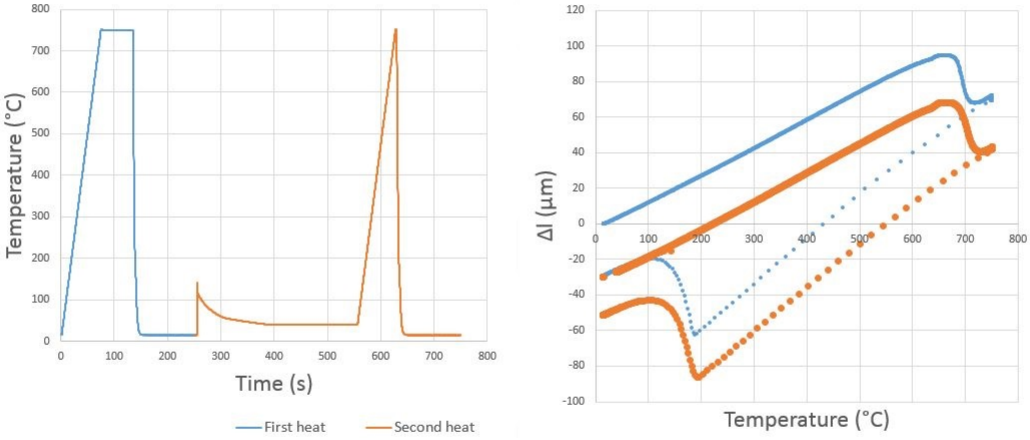

Figure 3.15: Temperature profile of the heat program (Left) and elongation of the sample ΔL versus the temperature for sample *Dilato 750* (Right)

Seventh, the resulting graph from the sample *Dilato 750* is depicted in Figure 3.15. The main difference with the previous heat treatment was the change of the temperature plateau: two plateaus at 750°C for very short time (1 minute and 2 seconds respectively) were performed while a plateau at 600°C and 1100°C was done previously. Since the plateau is much more shorter, no true contraction at 750°C can be noticed.

Moreover, four phase transformations can be highlighted: two around 750°C and two around 200°C. Again, as well as for the first samples, there is an increase of the elongation during the heating and a contraction during the cooling. In addition, only one peak, representing the recalescence, in the temperature profile can be distinguished. In addition, a small bump before the first transformation can be distinguished.

Eighth, the graph resulting from the thermal cycling program can be seen on Figure 3.16. By comparing Figures 3.13 and 3.16 it can be noticed that the last part of the graphs presents the same behaviour. Moreover, as well as for the graph on Figure 3.15, four phase transformations can be observed at approximately the same positions.

Furthermore, it can be observed that after a plateau at smaller temperature and for a smaller time, the plateau at 600°C for one hour behave similarly as the one of Figure 3.10. In

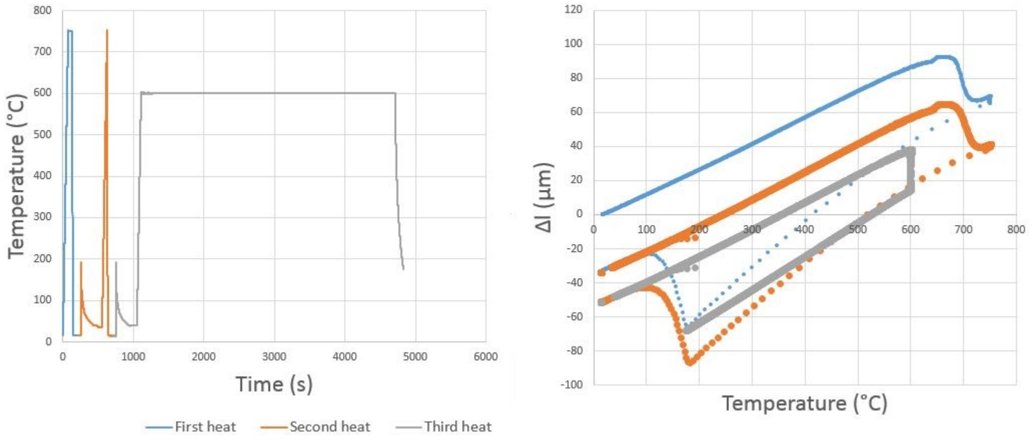

Figure 3.16: Temperature profile of the heat program (Left) and elongation of the sample ΔL versus the temperature for sample *Dilato cycling* (Right)

addition, there are two peaks, representing the recalescence, in the temperature profile that can be distinguished. Moreover, a bump before the first transformation can be distinguished in the resulting graph of the extension versus the temperature.

2.1.1.1 Thermal expansion coefficients

The thermal expansion coefficients have been calculated for the ferrite phase $\alpha_{ferrite}$, as well as for the austenite phase α_{a1}, α_{a2} and α_{a3} for each of the samples. The definition of those coefficients can be found on Figure 3.17.

The thermal expansion coefficients of the ferrite and austenite phase calculated near the phase transformations are summarised in Table 3.1.

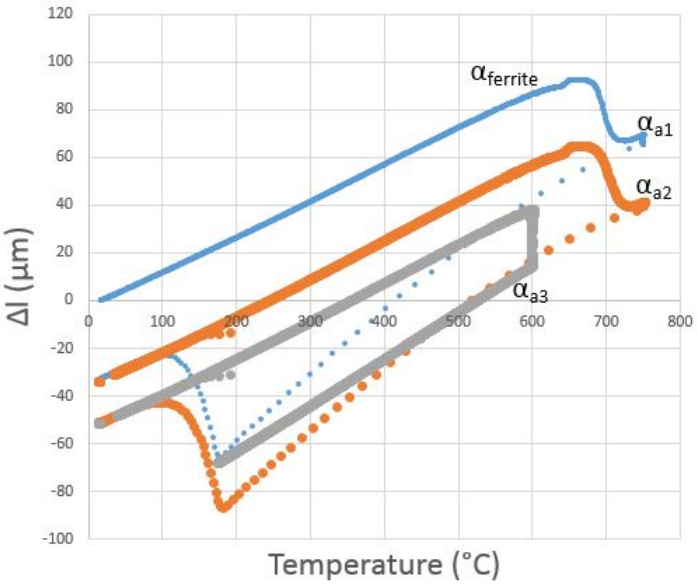

Figure 3.17: Definition of the thermal expansion coefficients

First, it can be highlighted that all the ferrite thermal expansion coefficients are approximately equal to $15 * 10^{-6}/°C$. The lowest values correspond to the thermal cycling and the *Dilato 900* whereas the larger value is linked with the sample *Dilato electropoli*. In addition, the thermal

Table 3.1: Summary of the thermal expansion coefficients

Sample	$\alpha_{ferrite}$ $[10^{-6}/°C]$	α_{a1} $[10^{-6}/°C]$	α_{a2} $[10^{-6}/°C]$	α_{a3} $[10^{-6}/°C]$
Dilato 1h/8h	15.27	20.88	16.43	
Dilato 1h/1h	15.14	20.84	16.64	
Dilato 750	15.47	9.42	15.47	
Dilato cycling	15.07	9.11	15.38	15.44
Dilato 900	15.06	19.74	15.91	
Dilato electropoli	15.95	22.25	15.75	
Dilato 1h	15.47	21.23		
Dilato 15/1h	15.38	21.29	15.84	

expansion coefficients of the ferrite of the samples are not the same although they follow the exact same plateau.

Second, the thermal expansion coefficients of the austenite, α_{a1}, α_{a2} and α_{a3} are higher than the $\alpha_{ferrite}$ except for the samples *Dilato 750* and *Dilato cycling.* In addition, more changes in the values of the thermal expansion coeffcients of the austenite can be distinguished.

Furthermore, it should be noticed, that in the case of the thermal expansion of α_{a1}, α_{a2} and α_{a3}, not only an austenite phase will be present. Hence, depending of the phase transformation, the presence of martensite as well as austenite could be distinguished.

2.1.1.2 The martensite transformation

The martensite transformation temperatures are gathered in Table 3.2 with an acceptable error of $1°C$.

Table 3.2: Summary of the martensite transformation temperatures: M_S and M_f

Sample	$M_{S1}[°C]$	$M_{f1}[°C]$	$M_{S2}[°C]$	$M_{f2}[°C]$
Dilato 1h/8h	230	145		
Dilato 1h/1h	215	152		
Dilato 750	193	103	195	96
Dilato cycling	178	98	183	85
Dilato 900	215	145		
Dilato electropoli	215	155		
Dilato 1h	222	137		
Dilato 15/1h	218	100		

By comparing the M_{S1} and M_{f1} temperatures, it can be noticed that the highest value corresponds to the sample *Dilato 1h/8h* whereas the smallest value is linked with the *Dilato cycling* sample. In addition, those values are very different: the highest value is around $230°C$ while the smallest one is around $178°C$. In addition, when the temperature or the time of homogenization is decreased, no effect can be highlighted. On the other hand, it can be highlighted that even if the previous heat treatment is the same, it does not result in the same M_S and M_f temperatures.

Furthermore, by comparing the M_{S2} temperatures, it can be highlighted that their values are slightly higher than the ones of the M_{S1}. Moreover, their M_{f2} temperatures are much more lower than the M_{f1} temperatures.

2.1.2 Variation of the elongation of the samples with time

The graphs of the elongation of the sample versus the time are presented on Figures 3.18 and 3.19.

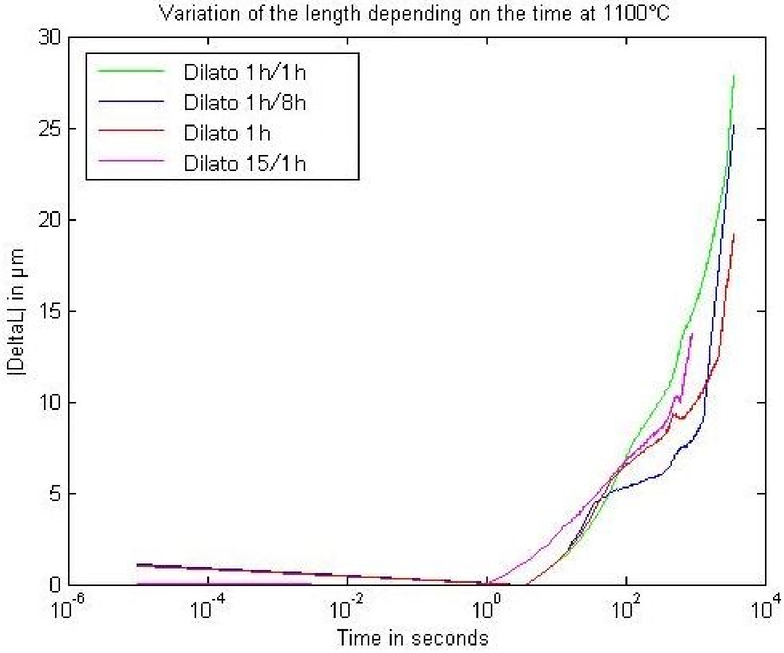

Figure 3.18: elongation of the sample $|\Delta L|$ versus the time at $1100°C$

First, from the Figure 3.18, it can be noticed that all curves follow an exponential behaviour. Moreover, all the samples that had to sustain the plateau at $1100°C$ for 1 hour behave more or less the same way. Hence, there is almost no elongation until 10^2 seconds were all the curves increase abruptly.

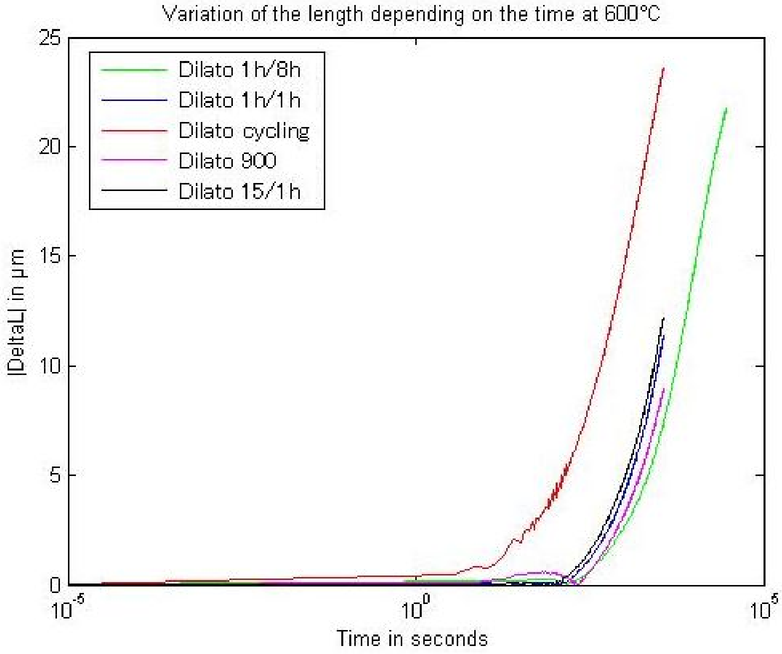

Figure 3.19: elongation of the sample $|\Delta L|$ versus the time at $600°C$

Thereafter, comparing Figures 3.18 and 3.19 it can be noticed that the curves will follow an exponential behaviour for both temperatures. Moreover, by looking closely to Figure 3.19 it can be observed that all the curves are very close to each other except the curve of the sample *Dilato cycling.* Although all the curves follow the same general behaviour, the curve of sample *Dilato cycling* increases much more faster than the other ones.

On the other hand, comparing sample *Dilato 15/1h* and *Dilato 1h/1h*, no large differences can be highlighted except that the curve of the sample *Dilato 15/1h* presents a faster increase of expansion and a slight increase of the final expansion reached.

Furthermore, it can be noticed that the slowest sample is *Dilato 1h/8h.* Indeed, even the sample *Dilato 900* behaves faster than the *Dilato 1h/8h.*

Finally, all the samples reach more or less the same expansion except the samples *Dilato cycling* and *Dilato 1h/8h* which reach the largest expansion.

2.2 Microstructure characterization of the dilatometry and furnace samples

The presence of two phases has been highlighted thanks to a chemical attack. Specifically, it consisted in an attack with a Behara reagent 20 seconds. The resulting microstruture is presented on Figure 3.20. It can be highlighted that the austenite phase corresponds to the lighter regions whereas the martensite phase is linked with the darker regions.[93]

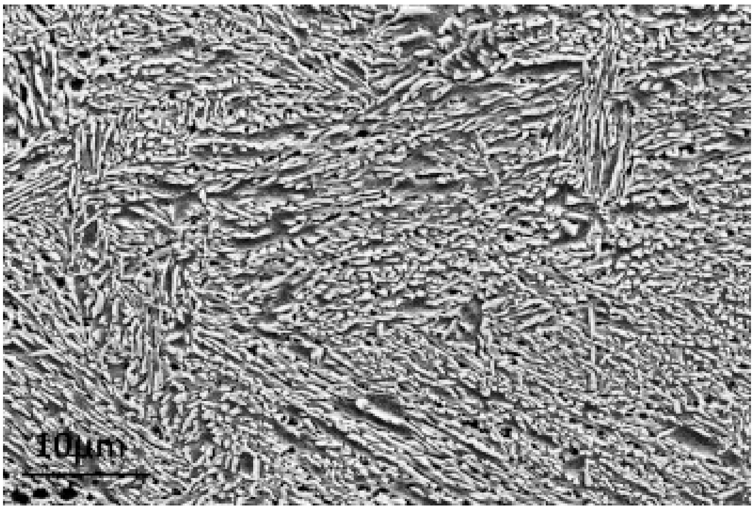

Figure 3.20: Chemical attack on the sample *Furnace 8h*

In Figure 3.21 (a), the microstructure of the sample *Dilato 1h/1h* is presented. In this microstructure two elements can be distinguished: equiaxed films and more dense regions. Hence, they represent the presence of austenite and martensite respectively.

In addition, the microstructure of the sample *Furnace 1h* can be observed in Figure 3.21 (b). Again the presence of martensite and austenite can be distinguished.

On the other hand, there is a distribution of the grain size of the grains, but a characteristic size of $30 \pm 10 \mu m$ can be distinguished [2].

Thereafter, in Figure 3.22, the microstructure of the sample *Dilato 1h/8h* and the sample *Furnace 8h* can be observed. As well as in the previous sample, the presence of austenite and martensite can be distinguished.

---

[2] For all samples analysed in this section, only a characteristic size of the grains will be given, since there is a distribution of the grain size.

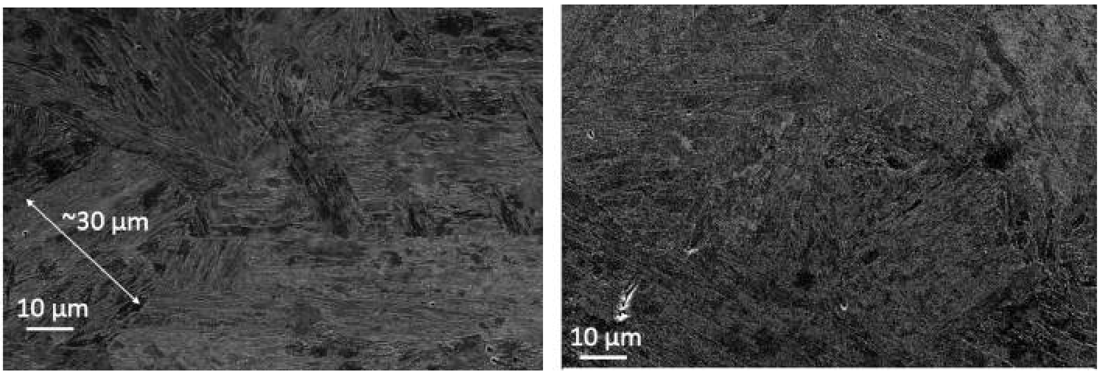

(a) (b)

Figure 3.21: Comparison of the microstructure between the samples *Dilato 1h/1h* (a) and *Furnace 1h* (b) in the center

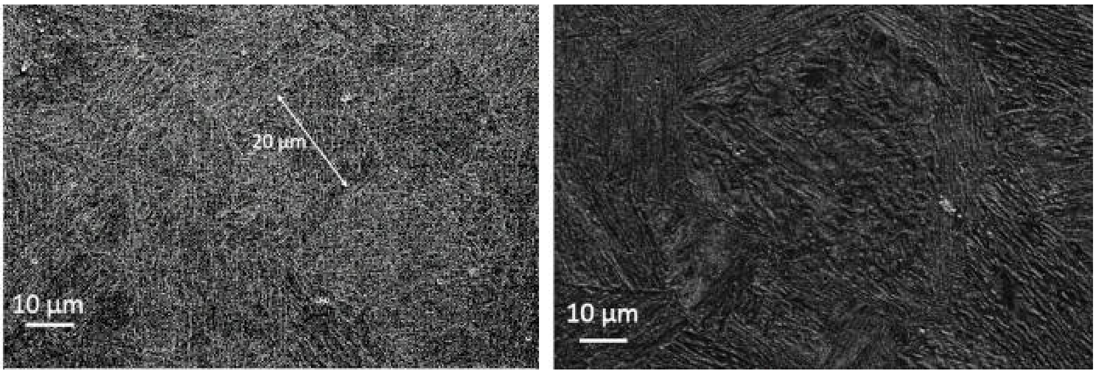

(a) (b)

Figure 3.22: Comparison of the microstructure between the samples *Dilato 1h/8h* (a) and *Furnace 8h* (b) in the center

Moreover, a characteristic size of $20 \pm 10\mu m$ can be noticed. Furthermore, by comparing Figures 3.22 (b) and 3.21 (b) it can be highlighted that the sample *Furnace 8h* shows broader austenite grains.

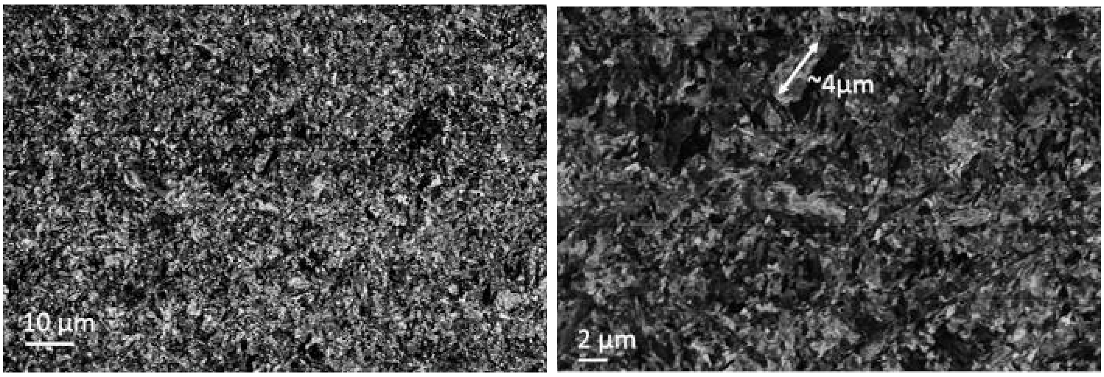

Figure 3.23: Microstructure of the sample *Dilato 750* in the center

Then, the microstructure of the sample *Dilato 750* can be observed in Figure 3.23. Contrary to the microstructure obtained above, very small aggregates can be distinguished. Moreover, the size of these aggregates is very small, about $4 - 5\mu m$.

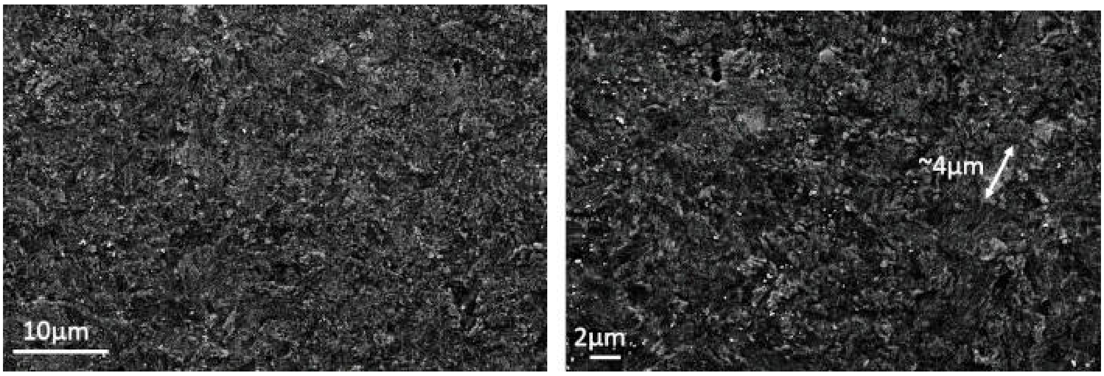

Figure 3.24: Microstructure of the sample *Dilato cycling* in the center

In Figure 3.24, the microstructure of the sample *Dilato cycling* can be noticed. As well as for the first samples, the presence of austenite and martensite can be distinguished by the small equiaxed films and denser regions.

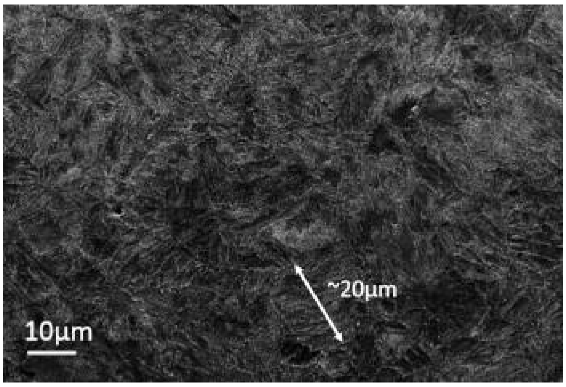

Figure 3.25: Microstructure of the sample *Dilato 900* in the center

Furthemore, on Figure 3.25, the microstructure of the sample *Dilato 900* can be observed. Again, the presence of martensite and austenite can be distinguished. The grain size is approximately $20 \pm 5 \mu m$.

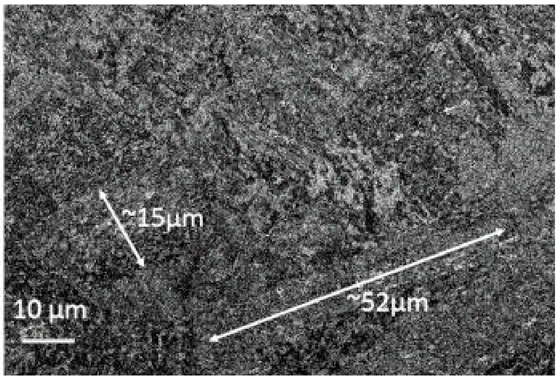

Figure 3.26: Microstructure of the sample *Dilato 1h* in the center

In Figure 3.26, the microstructure of the sample *Dilato 1h* can be observed. In this sample, only the presence of martensite can be distinguished. Moreover, a large broad distribution of grain size can be observed: $15 - 52\mu m$.

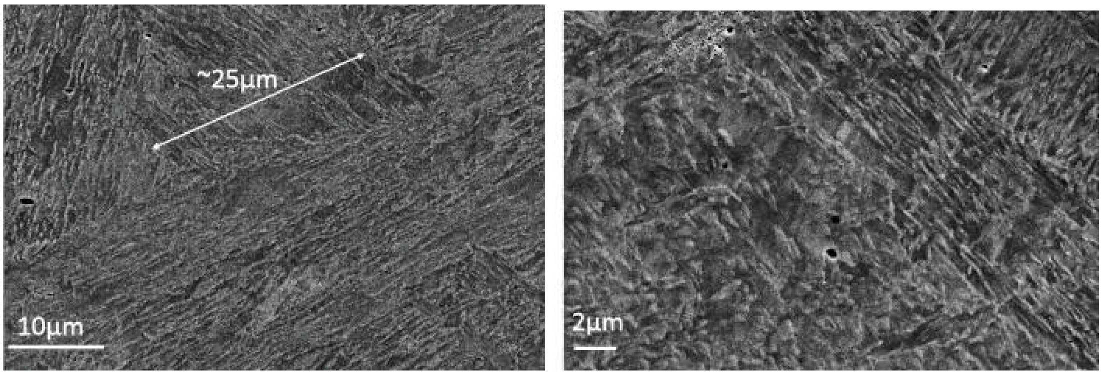

(a) Center of the sample (b) Center of the sample

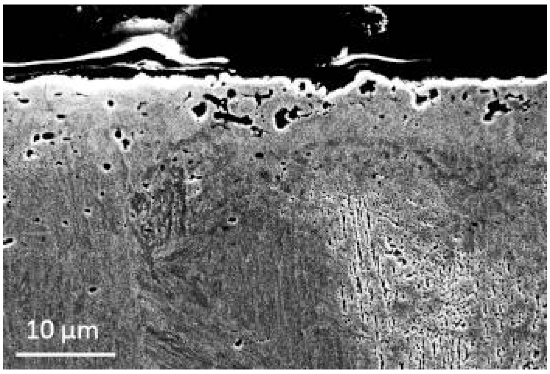

(c) Edge of the sample

Figure 3.27: Microstructure of the sample *Dilato electropoli* in the center and in the egde

On Figure 3.27, the microstructure along the thickness of the sample *Dilato electropoli* can be seen. There is still the presence of austenite and martensite. Moreover, the grain size is approximately $25 \pm +10\mu m$.

In addition, in the edge of the sample, lots of porosity can be noticed. On the other hand, in the center of the sample, there are only few porosity that can be distinguished.

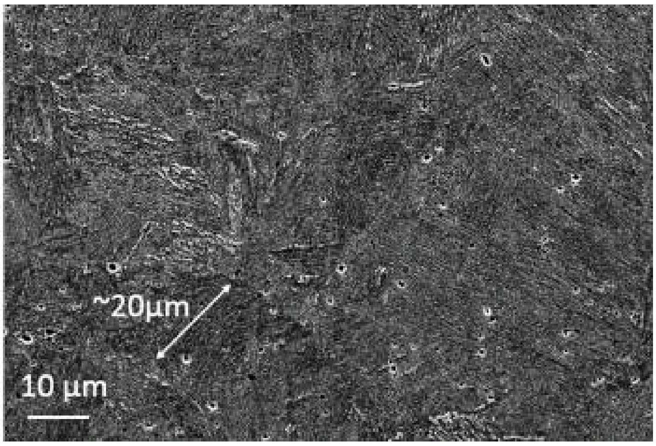

Figure 3.28: Microstructure of the sample *Dilato 15/1h* in the center

Then, in Figure 3.28, the microstructure of the sample *Dilato 15/1h* can be detected. As well as for the first samples, the presence of austenite and martensite can be distinguished. In addition, the grain is approximately $20 \pm 10\mu m$.

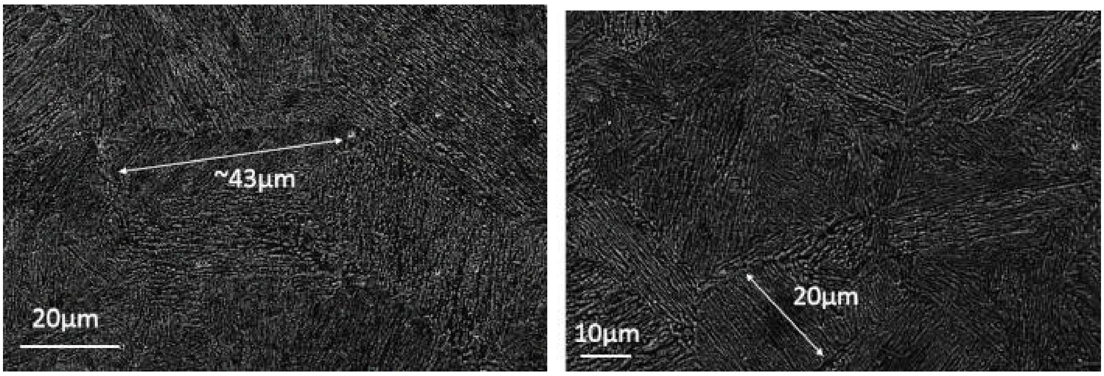

(a) (b)

Figure 3.29: Microstructure of the sample *Furnace 24h* (a) and *Furnace 48h* (b) in the center

In Figure 3.29 (a), the microstructure of the sample *Furnace 24h* can be observed. Again, martensite and austenite can be distinguished. In addition, the grain size is approximately equal to $40 \pm 10\mu m$.

Finally, in Figure 3.29 (b), the microstructure of the sample *Furnace 48h* can be seen. As well as for the previous samples, martensite and austenite can be distinguished. Furthermore, the grain size is about $20 \pm 10\mu m$.

2.3 X-Ray diffraction results

The fraction of austenite in each sample is summarised in Table 3.3.

Table 3.3: Summary of the austenite fraction in the dilatometry and furnace samples

Sample	Integration method %	Rietveld method %
Dilato 1h/8h	39,35	40,5
Furnace 8h	29,70	
Dilato 1h/1h	43,95	38,4
Furnace 1h	17,67	
Dilato 750	3,89	0
Dilato cycling	38,90	39,8
Dilato 900	21,15	
Dilato 15/1h	30,62	
Furnace 24h	34,20	
Furnace 48h	24,02	

The resulting graphs from the XRD of the samples quantify by the Rietveld method are presented on Figure 3.30.

2.3.1 Quantification of the austenite fraction by the integration method

By observing Table 3.3, it can be noticed that the sample *Dilato 1h/1h* presents the highest fraction of austenite. On the other hand, it is the sample *Dilato 750* that presents the lowest austenite fraction.

Moreover, the samples *Dilato cycling* has more or less the same austenite fraction as the sample *Dilato 1h/8h*. Furthermore, the sample *Dilato 900* presents a decrease of its austenite

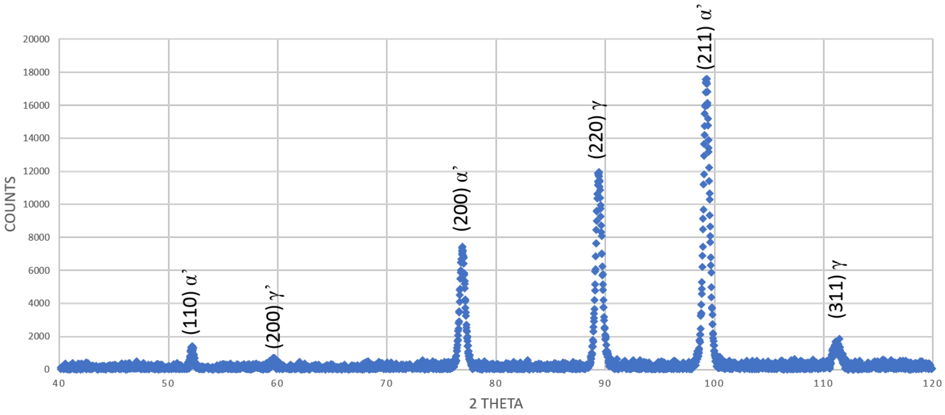

(a) XRD resulting spectra of the the sample *Dilato 1h/1h*

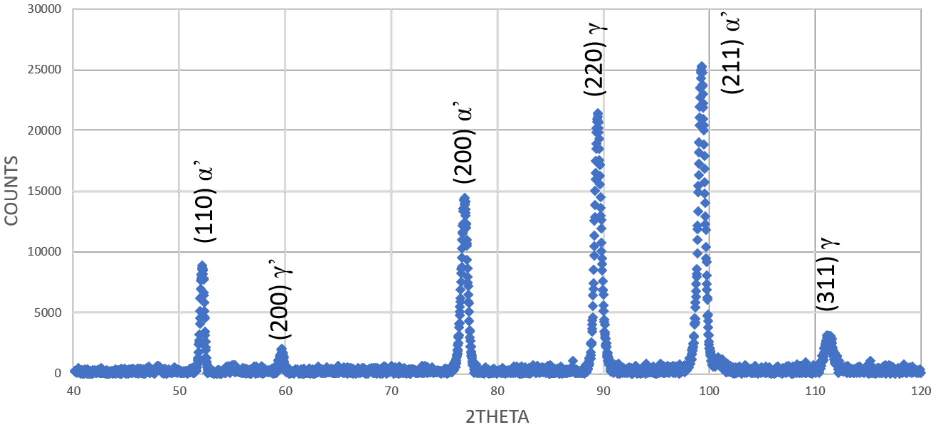

(b) XRD resulting spectra of the the sample *Dilato 1h/8h*

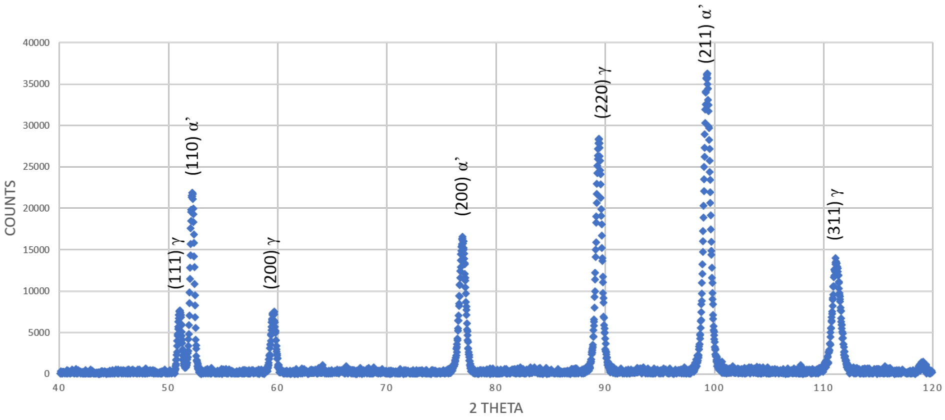

(c) XRD resulting spectra of the the sample *Dilato cycling*

Figure 3.30: Resulting graph of the XRD - Counts versus the 2 theta angle

fraction compared to the other samples. Although, the sample *Dilato 15/1h* presents a decrease in the austenite fraction as well, it still maintains a higher fraction than the sample *Dilato 900*.

On the other hand, the austenite fraction seems to increase with the time of the plateau at 600°C for the furnace samples except for the *Furnace 48h* sample. Moreover, the austenite fraction of the furnace samples seems much lower than the corresponding dilatometry samples.

2.3.2 Quantification of the austenite fraction by the Rietveld method

From Table 3.3, it can be highlighted that the larger fraction of austenite is attributed to the sample *Dilato 1h/8h* whereas the smaller fraction of austenite is attributed to the sample *Dilato 1h/1h.* In addition, there are no large differences between the fraction obtained with the Rietveld method except the sample *Dilato 750* which presents no austenite fraction.

3 Metastable austenite

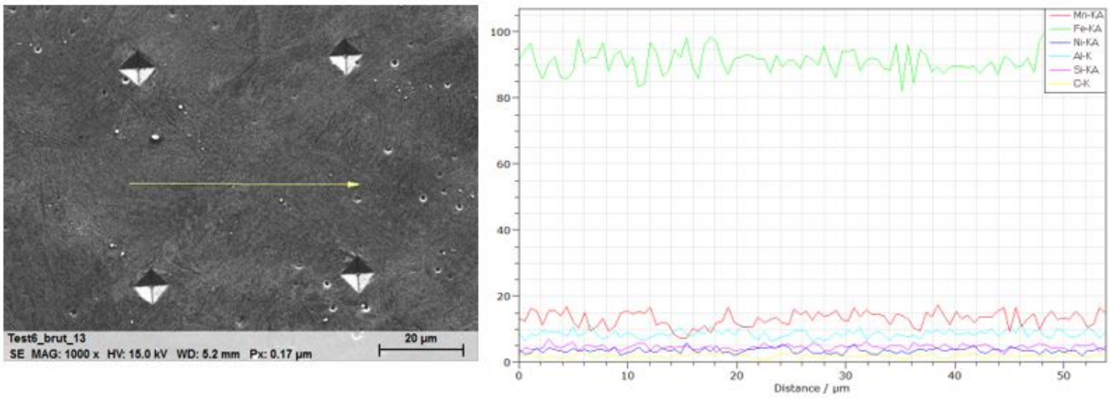

Figure 3.31: EDX scan on the microstructure of the sample *Dilato electropoli* - First scanning of the square

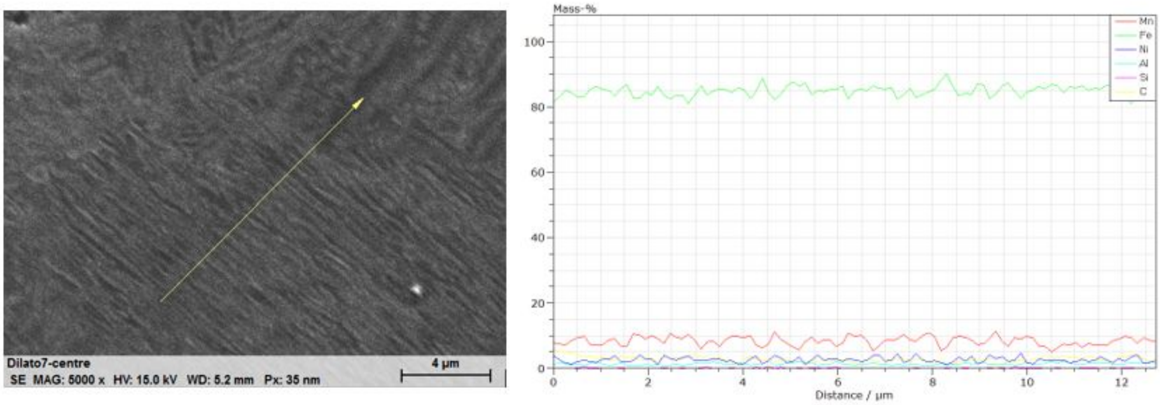

Figure 3.32: EDX scan on the microstructure of the sample *Dilato electropoli* - Second scanning inside a grain in the square

In this section, the results of the EDX analysis on the sample *Dilato electropoli* are presented. On Figures 3.31 and 3.32, the two scanning performed inside the square delimited by four indents can be observed.

It can be highlighted that iron content is lower in the second scanning performed. Moreover, more fluctuations can be distinguished in the scanning performed on the whole square. In addition, the mass percentage of all the elements considered seems globally higher for the scanning on the whole sample.

Furthermore, carbon and silicon content are very low in the scanning in the grain. On the other hand, their content are higher and do much variate in the scanning on the whole square.

4 Mechanical tests

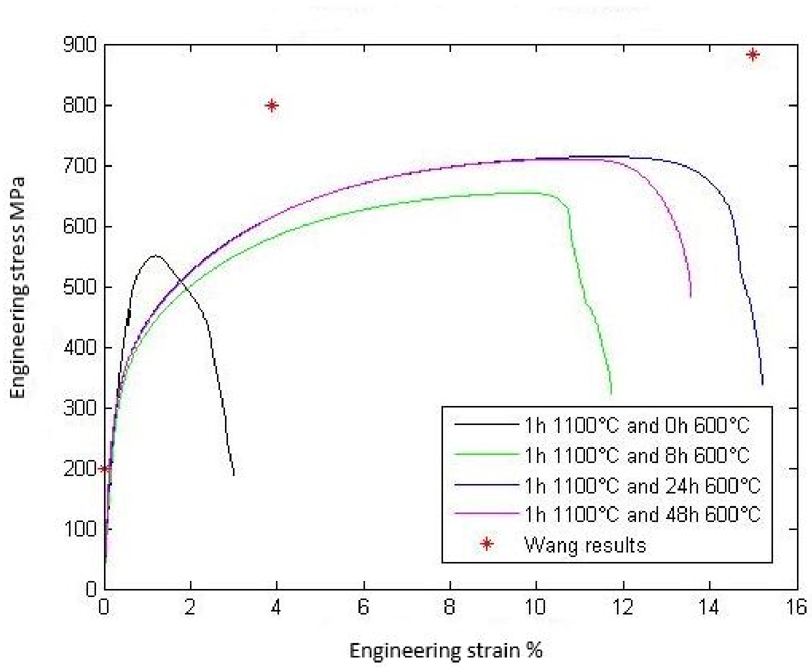

(a) Engineering elongation versus engineering stress of the four specimens

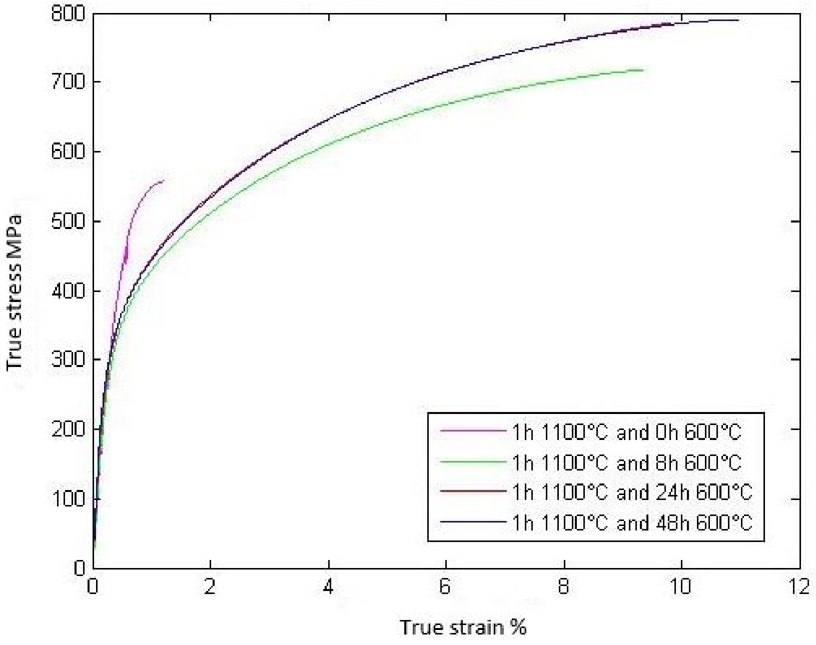

(b) True elongation versus true stress of the four specimens

Figure 3.33: Graph of the stress and strain of the four specimens

In this section, the results of the mechanical tests are presented. First, the true and engineering graphs will be exposed. Thereafter, the yield strength of the specimens will be given.

The mechanical results of the tensile tests performed on the samples *Specimen 0h*, *Specimen 8h*, *Specimen 24h* and *Specimen 48h* are shown in Figures 3.33a and 3.33b.

From the Figure 3.33 (a) it can be noticed that all the curves of the specimen tested are below the one obtained by Wang et al [67]. Moreover, the curves of the specimen *Specimen 24h* and *Specimen 48h* are almost exactly the same. In addition, the curve of the sample *Specimen 8h* is much more lower than the other curves. Finally, it can be highlighted that the curve of the sample *Specimen 0h* reaches the lowest elongation at fracture.

Table 3.4: Summary of the yield strength taken at $\epsilon^{pl} = 0.2\%$, $\sigma_{y0.2}$

Sample	$\sigma_{y0.2}[MPa]$
Specimen 0h	452,6
Specimen 8h	337,3
Specimen 24h	341,4
Specimen 48h	343,3

On the other hand, by looking at Table 3.4, it can be highlighted that the sample *Specimen 0h* has the highest yield strength. Hence, the yield strength of the different sample can be classified as follows : $\sigma_{Specimen0h} > \sigma_{Specimen48h} > \sigma_{Specimen24h} > \sigma_{Specimen8h}$.

From Figure 3.33(b), it can be observed that the curves of the samples *Specimen 24h* and *Specimen 48h* are exactly the same. Furthermore, whereas the curve of the sample *Specimen 0h* is above all the curves, it is the curve of the sample *Specimen 8h* that is below all the curves.

5 Corrosion

In this section, the corrosion results will be exposed. First, the corrosion rates of the immersion tests will be summarised. Then, the final microstructure of the samples will be analysed.

5.1 Corrosion rates

Table 3.5: Summary of the corrosion rates

Sample	v_{corr} **expressed in** g/m^2day
7 days immersion	
Immersion 0h/week	0.633
Immersion 8h/week	0.367
Immersion 24h/week	0.339
1 day immersion	
Immersion 0h/day	0.393
Immersion 8h/day	0.397
Immersion 24h/day	0.307
1 hour immersion	
Immersion 0h/1h	2.613
Immersion 8h/1h	3.615

The corrosion rates of the immersion samples are gathered in Table 3.5 and schematically represented in Figure 3.34. In order to calculate those corrosion rates, an approximation has been done. As a reminder, the equation that links the corrosion rate expressed in $gm^{-2}day^{-1}$ with the ion concentration released is as follows:

$$CR = \frac{cV}{ST} \tag{3.1}$$

where CR is the corrosion rate, c the released ion concentration in g/ml, V the volume of immersion solution in ml, S the surface area of the specimen m^2 and t is the time in days.

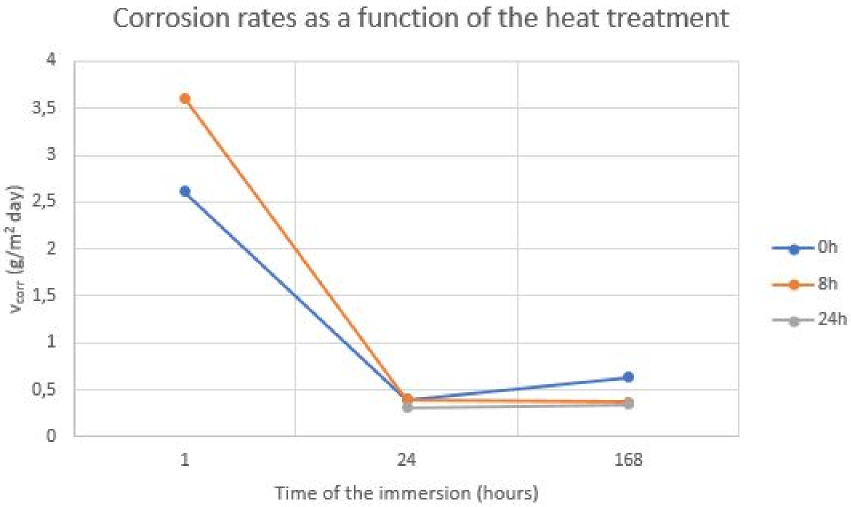

Figure 3.34: Corrosion rates as a function of the heat treatments and the immersion time

[73] This equation was already stated in Chapter 1 and Chapter 2. In order to calculate the released ion concentration, an ICP has been performed on the solution after the immersion. Hence, the released ion concentration c has simply been calculated by summing the concentration of manganese, iron, aluminum and nickel found by the ICP. As a result, the corrosion rates calculated may not be the true rates due to the fact that the element considered do not present the same ion form.

From Table 3.5, it can be highlighted that the corrosion rate of the sample *Immersion 24h/week* is the lowest one whereas the corrosion rate of the sample *Immersion 0h/week* is the largest one for the immersion tests during a week. Moreover, for an immersion of 1 hour, the corrosion rate of the sample *Immersion 0h/1h* is lower than the one of the sample *Immersion 8h/1h*. Furthermore, during an immersion of one day, it appears that the sample *Immersion 24h/day* is lower than the other samples even if the values are very close.

On the other hand, by comparing the different times of immersion, it can be noticed that the immersion samples that had sustained the same heat treatment do not result in the same corrosion rate.

Furthermore, it can be highlighted that the corrosion rates of an immersion time of 1 hour are much larger than the one of an immersion time of 1 or 7 days.

In addition, it should be reminded that those trends are based on only one run of immersion tests.

The solid and the released ions in solution ratios of the element of the alloy can be compared. The different ratios are gathered in Table 3.6.

First, by comparing the ionic and solid ratios for an immersion of one week, it can be noted that the released ions in solution ratios $\frac{Fe}{Mn}$ are all smaller than the solid ratios whereas the opposite is true for the ratios $\frac{Fe}{Ni}$ and $\frac{Fe}{Al}$.

Second, for an immersion time of one day, it can be deducted that the released ions solution ratios of $\frac{Fe}{Mn}$ and $\frac{Fe}{Al}$ are smaller than the solid ratios whereas the the opposite is true for the ratios $\frac{Fe}{Ni}$. In addition, it can be found that the released ions solution ratios $\frac{Mn}{Al}$ for 0 and 8 hours are as well smaller than the solid ratios: 4.6 to 6.6 respectively for the ions released solution ratios compared to 6.96 for the solid ratio.

Third, for an immersion of one hour, it can be noted that the ionic ratios $\frac{Fe}{Mn}$ and $\frac{Fe}{Al}$ are again smaller than the solid ratios whereas the opposite is true for the ratios $\frac{Fe}{Ni}$. Moreover, it can be found that the ionic ratios $\frac{Mn}{Al}$ for 0 and 8 hours are as well smaller than the solid ratios: around 1 to 1.6 respectively for the ions released solution ratios compared to 6.96 for the solid

Table 3.6: Solid and ionic ratios of the elements

Sample	$\frac{Fe}{Mn}$	$\frac{Fe}{Ni}$	$\frac{Fe}{Al}$
Solid ratios			
Solid sample	9,73	29,79	67,73
Released ions in solution ratios			
7 days immersion			
Immersion 0h/week	8,56	32,36	593,33
Immersion 8h/week	8,15	53	353,33
Immersion 24h/week	8,24	40,17	241
1 day immersion			
Immersion 0h/day	7,48	172	34,4
Immersion 8h/day	4,18	133	26,6
Immersion 24h/day	4,71	113	22,6
1 hour immersion			
Immersion 0h/1h	9,4	47	9,4
Immersion 8h/1h	5,25	42	8,4

ratio.

Finally, comparing the heat treatments and the ionic ratios associated, it can be highlighted that except for an immersion of one week, the samples annealed for 0 hour presents the largest ionic ratios. On the other hand, it can be noted that the samples annealed for 8 hours always present the smallest $\frac{Fe}{Mn}$ ionic ratios but their ionic ratios $\frac{Fe}{Al}$ and $\frac{Fe}{Ni}$ are always larger than the ones of the samples annealed for 24 hours.

5.2 Microstructure characterization

The morphological changes as well as the analysis of the surface composition will be investigated through this section

5.2.1 1 week immersion

The microstructures of the samples immersed for 1 week are presented on Figures 3.35, 3.36 and 3.37. Several elements can be highlighted from those microstructures:

- **The hole** A large region around the hole was attacked. In addition, some very large cracks and pits could be found in the regions near the hole. Moreover, deposited layers could be distinguished on all the samples in the region around and below the hole. Furthermore, corrosion products were detected in the region below the hole as in Figure 3.35c. On the other hand, the other regions were not similarly attacked.

- **The edges** For each sample, all the edges were attacked. In addition, some corrosion products were able to be distinguished as in Figures 3.35e and 3.36d. Moreover, black spots can be distinguished as in Figures 3.35e and 3.37d.

Several EDX have been performed on the immersed samples of 1 week. Only a qualitative analysis can be performed since the corrosion layer is very thin. In Figure 3.38, the EDX analysis close to the hole of the sample *Immersion 0h/week* is presented. From that analysis, the behavior of the cracking deposits layers as well as the underneath metal could be highlighted. The cracking deposit layers (named *Couche* and *Couche bis*) present considerable amounts of oxygen and lower amounts of iron and carbon. The alloying elements content is very low. In addition, there are as

(a) The hole (b) Region near the hole

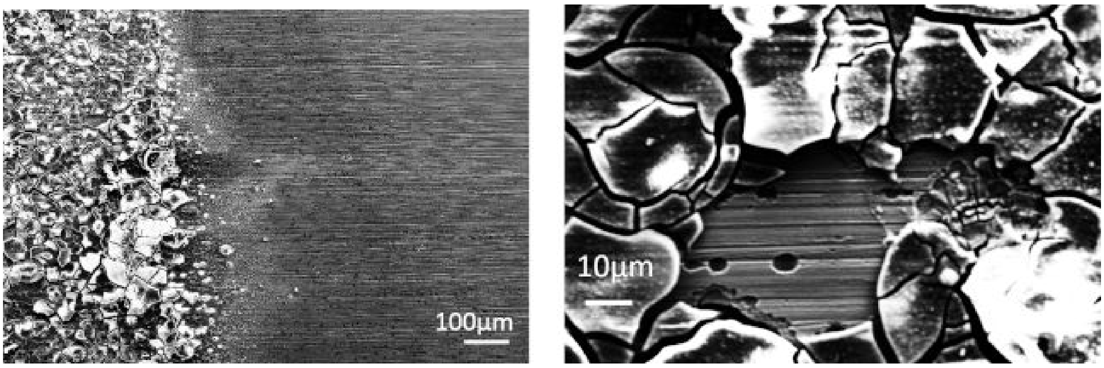

(c) Below the hole (d) Magnification below the hole

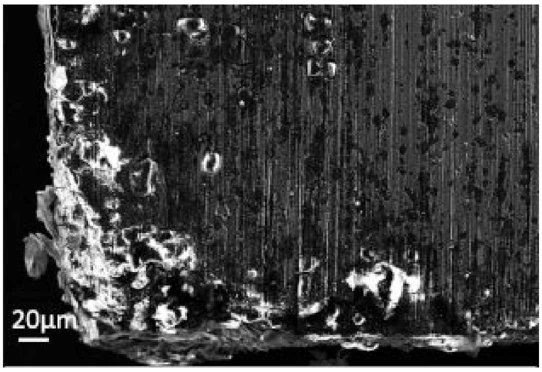

(e) Edge of the sample

Figure 3.35: Microstructure of the sample *Immersion 0h/week*

well small amounts of phosphorus followed by chlorine and silicon and in lower amounts sodium followed by calcium. The underneath metal presents much larger amounts of iron and alloying elements. But, there is still a high content of oxygen and carbon.

Furthermore, the EDX analysis performed close to the edge is summarised on Figure 3.39. It should be noted that the presence of magnesium, chlorine and sodium has not been investigated in this analysis. The cracking deposit layer (named *Couche* in this analysis) presents large amount of oxygen as well as low amounts of iron followed by carbon. There are very low contents in alloying elements except for aluminum who keeps a high level. In addition, there are as well small content of phosphorus followed by calcium and lower amounts of silicon. Moreover, the underneath metal presents a slightly higher iron content than the couche but there is still a high content in carbon and oxygen. The content in alloying elements is also increased except for aluminum. Furthermore, there is still a non-negligible amount of phosphorus. The *Trou* presents very large amount of oxygen followed by carbon and a small iron content. There is still a lower content of alloying elements except for aluminum. There is as well non-negligible amounts of

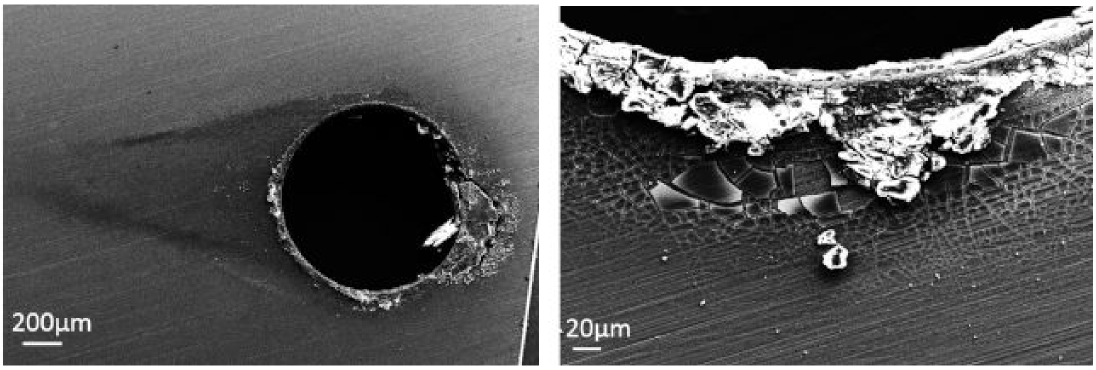

(a) The hole (b) Region near the hole

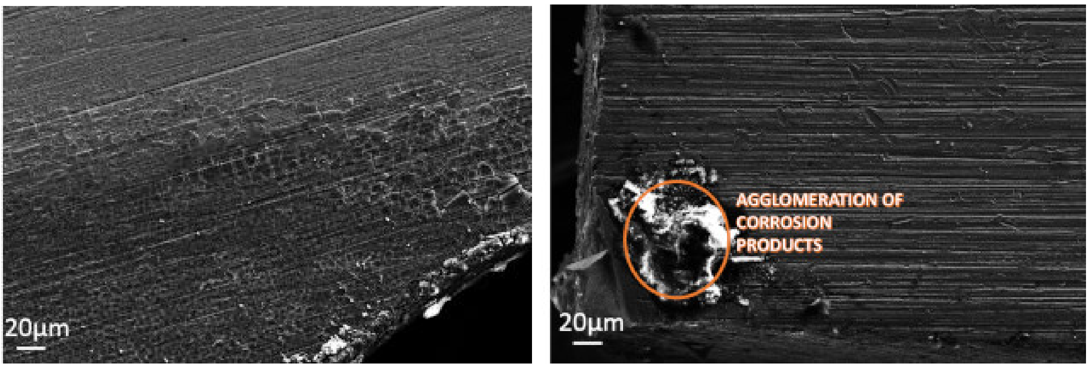

(c) Below the hole (d) Edge of the sample

Figure 3.36: Microstructure of the sample *Immersion 8h/week*

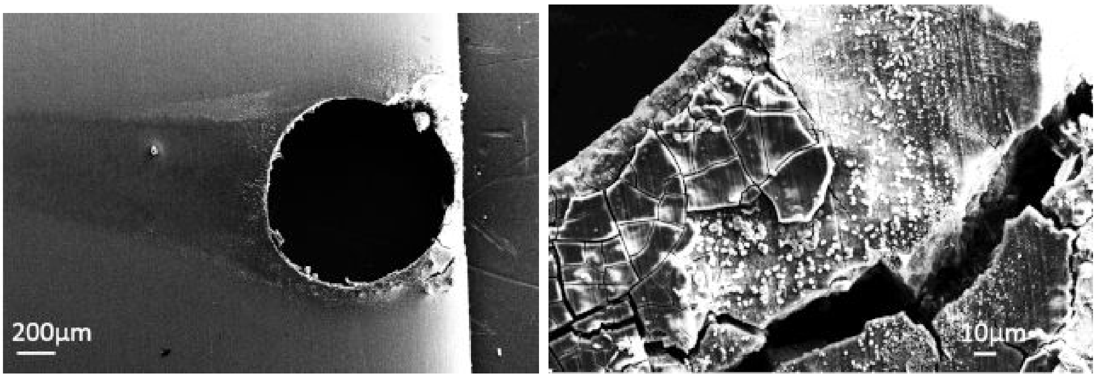

(a) The hole (b) Region near the hole

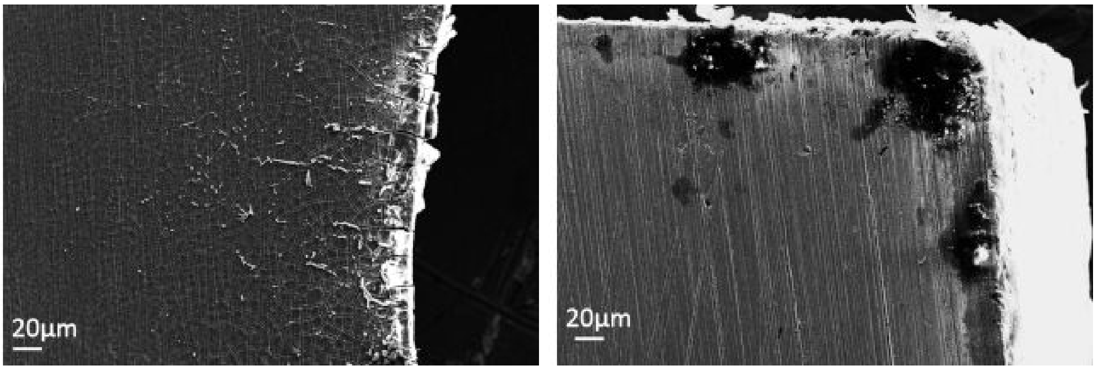

(c) Below the hole (d) Edge of the sample

Figure 3.37: Microstructure of the sample *Immersion 24h/week*

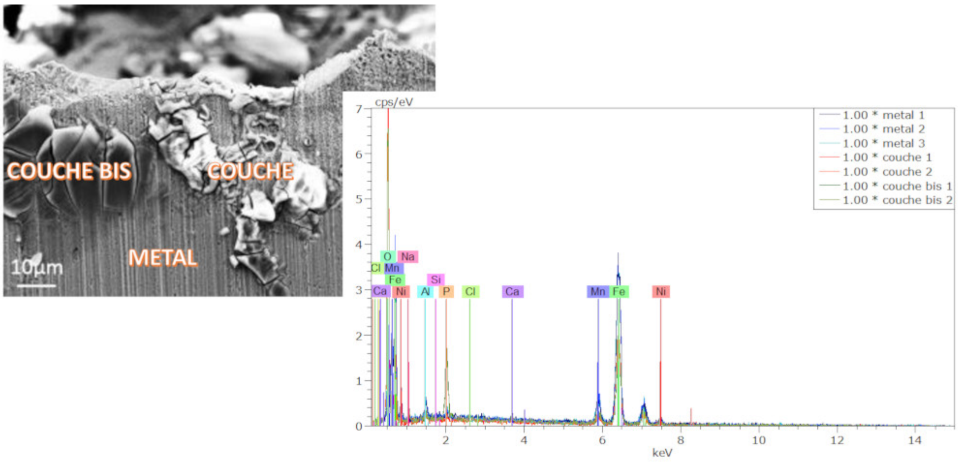

```
Atomic percent (%)

Spectrum          C     O   Na   Al   Si    P   Cl   Ca   Mn    Fe   Ni
----------------------------------------------------------------------
metal          9.23  10.67 0.02 2.49 0.05 0.43 0.16 0.13 7.15 66.60 3.09
couche         5.53 61.46 0.03 0.71 0.08 0.30 0.40 0.02 2.48 28.37 0.60
couche bis     9.24 57.52 1.37 0.47 0.04 4.46 0.03 0.42 1.96 23.99 0.48
```

Figure 3.38: EDX analysis of the microstructure of the sample *Immersion 0h/week* close to the hole

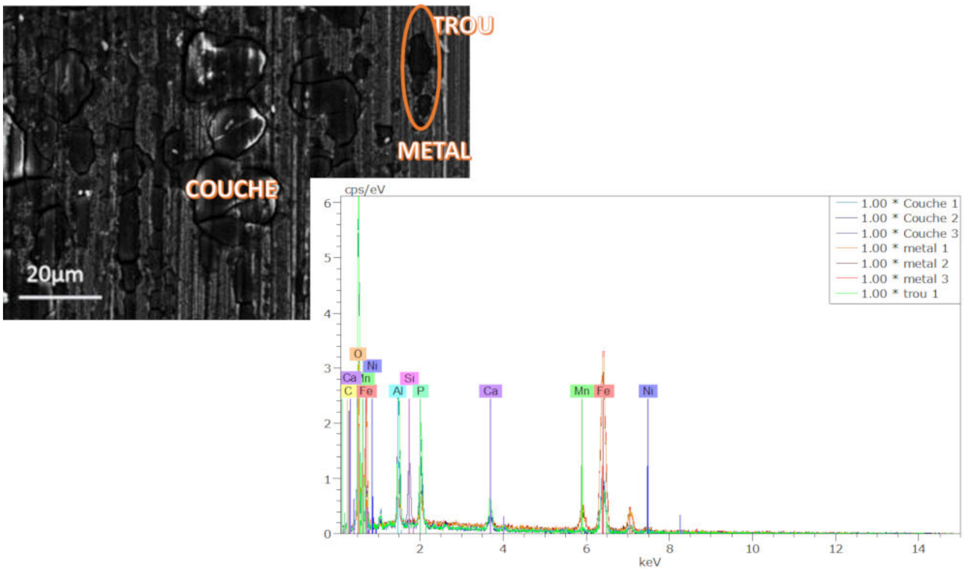

```
Atomic percent (%)

Spectrum        C     O   Al   Si    P   Ca   Mn    Fe   Ni
-----------------------------------------------------------
Couche      14.61 60.35 5.89 1.39 3.83 1.57 0.41 33.71 0.69
metal       12.21 32.54 3.57 0.01 2.04 0.83 4.32 42.91 1.61
trou        11.94 63.57 5.64 0.04 5.19 2.75 0.74  9.55 0.58
```

Figure 3.39: EDX analysis of the microstructure of the sample *Immersion 0h/week* close to the edge

phosphorus followed by calcium and very small amounts of silicon. Furthermore, the hole named *trou* in this analysis presents the same elements with more or less the same concentration as the cracking deposit layer.

5.2.2 One day immersion

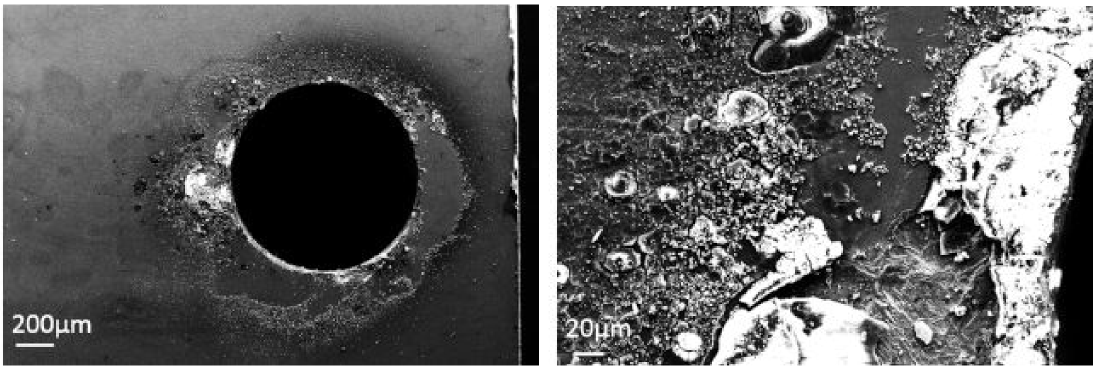

(a) The hole (b) Region near the hole

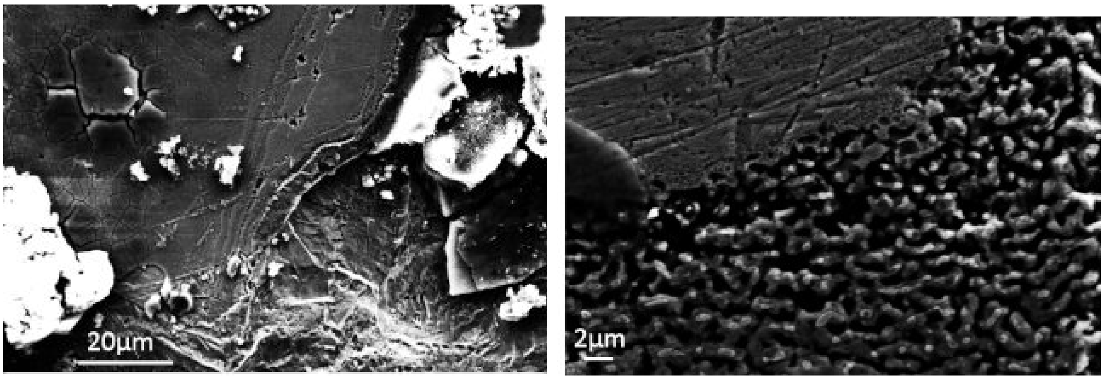

(c) Magnification near the hole (d) Edge of the sample

Figure 3.40: Microstructure of the sample *Immersion 0h/day*

The microstructures of the samples immersed for one day are presented on Figures 3.40, 3.41 and 3.42. The morphological changes for the faces of the samples polished up to the OPS can be summarised as:

- **The hole** Again, a very large region around the hole is attacked. Deposited layers as well as corrosion products can be highlighted. In addition, the microstructure of the metal can be distinguished below the cracking layers. Moreover, in the metal layers, some cracks can be observed as well (as in Figure 3.41d and 3.42d). On the other hand the sample *Immersion 0h/day* presents some pits near the hole. Again, the other regions of the sample were not similarly attacked.
- **The edges** The sample *Immersion 0h/day* presents on one of its edge a characteristic morphology composed of films as in Figure 3.40d. The other edges do present pits as in the sample *Immersion 24h/day* with corrosion products deposit.

On the other hand, by looking at the morphology of the samples polished up to 1200 SiC as in Figures 3.41f and 3.41g, no large cracks or cracking deposit layers can be distinguished. Only some corrosion products can be highlighted below the hole.

In addition, EDX analysis has been performed near the hole and the edge. Again, only a qualitative analysis can be done since the corrosion layers are very thin. From Figure 3.43, it can

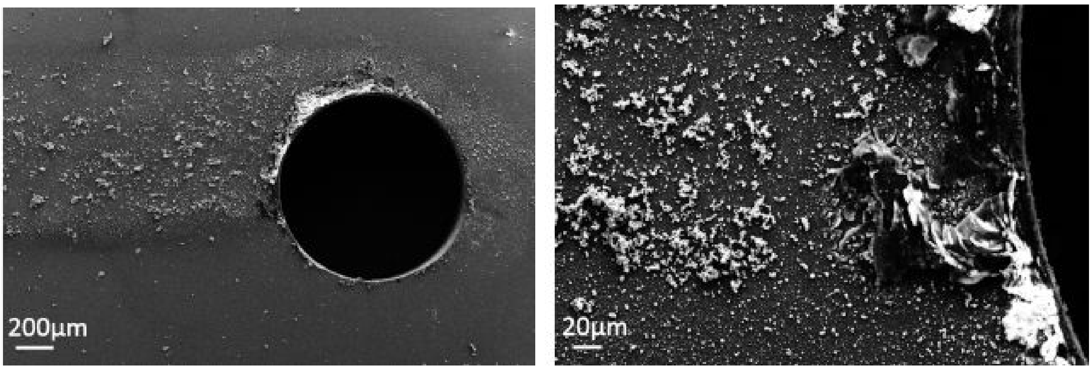

(a) The hole

(b) Region near the hole

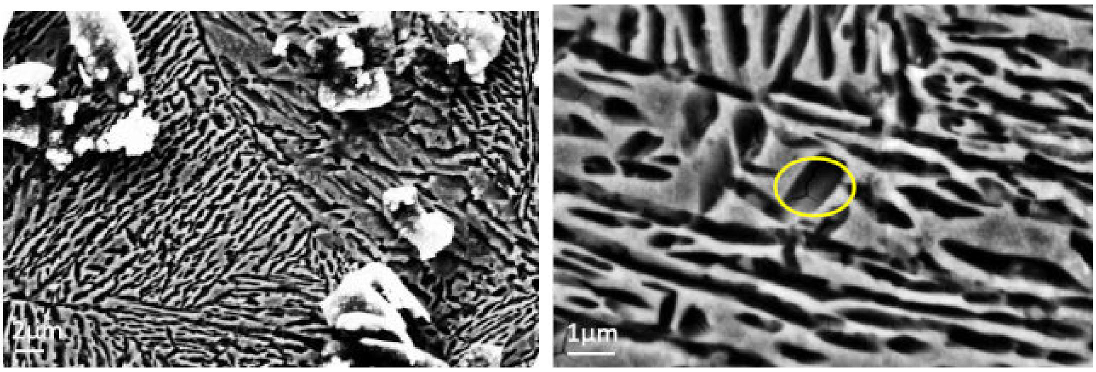

(c) Magnification below the hole

(d) Magnification below the hole

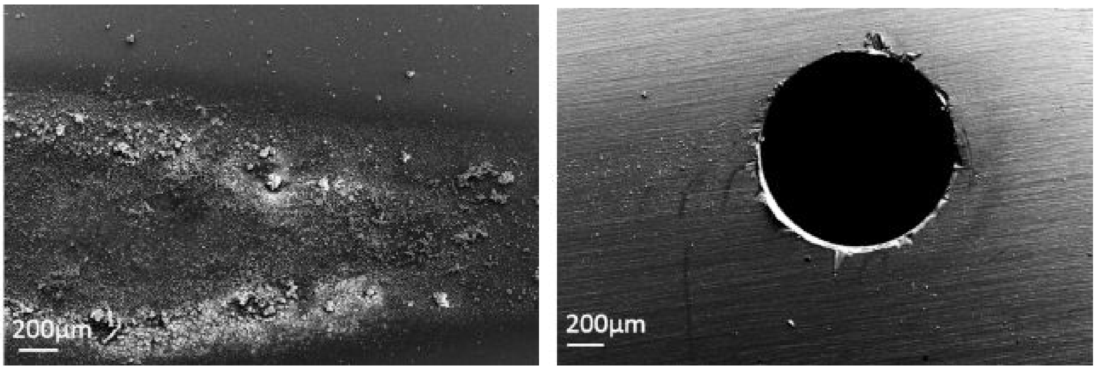

(e) Below the hole

(f) The hole - 1200 SiC polishing

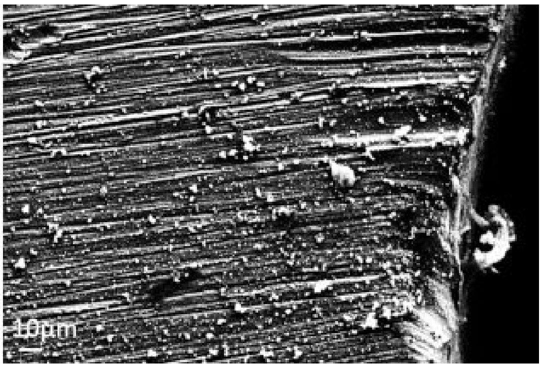

(g) Below the hole - 1200 SiC polishing

Figure 3.41: Microstructure of the sample *Immersion 8h/day*

be highlighted that the *Layer 1* presents large amounts of oxygen followed by iron and carbon as well as small amounts of the alloying elements. It has low amounts of phosphorus followed by calcium and chlorine. In addition, the *Layer 2* shows as well high oxygen content followed

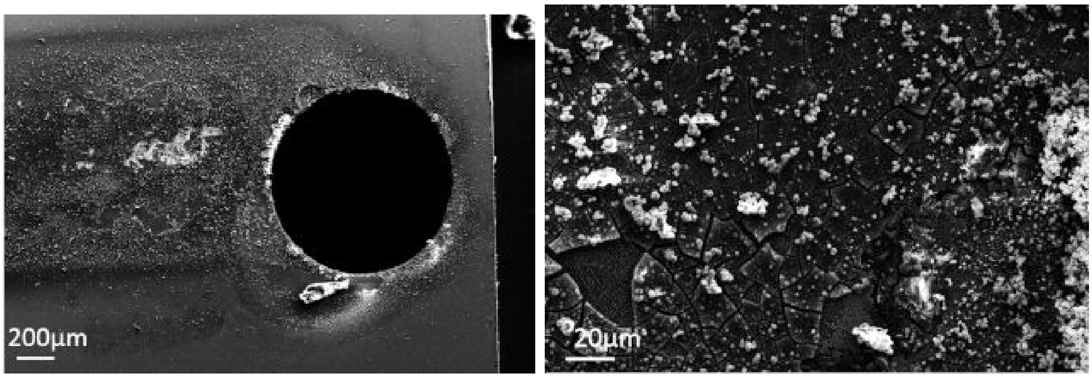

(a) The hole (b) Below the hole

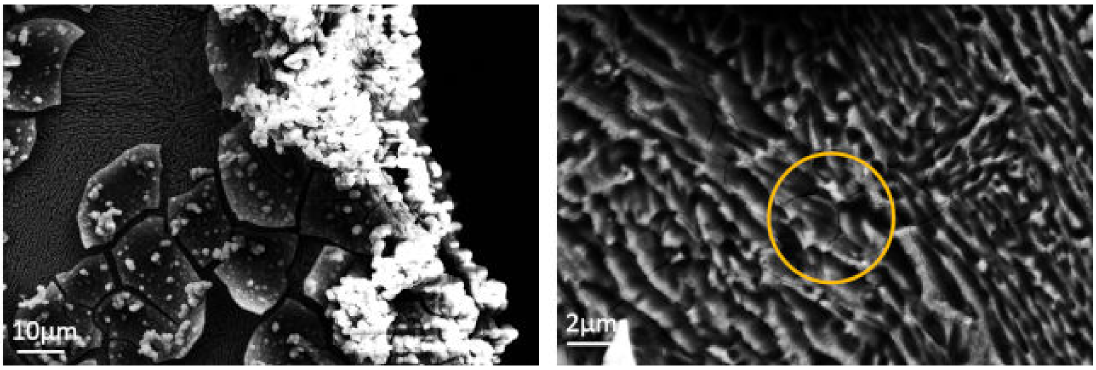

(c) Magnification below the hole (d) Magnification below the hole

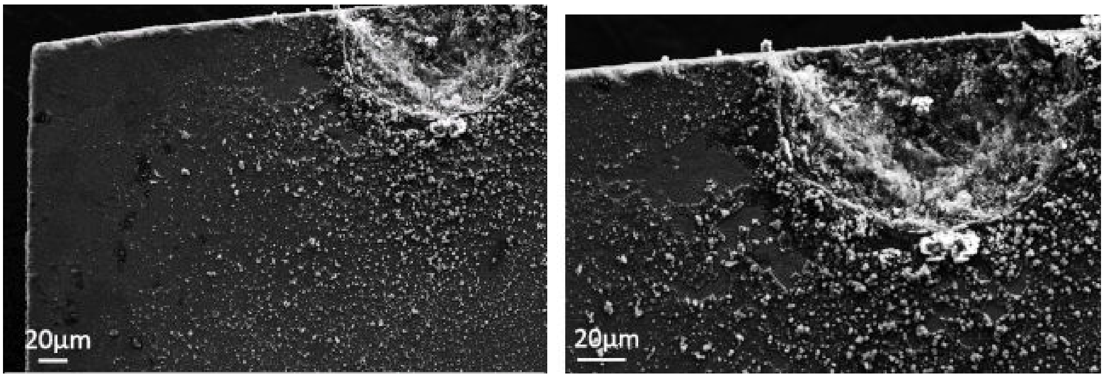

(e) Edge of the sample (f) Magnification at the edge of the sample

Figure 3.42: Microstructure of the sample *Immersion 24h/day*

by iron and carbon. It presents as well low contents of phosphorus, magnesium and chlorine. Moreover, the *Layer 3* presents a higher content in iron and low amounts of oxygen and carbon as well as higher alloying content compared to the previous layers. Furthermore, *White balls* have a very high content in oxygen and small amounts of iron and carbon. It presents as well very low content of phosphorus, calcium and sodium.

From Figure 3.44, it can be highlighted that the *underneath metal* presents a high content of iron and alloying elements and a very small content of carbon. It should be noted that the oxygen content has not been taken into account in this analysis. The *white balls* have a high contents of iron followed by carbon and high alloying elements contents as well. It shows as well non-negligible content of phosphorus followed by calcium and sodium. Furthermore, the *corroded layer* presents a high content in carbon followed by iron. There are as well non-negligible amounts of calcium, phosphorus and sodium.

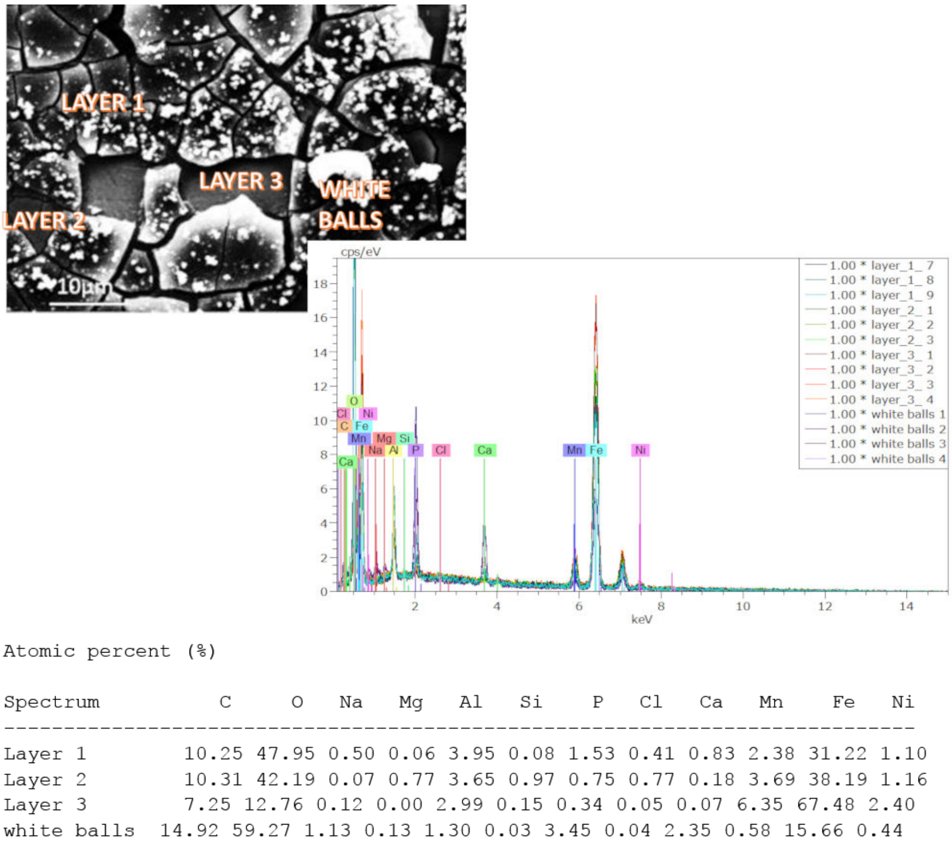

```
Atomic percent (%)

Spectrum          C     O    Na    Mg    Al    Si    P    Cl    Ca    Mn    Fe    Ni
---------------------------------------------------------------------------------------
Layer 1        10.25 47.95 0.50 0.06 3.95 0.08 1.53 0.41 0.83 2.38 31.22 1.10
Layer 2        10.31 42.19 0.07 0.77 3.65 0.97 0.75 0.77 0.18 3.69 38.19 1.16
Layer 3         7.25 12.76 0.12 0.00 2.99 0.15 0.34 0.05 0.07 6.35 67.48 2.40
white balls   14.92 59.27 1.13 0.13 1.30 0.03 3.45 0.04 2.35 0.58 15.66 0.44
```

Figure 3.43: EDX analysis of the microstructure of the sample *Immersion 0h/day* close to the hole

5.2.3 One hour immersion

Figures 3.45 and 3.46 show the microstructure of the samples immersed for one hour. The morphological changes on the faces of the samples polished up to OPS can be summarised as:

- **The hole** On the opposite of the previous samples, the hole only presents some corrosion products but no cracking layers deposit can be noticed. In addition, as well as for the other samples polished up to the OPS, the microstructure of the sample can be highlighted below the attacked layers. Moreover, the sample *Immersion 8h/1h* presents specific aggregates below the hole (see Figure 3.46c).

- **The edge** On the sample *Immersion 0h/1h* some pits can be distinguished and cracking deposits layers around those pits (see Figure 3.45b). For the sample *Immersion 8h/1h*, a very large crack was highlighted on one edge (see Figure 3.46a) whereas the other edges reveal small pits with no cracking deposit layer around.

A EDX analysis has been performed on the region close to the edge and close to the hole. It should be noted that the presence of oxygen has not been analysed in these analysis. From the analysis of the edge of the sample, presented in Figure 3.47, it has been observed that there are large amounts of iron and of alloying elements. There are also very small amounts of carbon. This is true for both the crack left and right. Hence, this crack could be related to the initial metal and non due to the corrosion mechanism.

From Figure 3.48, it has been highlighted that the large dark area and the aggregates correspond to the underneath metal. Hence, they present large amounts of iron and of alloying

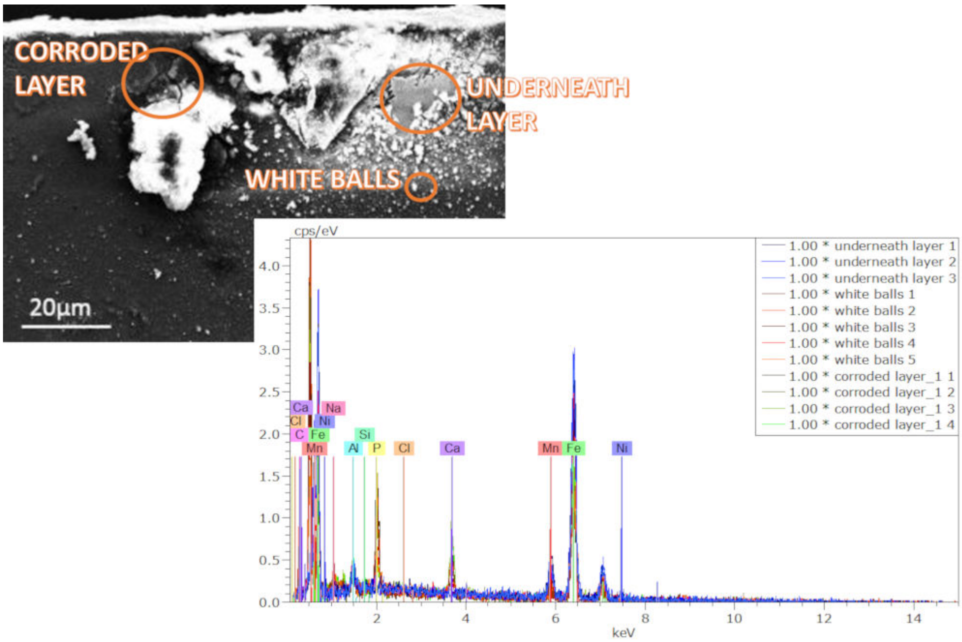

```
Atomic percent (%)

Spectrum                C    Na    Al    Si      P    Cl    Ca    Mn     Fe    Ni
-------------------------------------------------------------------------
underneath layer      8.63 0.67 2.54 0.13  0.15 0.13 0.04 8.18 76.69 2.86
white balls          37.15 1.75 1.4  0.05  4.75 0.24 2.72  3.63 47.02 1.29
corroded layer       42.35 2.94 1.90 0.23 4.93 0.26 5.70  2.63 38.15 0.90
```

Figure 3.44: EDX analysis of the microstructure of the sample *Immersion 24h/day* close to the edge

elements. There are as well small contents of carbon. On the other hand, the *White balls* present large amounts of iron as well as a non-negligible amount of carbon. There are as well low amounts of calcium and sodium.

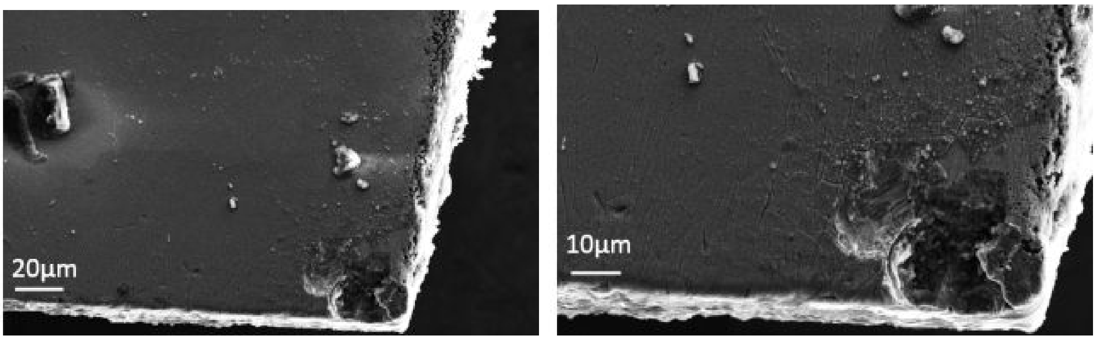

(a) Edge of the sample (b) Magnification at the edge of the sample

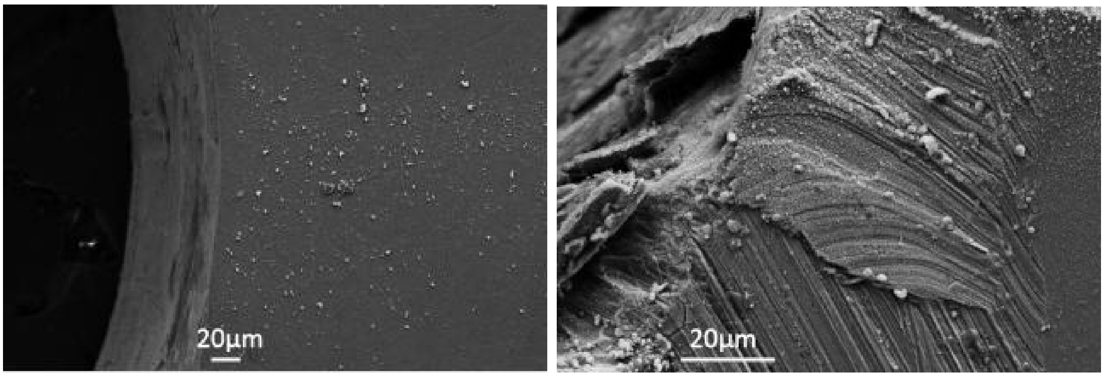

(c) Below the hole (d) Magnification below the hole

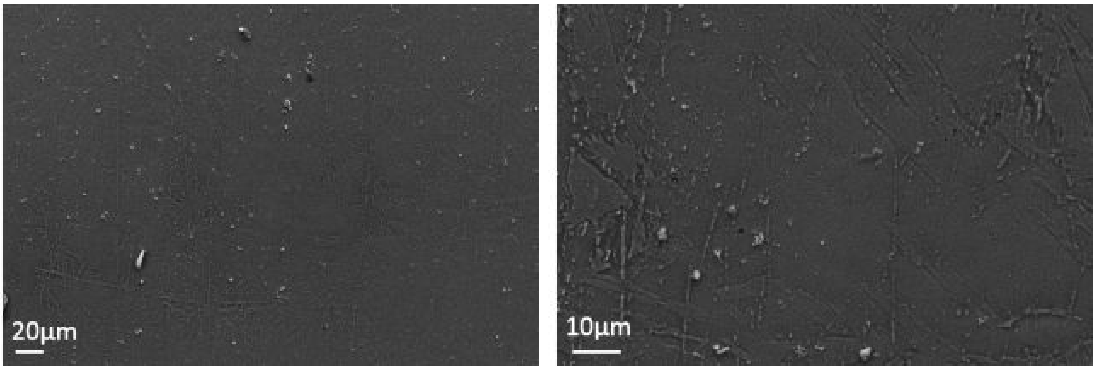

(e) Magnification below the hole (f) Magnification below the hole

Figure 3.45: Microstructure of the sample *Immersion 0h/1h*

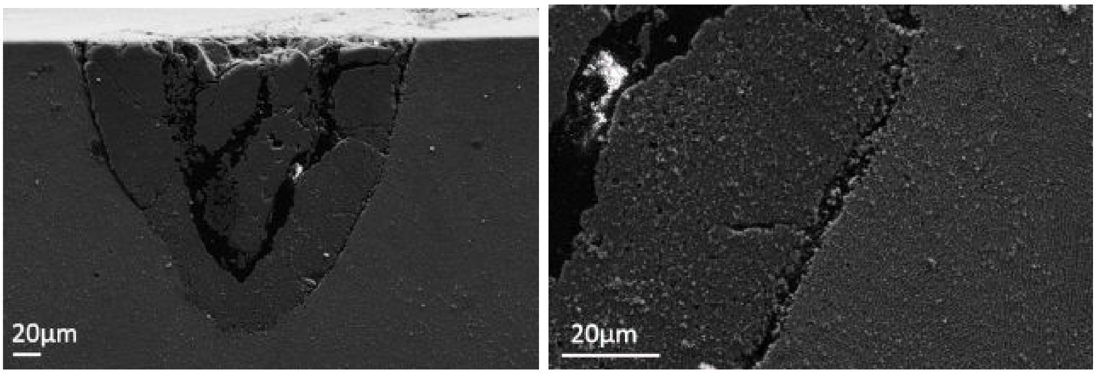

(a) Edge (b) Magnification at the edge

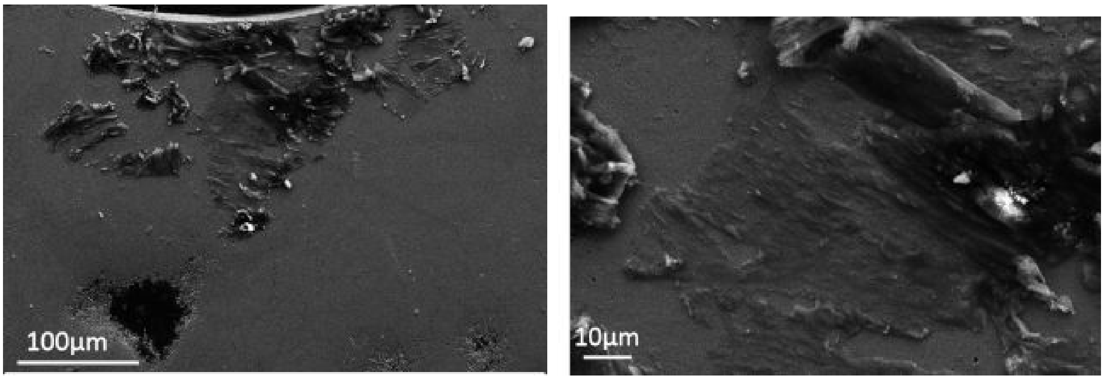

(c) Region near the hole (d) Magnification near the hole

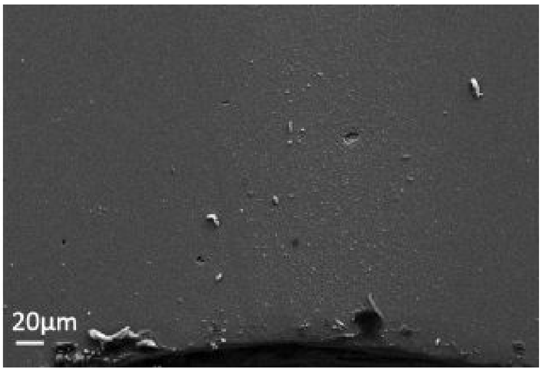

(e) Region below the hole

Figure 3.46: Microstructure of the sample *Immersion 8h/1h*

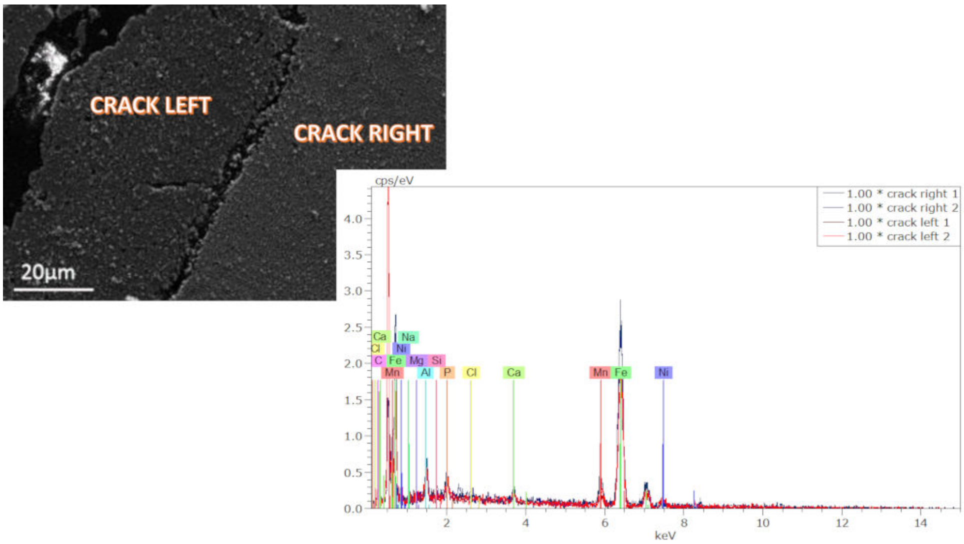

```
Norm. mass percent (%)

Spectrum          C    Na    Mg    Al    Si     P    Cl    Ca    Mn     Fe    Ni
----------------------------------------------------------------------
crack right   6.99 0.61 0.04 2.11 0.22 1.15 0.07 0.93 7.72 78.18 1.95
crack left    6.89 0.61 0.59 4.69 0.07 2.39    0  0.86 5.14 74.69 7.58
```

Figure 3.47: EDX analysis of the microstructure of the sample *Immersion 8h/1h* close to the edge

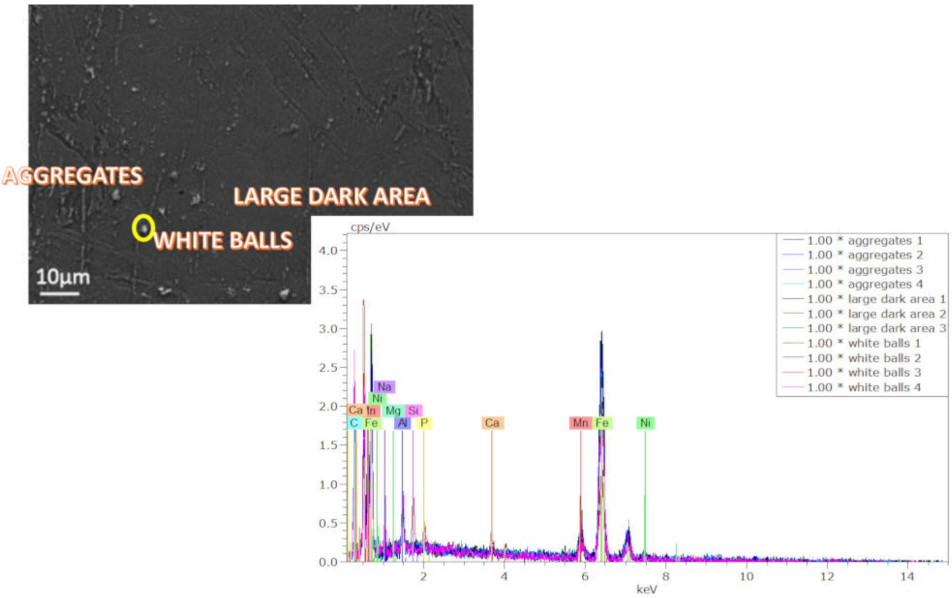

```
Norm. mass percent (%)

Spectrum              C    Na    Mg    Al    Si     P    Ca    Mn     Fe    Ni
----------------------------------------------------------------------
aggregates         4.67 0.32 0.14 2.47 0.03 0.37 0.47 7.49 82.18 1.85
large dark area    3.85 0.05 0.06 1.97 0.00 0.18 0.11 8.66 82.86 2.27
white balls       28.48 1.34 0.18 2.49 0.71 1.00 1.35 5.81 57.17 1.46
```

Figure 3.48: EDX analysis of the microstructure of the sample *Immersion 0h/1h* close to the hole

Chapter 4

Discussion

In this section, the results exposed in the previous Chapter will be analysed and discussed. First, the effect of the heat treatments on the martensite transformation and the austenite reversion will be summarised. Second, a comparison between the experimental results and the Dictra simulations will be detailed. Thereafter, the microstructure of the samples will be further analysed. Third, the metastable properties of the austenite will be discussed. Fourth, the mechanical properties resulting from the heat treatments will be highlighted. Finally, the corrosion behaviour of each samples will be characterised.

1 Austenite reversion

As a result of the different heat treatments performed thanks to the dilatometer or the furnaces, different properties of the austenite reversion and martensite transformation have been observed in the previous chapter.

1.1 XRD analysis

First, from the XRD analysis, it can be highlighted that the austenite fraction increases when the time of the annealing at $600°C$ increases. In addition, this observation is verified with samples from the furnaces except when a plateau of 48h is performed. Moreover, this increase of the austenite fraction with the increase of the annealing time is in agreement with the the observation of Wang et al.[67] and Escobar et al.[94]

Furthermore, for the same heat treatments performed, the volume fraction of austenite calculated is lower than the one in the work of Wang. Moreover, it should be noticed that the background noise increases with the 2θ angle in the diffraction pattern. Hence, it could cause the modification of the peak intensity at small angles and lead to certain errors of the results.

In addition, in the work of Lee et al. [95], it has been demonstrated that the experimentally measured austenite volume fraction for the same annealing temperature but for different holding times is not the same. Hence, they concluded that for longer annealing time, the austenite volume fraction experimentally measured corresponds to the equilibrium austenite volume fraction. On the other hand, for shorter annealing time, the equilibrium cannot be reached, hence, the lower volume fraction measured. Moreover, for a Fe-0.3C-6Mn (in mass pct) TRIP steel, they found an austenite volume fraction of 17% and 28% for an annealing at $600°C$ for 1 hour and 24 hours respectively.

Moreover, when the temperature as well as the time of the homogenization at $1100°C$ are decreased, the austenite fraction largely decreases. Normally, at the homogenization temperature of $1100°C$, the sample is fully austenitized. Specifically, since the different impurity elements of the alloy will be segregated at the grain boundary, the alloy needs to be heated to very a high temperature at which the mobility of the substitutional alloying elements is high and a homogeneous austenite composition is obtained. [96]

Hence, since the temperature as well as the time of the homogenization is decreased, the austenitization and the homogenization of the microstructure may be not completed. As a results of this decrease of time and temperature of the homogenization, they might be a non-uniform chemical composition as well as the presence of impurity at the grain boundary that could slow the reversion into austenite.

In addition, when a thermal cycling is performed before the annealing, the same order of magnitude of austenite fraction as the one resulting from a homogenization followed by the same annealing treatment. Indeed, in a thermal cycling, there is an increase of the mobility of the grain boundaries due to the extra thermal excitation available. [97] [98] Hence, there is a decrease of the effective activation energy for the grain growth and an increase of the recrystallisation response[1]. As a result of this activation and increase of the recrystallisation, the reversion of austenite during the annealing will be faster as it has been noted on the graph of the extension versus the time at $600°C$ (see Figure 3.19).

Furthermore, when only very short plateaus around $750°C$ are performed, the austenite fraction is very low. Indeed, only thermal cycles have been performed. As a result, even if the thermal cycling increases the thermal excitation available and the recrystallisation, an annealing after the martensite transformation is still needed to have the reversion of martensite into austenite.

1.2 Extension of the samples

First, from the graphs of the extension versus the temperature, some general trends can be highlighted. There is an extension of the sample during the heating whereas there is a contraction of the sample during the cooling and the plateaus.

As a matter of fact, at the beginning, the sample is constituted of a ferrite phase. Then, upon heating, there is an expansion according to the heat expansion behaviour of the ferrite. Thereafter, a small bump is present before the first transformation that corresponds to the cementite decomposition. Subsequently, the first transformation, from ferrite (a BBC phase) into austenite (a FCC phase), causes a contraction due to the smaller specific volume of austenite. This transformation always occurs around $650 - 700°C$. This range of temperatures is slightly lower than the one given by the phase diagram of the iron and carbon. Hence, this difference can be explained by the presence of the gammagenic elements (nickel, manganese and carbon) in the alloy which decreases the transformation temperatures of the austenite.[99] Moreover, this range of temperature is in agreement with the literature of other TRIP steels. Then, there is a contraction during the homogenization at $1100°C$. Indeed, during the homogenization, the sample is fully austenitized and, consequently, it will follow the heat expansion behavior of the austenite at $1100°C$. [95]

Upon cooling, there is still a contraction since it follows the heat expansion of the austenite. Then, when the M_S temperature is reached, the martensitic transformation takes place. Specifically, since this transformation is a displacive transformation it will take place through atomic movements. Hence, there is an expansion due to the higher specific volume of the martensite. Indeed, the martensite has a lower density than austenite.

During the heating, there is an expansion due to the heat expansion behavior of the martensite. When the annealing plateau at $600°C$ is reached, there is a partial reversion of the martensite into austenite. This isothermal transformation causes a contraction due to the lower specific volume of austenite. Furthermore, from the literature, it can be found that the reversion of

---

[1] The recrystallisation consists in the replacement of deformed grains by a new set of non-deformed grains that nucleate and growth until the originates grains have been entirely consumed. [97] [98]

α' martensite to γ austenite occurs around $600°C$ for other TRIP steels. [94] In addition, this reversion occurs by nucleation and diffusion-controlled growth. [95]

Moreover, in the work of Lee et al. [100], they investigated the mechanism behind this reversion transformation into austenite. They demonstrated that this transformation occurs first diffusionlessly during the continuous heating and then it proceeds in diffusive nucleation and growth manner during the isothermal holding. Specifically, during the heating, the martensite transformed to austenite without atomic diffusion. When the plateau at $600°C$ is maintained, the diffusionless transformation stops and it is the diffusive reverse transformation that immediately starts. Furthermore, they observed that the temperatures range for this reverse transformations were independent from the heating rate.

In addition, during the cooling after the annealing at $600°C$ no further transformations occur.[101] Contrary to the other cooling which correspond to quenching, the cooling after the annealing corresponds to a slower cooling. Since a slower cooling is performed, the elements including the carbon have more time to diffuse. Hence, the formation of martensite is not possible during the cooling after the annealing at $600°C$ since the martensite formation is a diffusionless transformation. [102]

Second, from the graph of the extension versus the time for the homogenization (at $1100°C$), it can be highlighted that the time of the plateau does not change the curves. On the opposite, different parameters change the behaviour of the curves during the annealing at $600°C$. Hence, those different behaviours represent the austenite reversion in each sample.

As previously indicated, the curve of the sample on which a thermal cycling has been performed is outside all the other curves. As a result, the thermal cycling leads to the fastest transformation in austenite thanks to its thermal activation. On the opposite, the sample on which an annealing of 8 hours has been performed is the slowest one. Hence, this is in agreement with the previous observations.

Thereafter, decreasing the time and the temperature of the homogenization at $1100°C$ causes a slowest and smallest transformation into austenite. As stated previously, a shorter and lower temperature homogenization causes a decrease of the austenite reversion. Hence, this lower reversion may come from the uncompleted homogenization.

1.3 Comparison between the experimental and numerical results

By comparing the experimental and the numerical results the same conclusions have to be drawn. From the simulations it has been observed that increasing the time of the annealing at $600°C$ causes an increase in the austenite transformation. In addition, the austenite phase has a higher weight fraction of manganese, nickel and carbon than the martensite phase since those elements are gammagenetic. The opposite is true for aluminum, which is an alphagenic element.

Moreover, as well as the results of Wang et al. [67], when the annealing time is increased, the austenite grains continue to grow and maintain the same chemical composition as the one for an annealing time of 1 hour.

Furthermore, from the three simulations performed, it can be distinguished that the presence of carbon increases the reversion into austenite while the presence of aluminum decreases the reversion compared to the simulation where none of carbon or aluminum is present. Hence, as well as for the transformation of ferrite into martensite, in the martensite to austenite reversion, the gammagenic elements will stabilise the austenitic phase and favors the transformation into austenite whereas the opposite is true for the alphagenic elements.

Finally, it can be concluded that increasing the holding time of the annealing treatment at $600°C$ increases the volume fraction austenite but a saturation can be highlighted around 48 hours. As a result, the equilibrium volume fraction of austenite is reached for an annealing of 24 hours. In addition, the thermal cycling increases the recrystallisation and the number of active sites thanks to the extra thermal excitation. Hence, the thermal cycling leads to a fastest conversion of the same order of magnitude as the one resulting from a homogenization followed by the same annealing treatment. Furthermore, decreasing the temperature and the time of the homogenization slows down the reversion.

1.4 Resulting microstructure

Thanks to the heat treatments performed on the samples, different microstructures were obtained.

As a general trend it can be highlighted that all the samples present more or less the same microstructure except for the samples treated thanks to thermal cycles. Hence, all the samples present a microstructure constituted of grains with austenite and martensite which is close to the microstructure obtained in the work of Wang et al. [67] As a matter of fact, the retained austenite grows along the prior austenite grain and the α' martensite block or laths.

On the other hand, it can be highlighted that increasing the time of the annealing at $600°C$ causes an increase of the austenite grains. Hence, as well as in the work of Wang et al. [67], the retained austenite grains grow after an annealing of 1 hour and continue to grow with further annealing leading to a quasi-continuous network near the martensite boundaries with limited gaps in between. In addition, it should be noted that there is a large range of grain size presents in each sample as well as in the work of Wang et al.[67].

Furthermore, Lee et al. [100] studied in details this reversion transformation. They demonstrated that during the continuous heating, the reversion transformation into austenite occurs without atomic diffusion. Hence, it gives a lath-shaped austenite with a high dislocation density. Thereafter, when the sample is maintained at the temperature, the transformation occurs immediately by diffusive reverse transformation. As a result of this diffusive transformation, the microstructure consists in an equiaxed austenite grains with low dislocation density. In addition, when the holding time of the plateau is increased, the new equiaxed grains are nucleated and grow whereas the diffusionlessy formed austenite laths are recovered and subdivided into several sub-grains with low-angle boundary.

On the other hand, the samples treated with thermal cycles reveal a finer microstructure. Hence, thanks to rapid heating and cooling between the martensite and austenite phase, the size of the austenite and the block or lath of the martensite decreases. This observation is in agreement with previous work such as the one of Santofimia et al.[103]

Moreover, sample on which no annealing treatment has been performed (as in *Dilato 1h*) presents a fully martensitic microstructure with no austenite grains. Hence, this microstructure is a typical martensitic microstructure and is in agreement with the initial microstructure of the work of Wang et al.[67]

In addition, from the analysis of the microstructure of the sample *Dilato electropoli* that represent the microstructure of the thickness of the sample, only porosity at the edge of the sample can be noted. Hence, there are lots of porosity at the surface whereas there are few porosity in the thickness of the alloy. As a reminder, the alloy was produced by casting and then a hot and a cold rolling was performed. From the casting step, a lot of defects including porosity can be created. Thereafter, thanks to the rolling steps, some porosity can be closed but some residues can still be present.

Finally, it can be summarised that the microstructure of the sample after a homogenization at $1100°C$ and a further annealing at $600°C$ reveals martensite grains along which austenite grains grow. Moreover, increasing the time of annealing decreases the fraction of martensite whereas it increases the growth of austenite grains. Specifically, the retained austenite grows along the prior austenite grain and the α' martensite block or laths. On the other hand, if thermal cycles are performed on the sample before the annealing, the final microstructure is finer and composed as well of martensite and austenite grains.

1.5 Thermal expansion coefficients and martensite transformation

First, the thermal expansion coefficients have been calculated for the ferrite and the austenite phases. For the thermal expansion coefficients of the ferrite, no important changes can be noticed. On the other hand, the thermal expansion coefficient of the austenite is higher than the one of the ferrite except when a thermal cycling is perfomed. It should be noted that since the two first plateaus performed in the thermal cycles were very short, the slope of the tangent to the curve in the graph was very short as well. Hence, this limited number of results for the calculation could lead to some errors.

In addition, the thermal expansion coefficients α_{a1}, α_{a2} and α_{a3} do not represent the thermal expansion coefficients of the austenite alone. Specifically, for α_{a2} (or α_{a3} in the case of a thermal cycle), it should be noted that it is calculated after the annealing at $600°C$. Hence, after the annealing martensite and austenite are present. Since the thermal expansion coefficient of the martensite is lower [104], the α_{a2} and α_{a3} in the case of a thermal cycle will be lower than the α_{a1} which is linked to a fully austenize sample in most of the samples. Moreover, it is known that the thermal expansion coefficients depend on the temperature and their values globally increase with the temperature. [104]

Furthermore, the thermal expansion coefficients linked with samples on which a thermal cycle has been performed are very low. As explained previously, due to the short plateau performed, the limited number of results for the calculation could lead to some errors. Furthermore, in the work of Kumar et al.[105], they explained the presence of a transient behavior due to the functionning of the dilatometer itself. Specifically, the thermocouple inside the dilatometer does not touch the sample, it is just placed above it. Hence, the temperature recorded by the thermocouple increase as a function of the heat supplied by the furnace when the resistance of the furnace is turned on. Normally, the sample temperature is equal to the thermocouple temperature when the steady state is reached but the sample takes some time to homogenise the temperature. As a result, there will be a transient stage until this steady state is reached. The thermal expansion coefficient calculated in this transient stage will be lower than the true value. This transient stage could explain the lower values obtained for the samples on which a thermal cycling has been performed.

On the other hand, from the literature it is known that the absolute values of the thermal expansion coefficients are higher for austenitic structure than for ferritic structure. Hence, the change of slope of the linear coefficient of expansion during the transformation from ferrite to austenite. In addition, the values found during the dilatometry tests are in concordance with the mean values found in the literature: 14.5 $10^{-6}K^{-1}$ for the ferrite and 23 $10^{-6}K^{-1}$ for the austenite.[104]

Second, during the martensitic transformation, it can be noticed that for the same heat treatment performed, the samples will not present the same M_S and M_f. Those differences could come from the experimental errors in the calculations. In addition, no true difference could be distinguished between the martensitic temperatures from the different heat treatments except when a thermal cycling is performed.

In addition, the thermal cycling decreases a lot the M_S and M_f temperatures. The martensite start temperature depends on the alloying elements present in the alloy as well as the thermomecanic history of the alloys. Furthermore, this observation is in agreement with the observation of Lee et al.[95] and Santofimia et al.[103] who observed a decrease of the M_S temperature when increasing the number of thermal cycles due to the strengthening of the austenite in Fe-Mn and Fe-C-Si alloys respectively.

Moreover, in the work of Santofimia et al.[103] it has been reported that the prior grain austenite size reduction decreases the M_S temperature. This reduction comes from the refinement of the prior austenite grain size. The qualitative explanations of these observations are still unclear but most of them are based on the strengthening of the austenite as the prior grain size is reduced. In addition, the strengthening of the austenite is still not well understood. On the other hand, they highlighted that this reduction of the prior austenite grain size is more effective during the first cycles.

Finally, it can be concluded that the thermal expansion coefficients of the ferrite is smaller than the one of the austenite. In addition, the thermal expansion coefficients of the austenite increases with the temperature. Moreover, the thermal expansion coefficient after the annealing treatment reflects the presence of marteniste and austenite. On the other hand, thermal cycling decreases the M_S temperatures due to the strengthening of the austenite.

1.6 Metastable austenite

Two scannings have been performed with the EDX: one inside the square delimited by the four indents and one inside a grain in the square. It has been determined that there were more fluctuations in the scanning performed in the square than the one in the grain.

Since the resolution of the EDX is of $1 \mu m$ and the scanning that has been performed are in the range of $20 - 4 \mu m$, no true phase segragation could be highlighted. Hence, an other analysis with a transmission electron microscope in the STEM mode should be performed in order to get a mapping on each point to highlight a phase segregation.

2 Mechanical properties

As a result of the four different heat treatments performed on the tensile specimens various mechanical properties have been obtained.

First, the fully martensitic sample, *Specimen 0h*, presents the largest yield strength. Since it is a fully martensitic sample, it is, by definition, a brittle material. Hence, the specimen reaches the highest stress but it reaches the smallest elongation at the fracture point.

Second, the specimens that were further annealed exhibit a lower yield strength than the fully martensitic sample. Whereas the martensitic sample is a brittle material, the other specimens behave as ductile material. Hence, they reach a higher elongation at the fracture point.

Moreover, it can be highlighted that when the time of the annealing increases the yield strength slightly increases and the elongation at the fracture point is increased as well except for an annealing time of 48 hours. Furthermore, all the results are much lower than the one obtained in the work of Wang et al. [67] even for the same heat treatments. From the XRD results it has been highlighted that the austenite volume fraction is lower than the one obtained for the same heat treatments in the work of Wang et al. Hence, this lower fraction of retained austenite explained the lower curves obtained in the mechanical tests.

On the other hand, when the specimens are deformed they will follow the same transformation as the one described in the work of Wang et al.[67] Specifically, at the beginning, in the undeformed state, the grains of retained austenite have a low density of staking fault and they will exhibit an uniform in-grain orientation. After the deformation has been applied, the retained austenite grains are plastically deformed before the transformation. Hence, those grains will accumulate partial dislocations and regular arrays of staking fault. Thereafter, when the deformation is increased, a multiplication of the staking fault occurs. As a result, the faults can create a bcc related structure in which the atoms can shift into bcc positions through a second shear mechanism.

Consequently, it is the configuration where the staking fault intersect each other that can act as a potential nuclei for the transformation into α' martensite. Hence, it has been demonstrated in the work of Wang et al.[67] that this transformation is an athermal mechanism since the α' martensite formed during the transformation inherits the staking faults of the retained austenite grains.

Thanks to this transformation into α' martensite, and more specifically, to the development of in-grain deformation substructures that stabilizes the larger grain, a higher overall mechanical stability is observed.

On the other hand, the general mechanical properties achieved present lower engineering strain at fracture than the typical TRIP-maraging steels (about 10-30%).[54] This reduction of the properties could come from the lower retained austenite fraction as well as the state of the specimen before the tensile tests. Only a simple polishing with silicon carbide paper has been performed. Thereafter, a layer of oxide was still present on the sample surface and there was small variation in the thickness of the sample. From the literature, it is known that the surface roughness affects mainly the fatigue life but there is no significant effect on the strength and ductility properties. Specifically, the surface roughness effect on the mechanical properties is only important when the size of the material is miniaturized. [106] Hence, the difference in the mecahnical properties achieved in this work could be linked with the geometry of the specimen.

In addition, thanks to the results of the evolution of the retained austenite fraction and the ϵ-martensite fraction during the tensile of the work of Wang et al.[67] on the same TRIP-maraging alloy, it can be distinguished that the fraction of retained austenite decreases drastically at the early stage of deformation. Hence, the stability of the austenite present in this TRIP-maraging steel is quite low. As a result, the polishing with the SiC paper could have decreased the content of retained austenite and consequently decreased the overall mechanical properties.

Finally, it can be summarised that the fully martensitic sample is very brittle and hard at the same time whereas the samples further thermally treated are ductile. Hence, increasing the time of the annealing increases the yield strength and the general mechanical properties thanks to the higher content of retained austenite. In addition, a saturation in the improvements of the mechanical properties can be noticed after 24 hours.

3 Corrosion properties

In order to characterise the corrosion properties of the TRIP-maraging steel studied, several immersion tests differing by their time of immersion and their heat treatments have been implemented. The general trends will be presented in this section. In addition, it should be noted that the trends highlighted below reflect the behaviour of the immersion tests performed. Since only one immersion test has been performed for each time of immersion, the trends highlighted should be taken carefully.

3.1 Corrosion rates

Thanks to the immersion tests performed, it can be highlighted that the corrosion rates associated with an immersion time of 1 hour are much larger than the one for 1 or 7 days. This observation is in agreement with the literature: the corrosion rate is higher at the beginning of the immersion and then the corrosion rate for longer immersion time decreases. [107] This observation could be explained by the formation of a passive layer on the metal surface. The passive layer formed with the corrosion products deposited on the metal surface. Hence, this film slows down the corrosion mechanisms since the oxide formed on the surface is insoluble. [108]

Furthermore, a global decrease of the rates can be noticed when the annealing at $600°C$ is lengthened except for an immersion of 1h and 1 day in the case of an annealing of 0 and 8 hours. Hence, the corrosion rate decreases when the content of austenite is increased. This observation is in agreement with the work of Handoko et al.[109] on the effect of the retained austenite stability on the corrosion mechanism of dual phase high carbon steel. As a matter of fact, they demonstrated that when the volume percentage of the retained austenite increases, its stability is improved. As a result, it minimized the internal energy between the martensite-austenite grain boundary interfaces and it lowered the propensity on a corrosion attack. Consequently, an increase of the volume percentage of the retained austenite causes a decrease of the corrosion rate. Hence, a lower martensitic volume improves the corrosion resistance properties.

In addition, in the work of Talapatra et al.[110], they found that high energy regions did prone the corrosion. Hence, the microstructure having finer grains has a lower corrosion resistance. Moreover, the microstructure that contains low transformation products as the bainite or the martensite has as well a lower corrosion resistance.

Moreover, from the released ions solution ratios calculated some general trends have been noted. First, by comparing the ratios for an immersion of an hour, it can be highlighted that the aluminum will be the most dissolved element. Since the released ions solution ratios $\frac{Fe}{Al}$ are smaller than the corresponding solid ratios, there will be more aluminum in the solution. The elements can be classified as $Al > Mn > Fe > Ni$. Hence, nickel is the less dissolved element.

Second, by comparing the ratios for an immersion of one day, it can be noted that aluminum will be the most dissolved element. Specifically, the elements can be classified as $Al > Mn > Fe > Ni$. Consequently, nickel is again the less dissolved element.

Third, by comparing the ratios for an immersion of a week, it can be highlighted that manganese will be the element that has been the most dissolved. Since the ionic ratios $\frac{Fe}{Mn}$ are smaller than the corresponding solid ratios, there will be more manganese in the solution. Specifically, the elements can be classified as $Mn > Fe > Ni > Al$. As a result, aluminum is the less dissolved element .

Moreover, in the first stage of the immersion, aluminum and manganese are the most dissolved elements whereas nickel is the less dissolved element. On the other hand, when the immersion time increases, aluminum will be the less dissolved whereas the dissolution of iron and nickel increases. Those differences between the dissolution of the elements could be explained by the different layers of passivation. Indeed, even if the element is not largely dissolved in the solution it does not mean that the element has not been dissolved. Hence, the element can have been dissolved and transformed into an oxide that could form a passive layer. Specifically, the passive layer is a type of oxide that forms a layer of several nanometers thick on the surface of the metals. Moreover, the elements that will passivate do no depend on the metal activity sequence but more on the fact that they belong or not to the noble region of the metal activity sequence.[111]

As a result, from the literature[112], the table of electrochemical potentials of different elements can be found. Thanks to those tables it can be highlighted that nickel and iron are more noble than manganese and aluminum. Hence, during the first stage of the immersion (1 hour and 1 day), nickel and iron will form more preferably oxides compared to aluminum and manganese.

When the time of immersion is increased, the tendency will reverse for aluminum whereas the passivation composed of iron and nickel oxide could be decreased. In addition, by looking at the ionization tendency [111], it can be highlighted that aluminum as well as manganese has a higher tendency to ionise than iron and nickel.

Finally, it can be concluded that the corrosion rates are very high at the beginning of the immersion whereas they decrease for longer time of immersion due to the passivation of the surface. In addition, by increasing the time of the annealing at $600°C$, the corrosion rates globally decrease due to the higher content of austenite. Furthermore, aluminum is the element that dissolves the most at the beginning of the immersion, whereas nickel dissolves the less. Moreover, at the first stage of immersion, there could be a greater tendency to the formation of passivation layers composed of iron and nickel oxide. Moreover, aluminum and manganese have a greater tendency to ionise.

3.2 Resulting microstructure

By comparing all the samples, it can be highlighted that the microstructure of the samples following the immersion tests presents cracking deposit layers, corrosion products and pits in the areas close to the edges, the hole and below the hole. On the opposite, no important changes can be noticed in the other regions of the sample. This behaviour could be explained by the fact that the regions near the edges and the hole are surrounded by a larger volume of solution.

In addition, by comparing the face that has been polished up to 1200 SiC and the face that has been polished up to the OPS for the sample *Immersion 8h/day*, a different behavior can be distinguished. As a matter of fact, the face that has been polished up to the OPS will present cracking deposit layers, pits as well as corrosion products. On the other hand, the face that has been polished up to the 1200 SiC only presents corrosion products. Hence, the polishing steps have an influence on the corrosion behavior of the sample. This behaviour could be explained by the fact that all the samples were not encompassed by the same amount of solution since the immersion tests were static. Moreover, remaining of OPS solution could lead to localised corrosion. In addition, the difference in roughness of the sample surface could as well impact the corrosion resistance.

Moreover, on the face polished up to the OPS, cracks in the microstructure of the metal could be noticed. The cracks in the metal microstructure reveals an attack of the metal.

Furthermore, from the samples immersed 1 hour it can be highlighted that they were mainly attacked on the edges of the sample whereas the region near the hole was slightly attacked. Hence, the corners of the sample are the first area of the sample to be attacked during the immersion. Again, this behaviour could be explained by the fact that the corners are more encompassed with the solution than any other region. As a result, the corners are favourable sites for corrosion.

The samples present different amount of cracking deposit layers, agglomerates of corrosion products and pits. Those differences could be explained by the different volume fraction of retained austenite present as well as the volume fraction of martensite. As stated previously, higher concentration of retained austenite decreases the propensity to corrosion. In addition, the grain size as well as the contact between the electrolyte and metal may have an influence on the behaviour of the metal surfaces.

From the EDX analysis it has been highlighted that the underneath metal was mainly constituted of iron with the presence of oxygen, as well as carbon and the different alloying elements. Moreover, only very small amounts of phosphorus and calcium could be distinguished.

Furthermore, the cracking deposits layers were mainly constituted of oxygen and lower amounts of iron followed by carbon. In addition, only small amounts of alloying elements could be distinguished. There were as well low amounts of phosphorus and calcium.

Furthermore, an analysis of white balls present on the surface has been carried out. It appears that they are mainly constituted of oxygen, iron and carbon. In addition, there are low amounts of phosphorus and calcium.

As a result, the presence of oxides is confirmed by the EDX analysis. Indeed, the different layers do contain large amount of oxygen as well as iron and carbon. On the opposite, the amounts of the alloying elements are low except the content of aluminum which stay at a high level. As a result, one may think that the deposited layers consist mainly of iron oxide. In addition, the presence of carbon could reveal the presence of carbide or more complex components as FeOC. Since the white balls mainly consist of oxygen, iron and carbon, they could represent the deposit of new oxide on the surface. Moreover, since the immersion tests are performed under slightly basic conditions, one of the main iron oxide formed is $Fe(OH)_2$. [71]

On the other hand, the presence of aluminum could be explained by the deposition of the large amount of dissolved aluminum on the surface. Moreover, the higher content of aluminum close to the edge of the sample *Immersion 0h/week* could be related to the decrease of the solubility of aluminum highlighted in the previous section for one week. Hence, aluminum could form an oxide layer when the immersion time is increased.

As a reminder, only a qualitative analysis has been done since the deposit layers are very thin. Hence, other more sensitive techniques should be considered in order to have a quantitative analysis and to be able to identify the oxides present on the surface.

Furthermore, non-negligible amounts of phosphorus and calcium could be noticed on the cracking deposit layers. The presence of those components could be explained by a higher affinity of the phosphorus and calcium to combine and precipitate on the metal surface. In addition, by comparing the results for all samples, no true differences between the concentrations can be highlighted. As a matter of fact, the corrosion rates of the immersed samples for 1 and 7 days are very close, only the corrosion rate for an immersion of 1 hour is much larger. Moreover, in the work of Liu et al.[47], they found as well that CaP compounds were more easily formed on the areas of the metal already corroded.

Finally, it can be concluded that the main areas affected by an immersion are the edges, the hole and the region below the hole of the sample which could be due to the difference of volume of solution encompassing those areas. In addition, from the tests performed during 1 hour, it can be highlighted that the first regions to be affected are the edges of the samples due to a larger amount of solution that encompassed the edges. Furthermore, the main components of the cracking deposited layers are oxygen, iron as well as carbon which may lead to the formation of oxide. Moreover, non negligible amounts of phosphorus and calcium can be noticed on the corroded areas of the metal.

Conclusion and perspectives

Through this study, a TRIP-maraging steel that could lead to biodegradable biomedical applications as the coronary stent has been characterised. More precisely, the alloy Fe-9Mn-3Ni-1,4Al-0,01C (mass%) produced by casting has been analysed. The research was focused on the effect of heat treatments composed either of a homogenisation and a further annealing or of thermal cycles on the properties of the alloy. Specifically, the microstructure, the mechanical and corrosion properties have been investigated.

Following the investigations of the influence of the heat treatments on the alloy, the microstructure, the phase fraction of austenite and a comparison with numerical simulations have been performed. It has been highlighted that increasing the time of annealing increases the phase fraction of austenite. However, a saturation after an annealing of 24 hours can be noticed. In addition, the thermal cycling followed by an annealing accelerates the reversion and leads to a phase fraction of austenite of the same order of magnitude as a homogenization followed by the same annealing treatment. Moreover, increasing the time of homogenisation increases the speed of reversion whereas decreasing the temperature of the homogenisation slows down the reversion.

On the other hand, by comparing the experimental and numerical results the same observations have been drawn: a longer annealing leads to a higher austenite fraction. In addition, the austenite phase presents higher content in manganese, nickel and carbon than the martensite phase.

Furthermore, the thermal expansion coefficients of the ferrite are lower than the ones of the austenite phase. Moreover, after the annealing, the thermal expansion coefficients of the austenite phase are slightly decreased due to the presence of martensite. On the other hand, the thermal cycling decreases the M_S and M_f temperatures.

The microstructure presents martensite and austenite grains that grow along the martensite laths and the prior austenite grains. In addition, it appears that the austenite grains grow when the time of annealing increases. Contrary to most of the samples, the microstructure resulting from a thermal cycling is finer but presents as well martensite and austenite.

The mechanical properties were then further analysed. It has been noted that the fully martensitic sample was very brittle and hard at the same time. On the opposite, the samples that were further annealed were related to ductile materials. In addition, increasing the time of annealing increases the mechanical properties. However, a saturation can be noticed after an annealing of 24 hours.

Thereafter, the corrosion properties were investigated. It has been highlighted that the corrosion rates are very high at the beginning of the immersion. Moreover, increasing the time of annealing globally increases the corrosion rates. However, from an annealing time of 24 hours the corrosion rates appear lower.

The microstructure of the immersion tests presents affected regions near the edges, the hole and below the hole. The regions affected present cracking deposited layers, corrosion products and pits. In addition, it appears that the first regions to be affected during the immersion are the edges of the sample. Moreover, the different layers present large amount of oxygen, iron and carbon. Furthermore, there are non-negligible amounts of calcium and phosphorus on the corroded areas of the surface.

This study revealed interesting properties and trends from the heat treatments performed. However, further investigations should be performed to fully characterise this TRIP-maraging steel.

First, in order to have a better understanding of the mechanical properties and a better idea of the holding time of the annealing at which the equilibrium austenite volume fraction is achieved, the same experiments as well as new ones should be carried out in order to be able to determine a general trend. Specifically, one should perform the same heat treatments as well as intermediate heat treatments and thermal cycles. Doing so, a better understanding of the evolution of the austenite phase fraction and the mechanism of the saturation as well as its approximate value could be emphasised. Moreover, a XRD should be performed on the sample which has been electropolished in order to be able to study the impact of the polishing on the austenite volume phase fraction.

Second, to fully characterise and highlight general trends of the corrosion properties, new immersion tests should be performed. Specifically, the same immersion tests as well as new tests with new heat treatments should be done. In addition, samples with different annealing holding times should be implemented for immersion tests with varying immersion time to fully understand the impact of the presence of austenite. Moreover, it could be of interest to study the corrosion process of samples that had sustained thermal cycles and highlight the influence of the microstructure.

Third, since only a qualitative analysis has been performed with an EDX analysis due to the very thin layer of the deposited products, further analysis should be considered. For instance, a X-ray photoelectron spectroscopy as well as a Raman spectroscopy could be performed in order to be able to carry out a quantitative analysis and highlight the specific oxides present on the surface.

Finally, there is still a long way before this TRIP-maraging steel becomes a material for the manufacture of coronary stents. Hence, a better understanding of its properties regarding heat treatments performed as well as its degradability properties should be further investigated.

Bibliography

[1] National Heart Lung and Blood Institute. *Stents.* `https://www.nhlbi.nih.gov/health-topics/stents`, consulted on 3/04/18.

[2] Harvard Health publishing Harvard Medical School. *Bypass or angioplasty with stenting: How do you choose?* `https://www.health.harvard.edu/heart-health/bypass-or-angioplasty-with-stenting-how-do-you-choose`, consulted on 3/04/18.

[3] K.Zamanian PHD and J. Stillborn Idata Research INC. *New Directions for Stent Technology.* `https://www.dicardiology.com/article/new-directions-stent-technology`, consulted on 3/04/18.

[4] Scot Garg MB CHB Patrick W. Serruys MD PHD. "Coronary stent : looking forward". In: *Journal of the American College of Cardiology* 56.10 (2010). DOI: `10.1016/j.jacc.2010.06.008`.

[5] Yoshihiro Tomita and Takeshi Iwamoto. "Constitutive modeling of TRIP steel and its application to the improvement of mechanical properties". In: *International Journal of Mechanical Sciences* 37.Issues 12 (1995).

[6] Tim Taylor. *Cardiovascular System.* `http://www.innerbody.com/image/cardov.html`, consulted on 4/04/18.

[7] Paul Gillam. *2.65 Blood vessels – A* understanding for iGCSE Biology.* `https://pmgbiology.com/2015/02/15/blood-vessels-a-understanding-for-igcse-biology/`, consulted on 6/04/2018.

[8] The free dictionary by Farlex. *capillary bed.* `https://medical-dictionary.thefreedictionary.com/capillary`, consulted on 16/05/18.

[9] Unknown. *Capillary.* `https://en.wikipedia.org/wiki/Capillary`, consulted on 16/05/18.

[10] National Heart Lung and Blood Institute. *Coronary Heart Disease.* `https://www.nhlbi.nih.gov/health-topics/coronary-heart-disease`, consulted on 4/04/2018.

[11] National Heart Lung and Blood Institute. *Coronary Artery Bypass Grafting.* `https://www.nhlbi.nih.gov/health-topics/coronary-artery-bypass-grafting`, consulted on 4/04/2018.

[12] Summit Medical Group. *Coronary artery stent.* `https://www.summitmedicalgroup.com/library/adult_health/car_coronary_artery_stents/`, consulted on 20/04/2018.

[13] T.W. Duerig and M. Wholey. "A comparison of balloon- and self-expanding stents". In: *Minimally Invasive Therapy et Allied Technologies* 11.4 (2002).

[14] N. Danchin I. Durand V. Decalf A. Lafont and D. Blanchard. "Coronary stents: a lovely story". In: *Analyse de cardiologie et d'angéiologie* 56.2 (2007).

[15] M.D.. A. H1JCHWAL.D. M.D.. c. UNTERBERG. M.D.. G. WERNER. M.D.. E. VOTH. M.D.*. H. KREUZER and v. WIEGAND. M.D. "Initial Clinical Results with the Wiktor Stent: A New Balloon-Expandable Coronary Stent". In: *Clinical Cardiology* 14.5 (1991).

[16] PETER B. and BERGER M.D. “The Cook Inc. Gianturco-Roubin Flex-Stent”. In: *Journal of interventional Cardiology* 9.2 (1996).

[17] Javaid Iqbal Julian Gunn and Patrick W. Serruys. “Coronary stents: historical development, current status and future directions”. In: *British Medical bulletin* 106.1 (2013).

[18] A. Ong J. Aoki M. Kutryk and P Serruys. “How to accelerate the endothelialization of stents”. In: *Archives des maladies du coeur et des vaisseaux* 98.2 (2005).

[19] William M Wilson and Nicholas LM cruden. “Advances in coronary stent technology: current expectations and new developments”. In: *Research reports in clinical cardiology* 4 (2013).

[20] H. Hermawan D. Dubé and D. Mantovani. “Developments in metallic biodegradable stents”. In: *Acta Biomaterialia* 6.5 (2010).

[21] Richard A. Schatz MD. “A View of Vascular Stents”. In: *Circulation* 79.2 (1989).

[22] J Butany K Carmichael S W Leong and M J Collins. “Coronary artery stents: identification and evaluation”. In: *Journal of clinical pathology* 58.8 (2004).

[23] C. Mauli Agrawal Gopinath Mani Marc D. Feldman Devang Patel. “Coronary stents: A materials perspective”. In: *Biomaterials* 28.9 (2007).

[24] Unknown. *Intimal hyperplasia.* `https://en.wikipedia.org/wiki/Intimal_hyperplasia`, consulted on 20/04/2018.

[25] Unknown. *Tunica intima.* `https://en.wikipedia.org/wiki/Tunica_intima`, consluted 20/04/2018.

[26] Dussaillant GR Mintz GS Pichard AD Kent KM Satler LF Popma JJ Wong SC and Leon MB. “Small stent size and intimal hyperplasia contribute to restenosis: a volumetric intravascular ultrasound analysis”. In: *Journal of the American College of Cardiology* 26.3 (1995).

[27] Olivier F. Bertrand MD Rajender Sipehia PHD Rosaire Mongrain Josep Rodé MD and all. “Biocompatibility Aspects of New Stent Technology”. In: *Journal of the American College of Cardiology* 32.3 (1998).

[28] unknown. *Chapter 6. Mechanical Properties of Metals.* `http://www.virginia.edu/bohr/mse209/chapter6.htm`, consulted on 17/05/2018.

[29] N.Figueira T.M.Silva M.J.Carmezim and J.C.S.Fernandes. “Corrosion behaviour of NiTi alloy”. In: *Electrochimica Acta* 54.Issue 3 (2009).

[30] Maryam Moravej and Diego Mantovani. “Biodegradable Metals for Cardiovascular Stent Application:Interests and New Opportunities”. In: *International Journal of 0Molecular Sciences* 12.7 (2011).

[31] Hui Ying Ang Ying Ying Huang Soo Teik Lim Philip Wong Michael Joner and Nicolas Foin. “Mechanical behavior of polymer-based vs. metallic-based bioresorbable stents”. In: *Journal of Thoracic disease* 9.supp 9 (2017).

[32] Futura santé. *Pyruvate.* `http://automotive.arcelormittal.com/saturnus/sheets/B_EN.pdf`, consulted on 17/05/2018.

[33] Wikipedia. *Citric acid cycle.* `https://en.wikipedia.org/wiki/Citric_acid_cycle`, consulted on 17/05/2018.

[34] Rottenstein law group. *What does FDA approval means ?* `http://www.rotlaw.com/legal-library/what-does-fda-approval-mean/`, consulted on 17/05/2018.

[35] Ormiston JA Webber B Ubod B Darremont O and Webster MW. “An independent bench comparison of two bioresorbable drug-eluting coronary scaffolds (Absorb and DESolve) with a durable metallic drug-eluting stent (ML8/Xpedition)”. In: *EuroIntervention : Journal of EuroPCR* 11.1 (2015).

[36] Heublein B Rohde R Niemeyer M Kaese V Hartung W and Rocken C. “Degradation of metallic alloys-A new principle in stent technology?” In: *J. Am. Coll. Cardiol* 35 (2000).

[37] Heublein B Rohde R Kaese V Niemeyer M Hartung W and Haverich A. “Biocorrosion of magnesium alloys: a new principle in cardiovascular implant technology?” In: *Heart (British Cardiac Society)* 89.6 (2003).

[38] Di Mario C Griffiths H Goktekin O Peeters N Verbist J Bosiers M Deloose K Heublein B Rohde R Kasese V Ilsley C and Erbel R. “Drug-eluting bioabsorbable magnesium stent”. In: *Journal of interventional cardiology* 17.6 (2004).

[39] Zartner P Cesnjevar R Singer H and Weyand M. “First successful implantation of a biodegradable metal stent into the left pulmonary artery of a preterm baby”. In: *Catheterization and cardiovascular interventions : official journal of the Society for Cardiac Angiography et Interventions* 66.4 (2005).

[40] Waksman R Pakala R Kuchulakanti PK Baffour R Hellinga D Seabron R Tio FO Wittchow E Hartwig S Harder C Rohde R Heublein B Andreae A Waldmann KH and Haverich A. “Safety and efficacy of bioabsorbable magnesium alloy stents in porcine coronary arteries”. In: *Catheterization and cardiovascular interventions : official journal of the Society for Cardiac Angiography et Interventions* 68.4 (2006).

[41] Ghanashyam Acharya b and Kinam Park. “Mechanisms of controlled drug release from drug-eluting stentsB”. In: *Advanced Drug Delivery Reviews* 58.3 (2006).

[42] Lu P Fan H Liu Y Cao L Wu X and Xu X. “Controllable biodegradability, drug release behavior and hemocompatibility of PTX-eluting magnesium stents”. In: *Colloids and Surfaces B: Biointerfaces* 83.1 (2011).

[43] Hermawan H Alamdari H Mantovani D and Dube D. “Iron-manganese: new class of metallic degradable biomaterials prepared by powder metallurgy”. In: *Adv. Mater. Res* 15 (2007).

[44] Hermawan H Dube D and Mantovani D. “Development of degradable Fe-35Mn alloy for biomedical application.” In: *Powder Metall.* 51 (2008).

[45] Hermawan H Dube D and Mantovani D. “Degradable metallic biomaterials: design and development of Fe-Mn alloys for stents”. In: *Journal of biomedicals materials research* 93.1 (2010).

[46] Schinhammer M Hanzi AC Loffler JF and Uggowitzer PJ. “Design strategy for biodegradable Fe-based alloys for medical applications”. In: *Acta Materialia* 6.5 (2010).

[47] Liu B and Zheng Y. “Effects of alloying elements (Mn, Co, Al, W, Sn, B, C and S) on biodegradability and in vitro biocompatibility of pure iron”. In: *Acta Biomaterialia* 7.3 (2011).

[48] Liu B Zheng Y and Ruan L. “In vitro investigation of Fe30Mn6Si shape memory alloy as potential biodegradable metallic material”. In: *Materials letters* 65.3 (2011).

[49] Nie F Zheng Y Wei S Hu C and Yang G. “In vitro corrosion, cytotoxicity and hemocompatibility of bulk nanocrystalline pure iron”. In: *Biomedical Materials* 5.6 (2010).

[50] Wikipedia. *Severe plastic deformation.* `https://en.wikipedia.org/wiki/Severe_plastic_deformation`, consulted on 17/05/2018.

[51] Katharina Maria Angelika Hausmann. "TRIP-assisted Thin Sheet Steel with a Bainitic and/or Martensitic Matrix - Effects of Alloying Elements and Heat Treatment on Phase Transformations, Microstructures, and Mechanical Properties". PhD thesis. TECHNISCHE UNIVERSITÄT MÜNCHEN, 2014.

[52] Sourabh Chatterjee. "Transformations in TRIP-assisted Steels: Microstructure and Properties". PhD thesis. Darwin College, University of Cambridge, 2006.

[53] D. Raabe D. Ponge O. Dmitrieva and B. Sander. "Nanoprecipitate-hardened 1.5 GPa steels with unexpected high ductility". In: *Scripta materialia* 60.12 (2009).

[54] T Hickel B Grabowski F Kormann and J Neugebauer. "Advancing density functional theory to finite temperatures: methods and applications in steel design". In: *Journal of Physics: condensed matter* 24.5 (2012).

[55] Dierk Raabe. *Transformation Induced Plasticity Steels - TRIP steels.* `http://www.dierk-raabe.com/trip-steels/`, consulted in 18/04/2018.

[56] Arcelor Mittal. *TRIP (TRansformation Induced Plasticity) steels.* `http://automotive.arcelormittal.com/saturnus/sheets/B_EN.pdf`, consulted on 25/04/2018.

[57] B.C. De Cooman. "Structure–properties relationship in TRIP steels containing carbide-free bainite". In: *Current Opinion in Solid State and Materials Science* 8.3 (2004).

[58] Shaofan Li and Gang Wang. *Introduction to Micromechanics and Nanomechanics.* World Scientific, 2008.

[59] K Tanaka Q-P Sun and F.D Fischer. "Transformation-induced plasticity (TRIP)". In: *Applied Mechanics Reviews* 49.6 (1996).

[60] Elena V. Pereloma Azdiar A. Gazder and Ilana B. Timokhina. *Encyclopedia of Iron, Steel and their Alloys.* CRC Press, 2016. Chap. 9 Retained austenite: transformation-induced plasticity.

[61] Prof. Wenjea J. Tseng. *Chapter 8: Slip.* `http://audi.nchu.edu.tw/~wenjea/mechanical103/Chapter_8.pdf`, consulted on 18/05/2018.

[62] J. Chiang B. Lawrence J.D. Boyd and A.K. Pilkey. "Effect of microstructure on retained austenite stability and work hardening of TRIP steels". In: *Material science and engineering A* 528.13 (2011).

[63] F. Sun Y.F. Gu J.B. Yan Y.X. Xu Z.H. Zhong and M. Yuyama. "Creep deformation and rupture mechanism of an advanced wrought NieFe-based superalloy for 700 $°C$ class A-USC steam turbine rotor application". In: *Journal of alloys and compounds* 687 (2016).

[64] Unknown. *Orowan mechanism.* `https://www.giessereilexikon.com/en/foundry-lexicon/Encyclopedia/show/orowan-mechanism-3506/`, consulted on 26/04/2018.

[65] Dierk Raabe Dirk Ponge Olga Dmitrieva and Benedikt Sander. "Designing Ultrahigh Strength Steels with Good Ductility by Combining Transformation Induced Plasticity and Martensite Aging". In: *ADVANCED ENGINEERING MATERIALS* 11.7 (2009).

[66] Wei Sha and Zhanli Guo. *Maraging Steels Modelling of Microstructure, Properties and Applications.* Woodhead Publishing Series, 2009. Chap. 1- Introduction to maraging steels.

[67] M-M. Wang C.C. Tasan D. Ponge A. Kostka and D. Raabe. "Smaller is less stable: Size effects on twinning vs. transformation of reverted austenite in TRIP-maraging steels". In: *Acta Materialia* 79.10 (2014).

[68] Feng Qian Joanne Sharp and W. Mark Rainforth. "Microstructural evolution of Mn-based maraging steels and their influences on mechanical properties". In: *Material sciences engineering A* 674.09 (2016).

[69] M.-M. Wang C.C. Tasan D. Ponge A.-Ch. Dippel and D. Raabe. “Nanolaminate transformation-induced plasticity–twinning-induced plasticity steel with dynamic strain partitioning and enhanced damage resistance”. In: *Acta Materialia* 85.02 (2015).

[70] Dierk Raabe. *TWIP steels (Twinning Induced Plasticity Steels)*. `http://www.dierk-raabe.com/twip-steels/`, consulted on 18/04/2018.

[71] R Winston Revie and Herbert H Uhlig. *Corrosion and corrosion control: An introduction to corrosion science and engineering*. Wiley interscience, 2008.

[72] Einar Bardal. *Corrosion and Protection*. Springer-Verlag London, 2004.

[73] B. Liu and Y.F. Zheng. “Effects of alloying elements (Mn, Co, Al, W, Sn, B, C and S) on biodegradability and in vitro biocompatibility of pure iron”. In: *Acta Biomaterialia* 7.3 (2010).

[74] Bill Nimmo and Gareth Hinds. *Beginners guide to corrosion*. `http://www.npl.co.uk/upload/pdf/beginners_guide_to_corrosion.pdf`, consulted on 27/04/2018. 2003.

[75] Intrafit. *About human blood pH*. `http://www.infrafit.ro/en/services-articles/human-blood-ph/`, consulted on 19/05/2018.

[76] Noam Eliaz. *Degradation of Implant Materials*. Springer, New York, NY, 2012.

[77] Parimal Ramesh Udgave. *Speciation analysis of silver ions using inductively coupled plasma optical emission spectrometry (ICP - OES)*. `https://www.biotecharticles.com/Biotechnology-products-Article/Speciation-Analysis-of-Silver-Ions-using-ICP-OES-4233.html`, consulted on 19/05/2018. 2017.

[78] Foundation of Computational Thermodynamics. *DICTRA Examples Guide Version 2015b*. 2015.

[79] Linseis thermal analysis. *Dilatometry / Dilatometer (DIL) - Expansion Measurements*. `https://www.linseis.com/en/our-products/dilatometer/`, consulted on 27/04/18.

[80] Segun Afokhainu Agbadua Chinedum Ogonna Mgbemena Chika Edith Mgbemena and Lazarus Onyebuchi Chima. “Thermal Cycling Effects on the Fatigue Behaviour of Low Carbon Steel”. In: *Journal of Minerals and Materials Characterization and Engineering* 10.14 (2011).

[81] François-Joseph Contat. *DETERMINATION DU DIAGRAMME TRC POUR UN ACIER HAUTE RESISTANCE, LE S690QH*. `https://infoscience.epfl.ch/record/231924/files/PDM_contat_2014_corr.pdf`, consulted on 27/04/18. 2014.

[82] Sarah Reuter. *Biocorrosion of iron based alloys for bioresorbable coronary stent applications*. 2016.

[83] University of Wyoming Susan Swapp. *Scanning Electron Microscopy (SEM)*. `https://serc.carleton.edu/research_education/geochemsheets/techniques/SEM.html`, consulted on 29/04/18.

[84] Ameer A. Hilal. *High Performance Concrete Technology and Applications*. Ed. by Salih Yilmaz. 2016. Chap. Microstructure of Concrete.

[85] Intertek group. *Energy Dispersive X-Ray Analysis (EDX) - Energy dispersive X-Ray (EDX) composition analysis*. `http://www.intertek.com/analysis/microscopy/edx/`, consulted on 30/04/2018.

[86] Dr. Thayumanasamy Somasundaram. *Data Collection Step Size Selection How to decide step size, time per step and collection time on panalytical X-PERT pro powder*. `http://biophysics.fsu.edu/soma/wp-content/uploads/sites/13/2016/12/2016PANalyticalXPertProStepSize.pdf`, consulted on 20/05/18. 2016.

[87] EAG Laboratories. *Diffraction des rayons X, analyse XRD.* `http://www.eaglabs.fr/cm/xrd.html`, consulted on 30/04/2018.

[88] B. D. Cullity. *Elements of X-Ray diffraction Second edition.* Addison - Wesley publishing company Inc., 1978.

[89] Antoine Hilhorst. *Interactions between diffusible hydrogen and the microstructure of a FeCMnSi third generation steel exhibiting a TRIP effect.* 2017.

[90] Ashish Garg. *A Brief Introduction to Rietveld Analysis of XRD Patterns.* `https://www.iitk.ac.in/tkic/workshop/XRD/ppt/Prof\%20Garg/AshishGarg_Rietveld.pdf`, consulted on 30/04/2018.

[91] A. Albinati and B.T. M. Willis. *International Tables for Crystallography Vol. C.* 2006. Chap. 8.6 The Rietveld method. DOI: `10.1107/97809553602060000614`.

[92] Lei Guoa Hans Roelofs Mirkka Ingrid Lembke and Harshad Kumar Dharamshi Hansraj Bhadeshia. "Modelling of recalescence effect on austenite decomposition". In: *Materials Science and Technology* 33.10 (2017).

[93] Paulo Maria de O. Silva Hamilton Ferreira G. de Abreu Victor Hugo C. de Albuquerque Pedro de Lima Neto João Manuel R.S. Tavares. *Cold deformation effect on the microstructures and mechanical properties of AISI 301LN and 316L stainless steels.* `https://web.fe.up.pt/~tavares/downloads/publications/artigos/Paper_M&D_32_2_605-614.pdf`, consulted on 8/06/2018.

[94] Diana Pérez Escobar, Sara Silva Ferreira de Dafe, and Dagoberto Brandao Santos. "Martensite reversion and texture formation in 17Mn-0.06C TRIP/TWIP steel after hot cold rolling and annealing". In: *Journal of material research and technology* 4.2 (2014).

[95] Seawoong Lee and Bruno C. De Cooman. "On the Selection of the Optimal Intercritical Annealing Temperature for Medium Mn TRIP Steel". In: *Metallurgical and Materials Transactions A* 44.11 (2013).

[96] M.K. Banerjee. *Comprehensive Materials Finishing.* Vol. 2. Elsevier, 2017. Chap. 2.8 Heat Treatment of Commercial Steels for Engineering Applications - Pages 180–213.

[97] T. ISHIKAWA. *Microstructure Evolution in Metal Forming Processes.* Woodhead publishing series in Metals and Surface engineering, 2014. Chap. Part I : 1- Understanding and controlling microstructural evolution in metal forming: an overview.

[98] S.S. Sahay C.P. Malhotra and A.M. Kolkhede. "Accelerated grain growth behavior during cyclic annealing". In: *Acta Materialia* 51.2 (2003).

[99] Mehran Maalekian. "The Effects of Alloying Elements on Steels". PhD thesis. Technische Universität Graz, 2007.

[100] Seok-Jae Lee Yong-Min Park and Young-Kook Lee. "Reverse transformation mechanism of martensite to austenite in a metastable austenitic alloy". In: *Materials Science and Engineering A* 515.Issues 1-2 (2012).

[101] Matilda Tehler. "Modeling Phase Transformations and Volume Changes during Cooling of Case Hardening Steels". PhD thesis. KTH Industrial engineering and management, 2009.

[102] Wikipedia. *Martensite.* `https://en.wikipedia.org/wiki/Martensite`, consulted on 8/06/2018.

[103] Javier Hidalgo and Maria Jesus Santofimia. "Effect of Prior Austenite Grain Size Refinement by Thermal Cycling on the Microstructural Features of As-Quenched Lath Martensite". In: *Metallurgical and Materials Transactions A* 47.11 (2016).

[104] M. Spittel and T. Spittel. *Metal Forming Data of Ferrous Alloys - deformation behaviour.* Springer, Berlin, Heidelberg, 2009. Chap. 4.5 Thermal expansion of steel.

[105] Subodh Kumar Sudeep Ingole Hajo Dieringa and Karl-Ulrich Kainer. "Analysis of thermal cycling curves of short fibre reinforced Mg-MMCs". In: *Composites Science and Technology* 63.Issues 12 (2003).

[106] Chang Hee Suh Yun-Chul Jung and Young Suk Kim. "Effects of thickness and surface roughness on mechanical properties of aluminum sheets". In: *Journal of Mechanical Science and Technology* 24.10 (2010).

[107] Erlin Zhang Haiyan Chen and Feng Shen. "Biocorrosion properties and blood and cell compatibility of pure iron as a biodegradable biomaterial". In: *Journal of material science - Materials in medicine* 21.7 (2016).

[108] Unknown. *Passivation.* `https://fr.wikipedia.org/wiki/Passivation`, consulted on 8/06/2018.

[109] W. Handoko F. Pahlevani and V. Sahajwalla. "Effect of Retained Austenite Stability in Corrosion Mechanism of Dual Phase High Carbon Steel". In: *International Journal of Materials and Metallurgical Engineering* 12.1 (2018).

[110] Animesh Talapatra Jayti Datta and N.R. Bandyopadhyay. "Mechanics of Corrosion of TRIP-assisted Steels in different NaCl solutions". In: *Oriental Journal of Chemistry* 28.3 (2009).

[111] Technical tutorial Misumi. *Surface finishing tutorials - Passivation of Metals.* `http://www.misumi-techcentral.com/tt/en/surface/2010/08/052-passivation-of-metals.html`, consulted on 8/06/2018.

[112] European federation of associations of insulation contractors (FESI). *Principles of Metal Corrosion - FESI document 9.* `https://fesi.eu/images/FESIdocs/ThermalTechnical/TTC9_Metal_Corrosion.pdf`, consulted on 8/06/2018. 2007.

Rue Archimède, 1 bte L6.11.01, 1348 Louvain-la-Neuve **www.uclouvain.be/epl**